NEW ECR-PECVD REACTOR AND PRELIMINARY THIN FILM DEPOSITIONS

Installation of a New Electron Cyclotron Plasma Enhanced Chemical Vapour Deposition (ECR-PECVD) Reactor and a Preliminary Study ofThin Film Depositions

By

RYSZARD DĄBKOWSKI, B. ENG

A Thesis Submitted to the School of Graduate Studies in Partial Fulfilment of the

Requirements of the Degree Master of Applied Science

McMaster University

McMaster University MASTER OF APPLIED SCIENCE (2012)
Hamilton, Ontario (Engineering Physics)

TITLE: Installation of a New Electron Cyclotron Plasma Enhanced Chemical Vapour Deposition (ECR-PECVD) Reactor and a Preliminary Study of Thin Film Depositions

Author: Ryszard Dąbkowski

Supervisor: Professor Peter Mascher

Number of pages: xvi, 172

Abstract:

A new electron cyclotron plasma enhanced chemical vapour deposition (ECR-PECVD) reactor has been installed and tested at McMaster University. The focus of this project was the installation of the reactor and the growth of silicon oxide, silicon oxynitride, cerium doped silicon oxynitride and aluminium doped silicon oxide films to test the capabilities of the reactor.

Silicon oxide films were prepared with near-stoichiometric compositions and silicon rich compositions. Good repeatability of the growths was seen. An increase in deposition temperature showed stable refractive index and a decrease in the growth rates.

Silicon oxynitride films of varying compositions were prepared, and showed a non-uniformity of ~1% and growth rates of ~3.5 nm/min. Films prepared with a low oxygen flow were seen to be nitrogen rich.

Although the depositions using $Ce(TMHD)_4$ showed significant cerium incorporation, there was also high carbon contamination. One likely cause of this is the high sublimator temperature used during depositions or a thermal shock to the precursor during initial system calibration. A definitive cause of the carbon contamination has not been established.

The cerium films showed strong blue luminescence after post-deposition annealing in N_2 above 900° C. A drop in the luminescence was observed at 1100° C and a return of the luminescence at 1200° C. Generally, high cerium incorporation was associated with higher total luminescence.

$Al(THMD)_3$ was evaluated as an aluminium precursor for Al-doped silicon oxide films. The films showed aluminium content up to 6% demonstrating the viability of using $Al(THMD)_3$ as a Al doping precursor.

Acknowledgments:

Acknowledgements:

I would like to thank the following individuals for valuable contributions to this work:

Dr. Peter Mascher, my supervisor, for his solid guidance, support and encouragement throughout my time as a masters candidate at McMaster. Without his teaching, discussions and encouragement this work could never have happened. I would further like to thank him for the opportunity to tackle such an ambitious project. His confidence in my abilities throughout the entire process, especially when my own confidence would waiver, has meant a great deal to me.

Dr. Jacek Wojcik, who has spent countless hours helping me directly, through tutoring and discussion. His technical excellence has given me an example to strive towards and his strong leadership has encouraged me to develop my own skills with the knowledge that his support was always available. Without the countless hours Jacek has dedicated to this project, and to me, none of this would have been possible.

Bram Evert whose dedication over two summers with our group has been of great assistance. His friendship and outstanding attitude have made him a pleasure to work with during long days of deposition. I wish Bram all the best in his future studies.

Sarah Langstaff who has been an invaluable help during the early stages of this project.

Evgueni Chelomentsev for his technical support and assistance in the laboratory.

Patrick Wilson for the many enlightening discussions and late night deep dish pizzas.

The RBS analysis would not have been possible without the help of Jack Hendriks and Dr. William Lennard (University of Western Ontario).

I would like to extend a special thanks to Dr. Andy Knights, who has always been a pleasure to be around and has encouraged me to greater things since the first time I walked into his class, fifteen minutes late, lost and half asleep seven years ago.

I would like to thank my parents Hanna Dąbkowska, Antoni Dąbkowski, and my sister Aleksandra Dąbkowska. They have been inspirations to me and without their support and never ending family dinner discussions on materials science I could not be here now.

Finally I would like to thank my partner Robin. Her ability to deal with my choleric fits and phlegmatic moods is simply amazing. Without her push, this work could not have been completed.

Table of Contents

List of Figures

Index of Tables

Chapter 1: Introduction

Section 1.1: Motivation

One of the largest forces of change in the technological, economic and social history of the past few decades has been the development of silicon processing technologies and the associated microelectronics revolution. This technological progress has moved at an unprecedented speed first characterized by Moore's law [1], which initially claimed that the complexity of a circuit normalized to cost increases by a factor of two every year.

Although updated frequently, the technical progress has generally followed Moore's law for decades, aided mainly by the shrinking of both the individual devices and the interconnects used in integrated circuit manufacture. The progress is, however, now reaching fundamental limits imposed by the inability to further reduce the RC time delay of the interconnects and limits on reliability of transistors with ever smaller gate thicknesses and channel dimensions.

One proposed solution to extend the period of rapid technological progress is a fundamental change from using electrons as the medium of information to the use of photons in optical computing. While the end goal would be the use of photons in all of the information processing, the first step should be focused on the current limiting factor: long interconnects. By using optical interconnects, with a light emitter and detector on each end, the RC time delay obstacle could be avoided.

While the technologies for waveguides, to replace the actual interconnects; detectors, to link the optical signals with the rest of the electrical circuits and even modulators to handle some of information processing are fairly well developed, a practical integratable silicon-based light source has yet to be achieved. It is the final hurdle left to achieving photonic computing which could leverage the low material cost, scale and development of existing silicon processing technologies and infrastructure lacking for devices based on other material groups.

Another area of intense interest is high efficiency lighting. As the appetite for energy increases worldwide, lighting (which accounts for approximately 8.8% of residential energy consumption and is the single largest end-use of electricity in commercial buildings [2]) is being targeted as an area in which efficiency needs improvement. There is a significant push away from inefficient, short-lived incandescent technologies and into solid state lighting.

Although commercially mature solid state lighting for niche markets exists today, it is largely based on III-V materials, many of them prohibitively expensive for most common applications. Organic based approaches currently suffer from lifetime and packaging issues. The relatively low materials and processing costs combined with the large established infrastructure for silicon processing would give silicon-based solid state lighting a competitive advantage over III-V based light sources [3] and could allow for the wide scale acceptance of solid state lighting products. Furthermore, the relatively low cost of silicon substrates means that planar technologies, in which the luminescence is distributed over a wide surface area could create more convenient light. The development of this technology with satisfactory efficiency would require large area, well controlled, defect and impurity free deposition technologies.

Since bulk silicon has an indirect electronic bandgap, radiative carrier recombination requires the participation of a phonon, resulting in recombination rates orders of magnitude lower than those of direct bandgap materials such as GaAs [4]. The promising applications of light emitting silicon have drawn particular interest to two specific materials groups: nanostructured silicon, in which quantum confinement effects allow for the emission of light and rare-earth doped silicon which utilizes emissions from rare-earth ions in a silicon based matrix. Interest in porous silicon was sparked by the discovery of efficient photoluminescence from porous silicon [5], however, the incompatibility with mainstream silicon processing methods limits the commercial applicability of this approach. The technique involving the production of silicon nanocrystals and nanoclusters by the growth of silicon rich films with subsequent high temperature annealing to promote phase separation of Si from the host matrix is compatible with standard high vacuum silicon processing procedures and promises the potential for well controlled material characteristics, promoting interest in the field [6].

The study of rare earth doped silicon has largely focused on Er^{3+} due to the 1.54

μm emission compatible with the telecommunications window [7]. Solid state lighting applications require a wider range of emissions to provide usable white light. Although creating “white” light appropriate for general illumination applications would require the mixing of red, green and blue emissions, respectively, from Eu, Tb and Ce [8]. Effective luminescence from silicon thin films can be achieved by using the energy transfer from silicon nanoclusters to rare earth dopants and rare-earth silicates formed during annealing of the film structures [6,7].

The choice of research tools aimed at developing silicon photonic technologies is far from trivial. The variation of material properties with deposition method means that a commercially viable method should be used if possible so that research results are to be easily scaled up to the manufacturing scale. At the same time, the tools require reasonable versatility so that the investment of precious research funds into expensive hardware allows a wide range of materials and structures to be studied. While in this branch of photonic research this means the ability to deposit a broad range of silicon oxynitrides the ability to grow other materials (such as silicon carbide based materials) is a great benefit. Finally, a system which is easily adaptable for a variety of dopants will ensure that the tools will be usable for research as new candidate dopants arise.

Section 1.2: Thesis Contents

Chapter 2 begins by giving some background on chemical vapour deposition (CVD) and important processes in CVD of thin films are reviewed. Basic physics related to the generation of a plasma in electron cyclotron resonance plasma enhanced chemical vapour deposition (ECR-PECVD) is discussed. A review of various deposition methods is given and the justification of the use of an ECR-PECVD reactor for silicon photonics research is provided.

The next chapter is a brief review of the general materials studied in this work. The focus is on various compositions of SiO_xN_y films and metalorganic precursors used in the study.

In chapter 4 an overview of the characterization techniques used in the study is presented. Single wavelength, single angle ellipsometry (SWE) as well as variable angle spectroscopic ellipsometry (VASE) are introduced and applications and limitations of the techniques are discussed. Photoluminescence spectroscopy is reviewed and finally, the basic theory of Rutherford backscattering spectrometry (RBS) is presented and a discussion of the models used in determining the composition of films is given.

A technical review of the installed ECR-PECVD reactor, including some details of the setup procedure, is presented in chapter 5.

Chapter 6 presents the result of selected preliminary growths from the system. The discussion focuses on several sample groups. SiO_x films grown under varying growth parameters in low vacuum conditions are presented and an analysis of a variety of compositions of SiO_x grown under high vacuum are discussed. The results of undoped SiO_xN_y growths are investigated and an analysis of ellipsometric, RBS and PL studies of

Ce-doped oxynitride films is given. Finally the growth of Al doped films is presented and discussed.

The work is concluded with a discussion of future research directions both in regards to gaining a better understanding of the system behaviour and future studies on materials deposited with the system.

Chapter 2: Chemical Vapour Deposition Background

Section 2.1: Introduction

This chapter is intended to give some background information about chemical vapour deposition (CVD) and introduce some of the important concepts related to plasma enhanced chemical vapour deposition (PECVD), in particular electron cyclotron resonance (ECR) as a method of plasma generation for the growth of thin films.

A short review of various thin film deposition methods is given and the advantages of using CVD and in particular, PECVD for the growth of uniform, conformal silicon based materials are discussed. The design requirements for a system to deposit silicon oxynitride films doped using metalorganic precursors are evaluated.

A review of the theory behind basic surface consumption and mass processes in a CVD reactor is given and standard designs of simple CVD reactors are discussed. The need for plasma enhancement is introduced and important plasma parameters and concepts are shown.

The underlying physics of ECR plasma generation, including the interaction of the plasma with an electromagnetic wave applied parallel to an applied magnetic field and plasma drift in the divergent magnetic field are given. The mechanism of plasma generation through ECR and limiting processes are shown.

Section 2.2: Chemical Vapour Deposition

Chemical Vapour Deposition (CVD) is a process in which gas phase species react on a solid surface in a reaction (or series of reactions) which lead to the production of a new solid phase material [9]. Although various methods and techniques are used to deposit materials through CVD, a simple, illustrative technique is the deposition of silicon dioxide from silane (SiH_4) and oxygen on a heated surface .

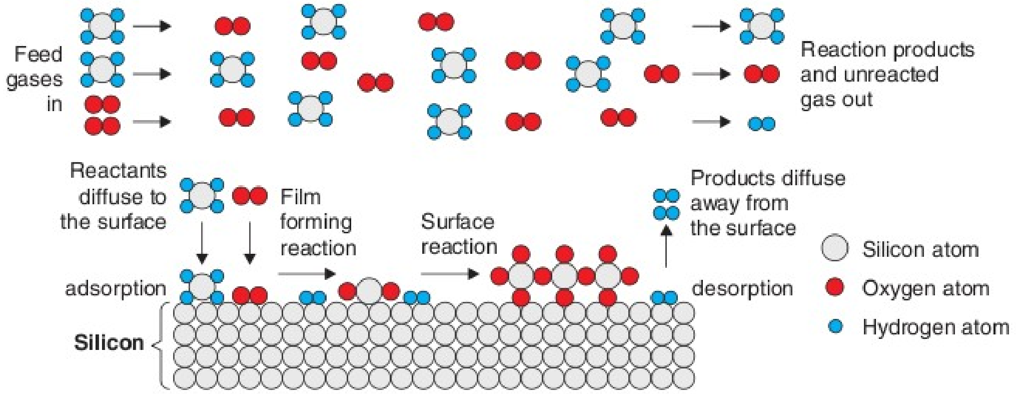

Figure 1: Schematic representation of classical CVD of silicon oxide on silicon using silane and oxygen as source gases [10]

When silane and oxygen molecules come into contact with the heated surface they can either rebound from the surface or be adsorbed. If thermal conditions permit, an adsorbed silane molecule may then gain enough energy to decompose into Si and H_2 and a reaction on the surface will form SiO_2 (eq 1). H_2 is then likely to desorb back into the gas phase, while the silicon dioxide is likely to be left behind building a thin film.

$$SiH_4(gas)+O_2(gas)\rightarrow SiO_2(solid)+H_2(gas) \tag{1}$$

Although most practical CVD reactions are significantly more complex than the above example, with multiple source gases and complex kinetics, the generic process steps taking place in the reaction chamber can be described in a straightforward manner (adapted from [11,12]):

1. The source gases must enter the chamber and be transported to the substrate, with or without intermediate chemical or physical changes
2. Good thermal control of the substrate must be maintained, usually held at a higher temperature than the surroundings to allow selective deposition on the substrate
3. The kinetics of the chemical reactions on the substrate must lead to a build-up of the desired film and the production of byproducts, which will quickly desorb from the film
4. Reaction byproducts must leave the chamber

Section 2.3: Brief Review of Popular Thin Film Deposition Methods

A variety of methods for the growth of thin film silicon based structures exist, so it is worth evaluating the benefits of CVD for the applications discussed in this work.

The three major classifications of thin film deposition methods are [13]:

- Physical Vapour Deposition; such as evaporation, sputtering and molecular beam epitaxy;
- Chemical Vapour Deposition; and

- Purely Chemical Methods; such as Sol-Gel and plating techniques.

Sol-gel coating is a purely chemical method which uses a solid suspension of precursors which is applied to the substrate surface. As the precursors destabilize and react they form a tacky gel which can form a dense film after drying. Sol-gel methods typically form films 50 nm – 1 mm in thickness and usually require high-temperature heat treatments for practical use [13]. The limited variety of materials that can be deposited, thickness of the resultant films, poor chemical purity of films and low uniformity make this an unattractive option for the applications of interest [13].

Electroplating and similar plating techniques are generally wet-chemical processes limited to metals, require a conductive substrate and in any manner could not provide the chemical quality and control required for optoelectronic and photonic applications.

The most important difference between Physical Vapour Deposition (PVD) and CVD is that in a CVD system, a chemical reaction occurs on the substrate surface which leads to a newly formed, adhesive species. In a strictly PVD scheme, no notable chemical changes occur and the adhesion is a more direct phenomenon [14]. Most practical processes exist somewhere in the continuum between strictly CVD and strictly PVD processes. In many processes that are considered PVD, particularly ones involving ionization of the source materials or epitaxial processes, there are in fact surface and gas phase reactions which lead to the formation of the new material films. The distinction between the classification of CVD and PVD processes can be thought of as the relative strength of adsorbtion of diffusively or convectively transported species from vapour sources and surface reactions (CVD) and condensation of the vapour on the surface/film, potentially combined with chemical reactions leading to a stable film.

The simplest physical deposition method is vacuum evaporation. It is widely used to deposit both conductive and dielectric materials for electronic and optical applications. The simplicity of the apparatus gives evaporation a cost-effective edge. Although purely thermal evaporation with electrical heating (such as a heated boat, external wire coil or by applying a current to a wire made of the desired film material) can be used and offers the advantage of even greater simplicity, the need for uniform source heating limits the temperature range that can be used [13].

Another common method employs an electron beam to locally heat an evaporant. Since only a very small volume is heated, less care is needed in preparing containers and surfaces of the source. The lower thermal mass of the volume evaporated and the responsiveness of the electron source allow quick and precise control of deposition rate, a feature of particular interest when depositing multilayer structures.

The deposition of high quality films requires that the deposition occurs in a regime where the mean free path of the atoms and molecules from the evaporant significantly exceeds the distance between the source and substrate. The dimensions of the volume heated by an electron beam relative to the distance between the source and substrate make a point source approximation valid and the system effectively deposits material in a line-of-sight manner. Any area in a “shadow” caused by a step structure on the film or nonuniformity in the growth will be exacerbated. For applications requiring good conformity or applications involving ridged or etched surfaces, evaporative deposition is a poor choice of technique.

Molecular Beam Epitaxy (MBE) can be thought of as an ultra-high vacuum version of vacuum evaporation. MBE requires significantly higher vacuum, often exceeding $5x10^{-11}$ torr [13] to avoid impurities entering the films [15]. In MBE, the mean free path of atoms or molecules in the chamber is more than an order of magnitude larger than the source to sample distance [15]. Since the interaction of the species is negligible in the chamber they are considered to act as a “molecular beam”. Careful sample cleaning and preparation yield a substrate with an effectively single crystalline surface and with extremely careful shutter and source temperature control, the structure is grown epitaxially, monolayer by monolayer. While MBE is a highly reproducible, controllable method of film growth, the extremely low growth rates of MBE make it inappropriate for the growth of the thicker films which would be necessary for commercially deployed silicon-based light sources and photonic materials.

Sputtering is the bombardment of a solid surface with energetic particles, such as ions accelerated through an electric field, knocking the surface atoms out of the solid and causing them to scatter off away from the surface [14]. The technique, similar to physical evaporation, has been used for applying thin metal coatings onto dielectric surfaces since its discovery in 1852 by Sir William Grove [16]. A typical sputtering system used to deposit insulating materials uses a chamber filled with a sputtering gas, usually an inert gas such as argon under a pressure of ~100 mTorr . The sputtering target, which contains the material to be deposited in the film and the substrate are mounted on parallel plates facing each other. The insulating nature of the target would preclude the use of a DC discharge since this would lead to an immediate charge build up on the surface of the insulator, so an RF voltage is applied between the two plates. A glow discharge builds up in the gas between the plates and surface atoms of the target are sputtered from the surface and build up on the target [14].

While sputtering allows the application of thin and thick films from a variety of material groups, it suffers from many of the line-of-sight and conformality issues of other growth techniques. Since the technique relies less on chemical reactions between the growth layers on the substrate the films produced have significant issues with broken bonds and graining effects relative to films grown by CVD methods. The resultant films exhibit poor electrical properties limiting the applicability and final efficiency of electrical and optoelectronic devices produced through this technique.

Chemical vapour deposition relies on chemical reactions occurring on the growth surface (initially at the substrate and then on additional layers of the film) to produce the film. As a result the films tend to have fewer issues with broken bonds and graining effects than films produced by sputtering. In classical CVD processes the main driving force of the growth is the high temperature of the substrate. This necessarily introduces a thermal stress between the film and the substrate once the sample is cooled. Other temperature limiting factors in modern processing techniques include the use of metal interconnect layers and low melting point substrates such as plastics which are being deployed to reduce cost and increase functionality in light emitting devices. The thermal budget of the processing steps does not allow the use of the high deposition temperatures needed for a practical classical CVD system.

Plasma enhanced chemical vapour deposition (PECVD) uses a plasma to provide the energy required for the growth reaction to advance without the need for high temperatures. The plasma breaks down the precursors in the gas phase through ionization and dissociation, creating a flux of free radicals which adsorb onto the surface and can result in acceptable growth rates at low temperatures.

The use of PECVD with silane as a silicon precursor has an additional benefit for growth of materials for electro-optic devices: The deposition incorporates hydrogen, which works to passivate any dangling bonds created in the deposition process [12], further improving electrical characteristics for application in future light sources.

Section 2.4: Deposition System Design Requirements

Although every well-developed thin film deposition method has found practical application in both, materials research, device development and commercial manufacturing, each has advantages and draw-backs in particular applications. It is always important to choose the right tool for the right job and this requires a firm understanding of expectations and design considerations. The development of silicon-based light emitting devices requires a technique which allows for precise control of film structure and composition. High quality films with predictable and uniform chemical make-up and properties are needed and mass-production would require well controlled thickness and film uniformity. When used to create doped silicon oxynitride films, PECVD allows films to be deposited without the non-radiative transitions induced by dopant clustering seen with other methods, such as RF sputtering, and allows more controlled distribution and less matrix damage than would be seen from techniques such as post-deposition ion implantation. These defects tend to reduce the luminescence of the fabricated films. From a research perspective, the technique should be easily adaptable to allow a wide range of material candidates to be investigated with minimal expense and effort required for system retooling. Finally, the technique should be one that is commercially applicable. The method should be adaptable to give good throughput with minimal deviance from design specifications and production quality. Adapting a technology which is widely deployed in the field also gives advantages of technician and engineer experience and familiarity, which minimizes training and allows for developed maintenance and calibration experience to reduce system downtime.

As will be shown in this work, the deposition method used for the following studies fits well into the required application niche. CVD, and in particular the hybrid physical evaporator - Electron Cyclotron Resonance Plasma Enhanced Chemical Vapour Deposition (ECR-PECVD) system - installed and deployed at McMaster has all of the requirements to be an important and effective tool in silicon light emission research.

In order to better understand the operation of the ECR-PECVD system some fundamental processes and characteristics related to CVD will now be described.

Section 2.5: Simplified Surface Consumption Considerations

In an ideal gas, the speeds of individual gas particles are given by the Maxwell distribution, with the most likely kinetic energy being equal to the thermal energy kT giving a mean speed of $c_{mean}=\sqrt{8\mathrm{kT}/\pi m}$. If one were to consider an over-simplified reactor, in which a precursor gas is present and may react to form a film on the wall (or equivalently, the substrate) in the reactor, it would be clear that the rate of the reaction would depend on the number of molecules interacting with an area of the surface in a given time: the flux of molecules to the surface.

Since the molecules are travelling in random directions, a prefactor of ¼ arises from the fact that half of the molecules within the mean free path of the surface are actually moving away from the surface, and the velocity vector of the rest is evenly distributed from being nearly parallel to the surface to being perfectly normal to it, the flux to the surface, J_{surf}, will be:

$$J_{surf}=\frac{n\,c_{mean}}{4} \qquad (2)$$

where n refers to the molar or molecular density of the molecules in the region within one mean free path of the wall. The above equation can be converted to a deposition rate R by using an empirical constant smaller than $c_{mean}/4$, which takes into account the surface reaction probability $K_{surface}$, species concentration n , and the molar film density ρ_m

$$R=\frac{K_{surface}n}{\rho_m} \tag{3}$$

Assuming steady state conditions and ignoring gas phase reactions, we can define certain important characteristic time scales relating to the precursors in the simplified reactor. Under steady state, the number of precursor molecules must be conserved:

$$F_{in}n_{inlet}=K_{surface}S\,n_{chamber}+F_{outlet}n_{chamber} \tag{4}$$

where F_{in} and F_{outlet} are, respectively, the volumetric flow of the precursor into the chamber and pumped out of the chamber and S is the surface area of reaction. The residence time refers to the average time that the molecule resides in the chamber, and ignoring depositions, is given by:

$$t_{res}=\frac{V}{F_{in}} \tag{5}$$

where V is the volume of the reaction chamber. The consumption lifetime t_{con} gives the average time a precursor molecule exists in the chamber without being incorporated into the deposition:

$$t_{con}=\frac{V}{K_{surface}S} \tag{6}$$

where S is the total surface area where the deposition takes place.

It is now of interest to investigate the limiting reactor kinetic cases. If $t_{res} \ll t_{con}$ then there is very little change in the concentration n_{inlet} and n_{outlet}. The deposition is clearly limited by the rate of the reaction on the surface since there is no significant consumption of the precursor in the chamber. The reaction is said to be “surface-limited”

If, however, $t_{res} \gg t_{con}$, the surface is consuming the precursor faster than it is supplied and the reaction is said to be “transport-limited”. Practical control over the surface/transport limited regimes is carried out by control of the gas flows and pumping speed.

Section 2.6: Mass Transport Regimes and Select Dimensionless Parameters

The flow of gases can simplistically be divided into two flow regimes, convective flow and diffusion.

Convection refers to the overall motion of a fluid, such as the movement of air in a breeze or water in a pipe when a faucet is turned on. Diffusion refers to the movement of individual gas particles caused by the thermal motion of the particles themselves. The diffusive flux caused by a concentration gradient (such as a gas-burst pushed into a partially evacuated chamber) is proportional to the gradient and opposes it as given by Fick's First Law:

$$J = -D \nabla \phi(r,t) \tag{7}$$

where ϕ represents the concentration at a location r at time t. J is the particle flux through a given surface, and D is a diffusivity constant. Taking an ideal gas approximation can give significant insight into the factors affecting the diffusivity in a given situation:

$$D \approx \sqrt{\frac{k^3}{\pi^3 m}} \quad \frac{T^{\frac{3}{2}}}{Pa^2} \tag{8}$$

where k is the Boltzmann constant, m is the mass of the molecule, T is absolute temperature, P is the pressure and a is the effective collisional cross-section of the molecules in the gas.

Since in a given region, the concentration must change over time with a net flux, this can be transformed into Fick's Second Law:

$$\frac{\partial \phi}{\partial t} = D \frac{\partial^2 \phi}{\partial x^2} \tag{9}$$

Thus knowing the boundary conditions and initial concentration profile allows the calculation of the concentration profile at later times.

A gas line connected to the partially evacuated reactor chamber can be approximated as an infinite reservoir of the source gas flowing into an infinitely long tube. Simplifying to a one dimensional case, the concentration profile will take the form of a complementary error function [12]:

$$n(x,t) = n_{x=0}\, erfc \frac{x}{\sqrt{4\mathrm{Dt}}} \tag{10}$$

The distance that the gas travelled is given by a characteristic length scale, the diffusion length:

$$L_d = 2\sqrt{Dt} \tag{11}$$

The approximation is valid while t is short enough that the diffusion length is less than the length of the tube/chamber into which the gas is flowing. Even at relatively low vacuum, such as 1 Torr, the diffusivity of gases is on the order of $100\, cm^2/s$ so the approximation breaks down in a matter of seconds.

After this time the solution enters a steady state regime as necessary for uniform CVD growth, where the real concentration gradients become significantly less sharp. In steady state the time derivative of Fick's Second Law must be zero, resulting in:

$$\frac{\partial^2 n}{\partial x^2} = 0 \tag{12}$$

The solutions become linear and the slopes are set only by the boundary conditions.

To determine the relative importance of diffusive and convective transport, the Peclet Number is defined:

$$Pe = \frac{LU}{D} \tag{13}$$

Where L is a characteristic length of the chamber and U is the convective or average fluid velocity. Peclet Numbers significantly less than unity indicate that diffusive flux dominates and the concentration gradients will very nearly be linear. Large Peclet

Numbers indicate that large gradients can exist in the chamber and that convective flux dominates over diffusive flux. It should be noted that since diffusivity depends inversely on the pressure, higher pressures tend to lead to larger Peclet Numbers, predicting that larger gradients and non-linearity are likely to be present. For this reason the deposition of uniform films in a CVD process requires that the system be kept in a pressure regime where diffusive transport dominates.

The Reynolds Number is another important parameter used to characterize the mass transport phenomena in typical CVD systems. While the Peclet Number deals with diffusion of concentration or density, the Reynolds Number describes the diffusion of momentum:

$$Re=\frac{\rho U L}{\mu} \tag{14}$$

Where ρ is the mass density and μ is the kinematic fluid viscosity. A large value of Re indicates that momentum does not diffuse effectively through the chamber and wild variations in flow velocities can be encountered, often associated with re-circulating or turbulent flows. It has been empirically found that Re Numbers on the order of unity relate to smooth laminar flows.

Viscosity is proportional to the product of density and the mean free path which is defined by:

$$\lambda=\frac{1}{\sqrt{2}\pi a^2 n} \tag{15}$$

Where a is the effective collisional diameter of the molecule in the gas. Since the density of the fluid is in the denominator of the mean free path term, viscosity is independent of pressure. The fluid velocity U is inversely proportional to the pressure under a constant molar flow rate and so the Reynolds Number is itself independent of pressure under a constant molar flow.

Since the diffusivity is inversely proportional to pressure, the Peclet Number is also independent of pressure under constant molar flow of a nearly ideal gas. This signifies that in a given system whose gas flows are controlled by a mass flow controller (MFC) or other method that maintains constant molar flow rates both the pressure gradient behaviour and the laminarity of flow will be maintained over wide pressure ranges.

Another important dimensionless parameter used to characterize CVD systems is the Damkohler Number, the ratio of residence time of a precursor to the consumption time. In a system with characteristic width H (perpendicular to the plug flow of the gas, such as tube reactor or precursor delivery line of diameter H), the Damkohler Number is defined as:

$$Da=\frac{K_{surface}H}{D} \tag{16}$$

A small Damkohler Number indicates that diffusion dominates and concentration will not vary much throughout the reactor due to precursor consumption. Since the diffusivity is inversely proportional to pressure, the Damkohler Number will increase at higher pressures and so non-uniformity will increase with operational pressure.

Since lower pressures yield longer depletion lengths, uniformity can be improved using low pressure reactors. The compromise comes with decreased deposition rate, eq 3, since the deposition rate is directly proportional to pressure through the concentration.

The nature of the metalorganic precursors used in this project makes the study of flow in a long narrow pipe of great importance. Even with systems having a low Re, significant differences in the volumetric velocity of gases will develop radially given a significant length of pipe. Since the velocity must be exactly zero at the walls, the fluid viscosity will cause the velocity to decrease near the walls. The situation in a cylindrical pipe is described by Hagen-Poiseuille flow:

$$U(r) = 2\mathrm{U}_{average}(1 - \frac{r^2}{R_c^2}) \tag{17}$$

where R_c is the radius of the pipe or channel. The decreased volumetric flow near the pipe walls increases the effective residence time of the precursor vapour near the walls and increases the deposition rate at a given precursor concentration and temperature.

Section 2.7: Typical CVD Reactor Types

Some of the earliest production-ready CVD reactors, such as the AMS-2100 built by Applied Materials, were designed for atmospheric pressure deposition of SiO_2 [17]. Atmospheric pressure allowed a feed-through style loading, wherein the wafers were loaded onto trays which were continuously fed into a long chamber and the growth zone was heated to ~400°C from beneath by quartz radiant heaters. Gas dispersion systems created an even distribution of reactant gases in the chamber. Preheating occurred under a nitrogen purge and the growth zone was separated from the atmosphere by a high-flow nitrogen curtain. Well controlled substrate temperature, a specialized gas dispersion system and well maintained wafer transport speed provided good repeatability for growths yielding thicknesses in the single micron range.

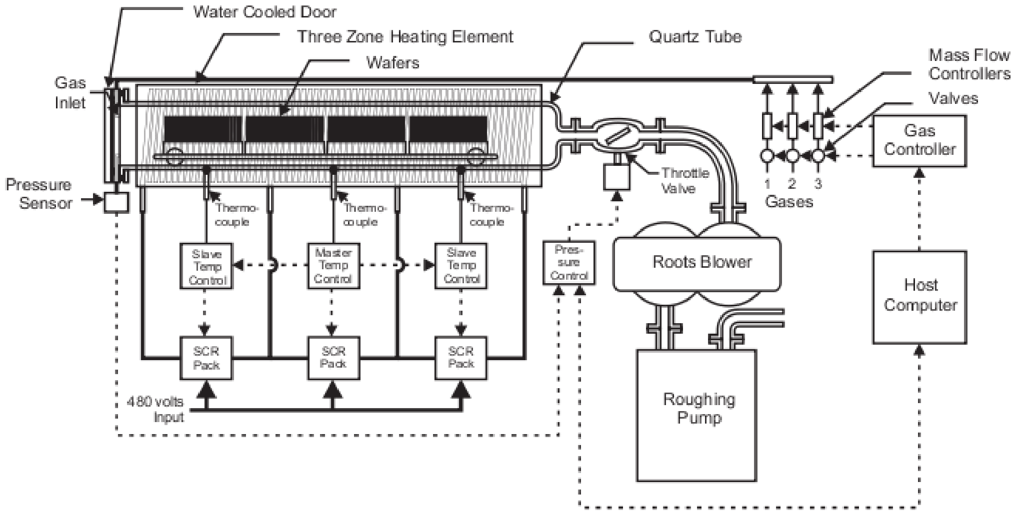

Figure 2: Overview of a modern tube furnace style classical CVD system [10]

Tube reactors are a common design, in which use of low pressure CVD allows the deposition to be surface-limited, which ensures higher uniformity providing that the wafer temperature can be well controlled. The lower pressures, typically in the range of a few hundred mTorr to a few Torr, increase the diffusivity of the reactant gases and allow a large number of wafers to be stacked vertically in a long boat placed into a tube furnace [12]. The large number of wafers in a single batch allows throughput to remain high even with the required pump-downs and complexity added by the vacuum system. A common design of such a system is shown in Figure 2. Depletion of source gases along the length of the boat can be compensated within limits by varying wafer temperature along the axis. Cantilever loading ensures that the boats do not contact the walls of the tube reactor and thus avoid scraping the film off of the walls which would create particulate contamination. The use of cantilevered loading allows many more runs to be performed without the need for a shutdown for cleaning. A vertical arrangement is often used to reduce the mechanical complexity of a cantilever system which must endure the large torque of the boat while allowing precise position adjustment. Vertical systems also give significant savings of expensive clean room floor space.

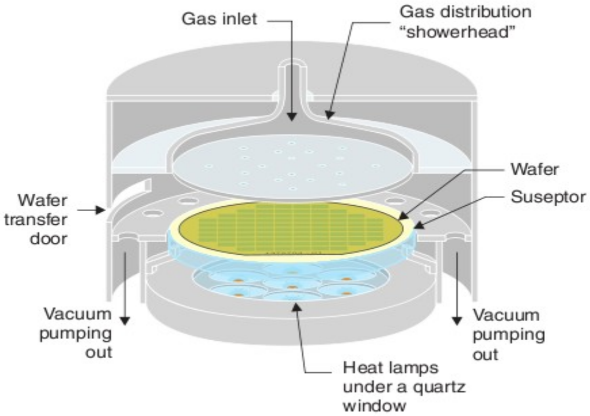

Figure 3: Typical CVD showerhead reactor schematic [10]

Another popular design makes use of the so-called showerhead design illustrated in figure 3. These reactors typically include an annular or disc-shaped gas dispersion system with an arrangement of holes or nozzles to evenly distribute reactant gases in the chamber. Typical operating pressures range from a few mTorr to several Torr. The simple configuration of these reactors make them quite versatile and appropriate for research and small scale production applications, but the large temperature and concentration gradients inherent in the designs make wafer uniformity harder to attain.

The arrangement of holes in the dispersion unit and the height of the chamber significantly affect the concentration distribution as well as flow regimes, radial flow velocities, residence times and consumption times, so very careful design is necessary for uniform deposition characteristics. Many reactors are designed for single-wafer processing and the small chamber dimensions of such a design allows for rapid change of gas conditions which lends itself to the deposition of multilayer films.

Section 2.8: Plasma Enhanced Chemical Vapour Deposition

Section 2.8.1: Motivation

The reaction rates in standard CVD processes are usually controlled by altering the substrate temperature. More recent trends in the semiconductor industry, including the use of multiple layers in devices and integrated circuits, the use of low melting point metals and the low dislocation, stacking fault and vacancy defect levels make the use of high substrate temperatures (>300 °C) an impractical feature of a processing step [9]. Growth phase and film properties are often directly linked to deposition temperature, meaning that full control over the desired film structure and growth rate is not always possible using substrate temperature as the only growth variable. In particular, thermal stress inherent in high temperature depositions needs to be minimized.

Chemical conditions which favour reactions leading to the desired solid-phase film structure can be brought about using sources of energy different than just the thermal energy of the substrate or source gases. A plasma environment can be used to create partially dissociated or ionized reactive species from the source gases formed by electron impact collisions in the plasma [9]. Under careful control, these species are then more likely to follow a reaction path leading to a favourable solid phase being formed on the substrate. Furthermore, the bombardment of the growth surface by positive ions, metastable species and electrons provides a unique physical environment, which, coupled with the surface diffusion and purely chemical reactions occurring, can result in films which are unattainable in purely thermal CVD systems [9].

Section 2.8.2: Plasma for PECVD

A plasma is an ionized gas containing a mixture of positively and negatively charged particles having nearly equal charge densities [18]. Plasmas are commonly found in extremely high temperature systems such as stars, where a gas is heated to such a temperature that the kinetic energy of the individual molecules exceeds the ionization energy. Collisions between gas particles can strip the electrons from atoms or molecules, leaving behind a combination of ions and electrons, with some neutral species [18].

The extreme energies needed to create thermal plasmas make these processes unsuitable for most materials processing techniques, particularly constructive techniques such as deposition. Other methods, such as electromagnetically and optically produced plasmas are more appropriate. Regardless of the plasma production technique, the generation of a steady-state plasma requires an equilibrium to be struck between the ionization and recombination processes in the bulk plasma [18].

In a thermal plasma, the proportion of ionized species is high and all of the species, both ions and electrons are at thermal equilibrium. Electromagnetically generated plasmas are usually considered to be “cold plasmas” [18]. In such a system, an applied electric field is used to couple energy into electrons in the plasma. These gain enough kinetic energy to cause ionization and maintain the plasma. The ratio of ionized species to neutral species in cold plasmas tends to be quite low.

Cold plasmas are characterized by a large difference in the effective temperatures of the electrons and ionized particles. In a cold plasma approximation, the average velocity of particles of a particular species in a given region is uniquely dependent on that species and the forces acting on that species in a particular region [19]. In particular the thermal energies of the ions and neutral species are relatively low while the electron temperature can be on the order of 10^4 K.

While the electrons and ions in a plasma are no longer bound, the plasma itself is “quasi-neutral”. The ionization processes which give rise to the plasma produce an equal number of positive and negative charges and the resulting oppositely charged fluids are strongly coupled to one another. This leads to a situation in which on macroscopic length scales, the plasma gas has no net charge or large scale static electric field associated with it.

Section 2.8.3: Number Density and Plasma Temperature

In a plasma, the complex mix of electrons and various ion species each responding differently to electromagnetic forces makes it is impossible to characterize the plasma with a single density. It is necessary to define an independent number density for each species, n_s, where s denotes the species in question.

One of the most important plasma parameters is the temperature of a species in a plasma. The distribution of particle velocities in a plasma is given by the Maxwell-Boltzmann distribution. This distribution is multinormal, so in any component direction, the velocities will be defined by a Gaussian with standard deviation $\sqrt{kT/m}$ [20]. In thermal equilibrium, the speeds of particles of type s are given by [18]:

$$f_s(v)=n_s\left(\frac{m_s}{2\pi k T_s}\right)^{3/2}\exp\left(\frac{-m_s v^2}{2\mathrm{kT}_s}\right) \tag{18}$$

Where m_s is the mass of the species, k is the Boltzmann constant and the independent behaviour of the species makes it necessary to define an individual temperature for each species T_s. Although these temperatues of individual species will move towards equilibrium, the infrequent collisions in cold plasmas make this approach extremely slow and non-equilibrium effects are dominating.

The average velocity of the particles, each with three degrees of freedom is given by:

$$E_{av}=\frac{3}{3}kT_s=\langle\frac{1}{2}m_s v^2\rangle; \qquad v_{av}=\sqrt{\frac{3\mathrm{kT}_s}{m_s}} \tag{19}$$

A hot, high pressure plasma is in thermal equilibrium and a single temperature can be used to describe the thermal energies of all of the species in the plasma. The large difference in masses of the ions and electrons in a cold plasma allows the electrons to move at a much higher velocity than ions and neutral species. The applied electromagnetic power tends to preferentially heat the more mobile electrons and creates a system where the electron “fluid” has a much larger effective temperature than the ion “fluid”. The temperature of each species can be found by the average kinetic energy of the particles of the species:

$$T_s=\frac{m_s v_{av}^2}{3\mathrm{k}} \tag{20}$$

Section 2.8.4: Plasma Frequency

Although the assumption of quasi-neutrality leads to the view that the plasma is in a state of equilibrium under steady state conditions, this is only true on the macroscopic scale. On the microscopic scale the particles are constantly being perturbed from equilibrium. Large Coulombic restoring forces, however, work to minimize the charge separation.

If one considers a quasi-neutral plasma as the overlap of two gases, one consisting of negatively charged electrons and the other of positively charged ions, whose centres of charge have been separated by a small amount (for example by an externally applied electric field) one would notice a strong Coulombic attraction between the ions and electrons. The heavy mass of the ions makes it reasonable to assume that their motion will be negligible compared to the motion of the electrons and the electrons would accelerate towards the ions. The inertia of the electrons would carry them past the ions and the charge centres would again begin to separate. Barring any energy loss from collisions and other interactions, this process would continue indefinitely in an oscillatory fashion.

The frequency of these characteristic oscillations is known as the plasma frequency:

$$\omega_p = \sqrt{\frac{n_e e^2}{\epsilon_0 m}} \tag{21}$$

where n_e is the electron density, ϵ_0 is the permittivity of free space and m is the mass of the electron. The above relation assumes the mass of ions to be infinite.

The dispersion relation for an electromagnetic wave with wave vector k in a plasma medium is:

$$\omega^2 = \omega_p^2 + c^2 k^2 \tag{22}$$

The plasma frequency effectively represents the lowest frequency that will propagate through the plasma without an external magnetic field, all lower frequencies being absorbed or reflected. By solving eq 22 for the number density, a critical plasma density of propagation of an EM wave of frequency ω can be written as:

$$n_c = \frac{\epsilon_o m_s \omega^2}{e^2} \tag{23}$$

In the ECR-PECVD system, at a frequency of 2.45 GHz, the critical density for plasma heating is ~7.5x10^{10} cm^{-3}.

Section 2.8.5: Debye Length/Shielding

While on a large length scale charge imbalances in a quasi-neutral plasma neutralize, small scale regions of charge imbalance will naturally exist. The length scale over which such regions exist is given by the Debye length. The large ratio of $M_{Ion}/M_{electron}$ gives the electrons significantly higher mobility so it is reasonable to assume that the electrons will move to neutralize the imbalance in the region while the ions remain relatively immobile. The Debye length is [17]:

$$d = \sqrt{\frac{k T_e \epsilon_0}{e^2 n_e}} \tag{24}$$

where ϵ_0 is the permittivity of free space and n_e is the mobile carrier (electrons in a cold plasma) density. For low pressure systems, the Debye length can be quite large. A dependence on T_e is expected since random thermal motions compete with the Columbic restorative forces. It is also natural that higher electron densities should reduce this length since more electrons are available in the immediate region so a shorter translation is required to neutralize the region. For typical ECR-PECVD electron temperature and pressure ranges, the Debye length is on the order of 5x10^{-5} m [21].

The Debye length determines the depth to which a strong electric field can be screened by the mobile charge carriers in a plasma. In effect, this length gives a scale to which a strong electric field can penetrate from a surface into the plasma, and defines the distance over which significant charge separation can be observed.

Section 2.8.6: Skin Depth

High frequency electromagnetic signals do not penetrate into the depth of a conductor and tend to be carried on the surface, with very little current flowing through the core regions. In an ideal magnetohydrodynamic plasma, all of the current would be transmitted through an infinitely thin layer at the plasma-vacuum boundary [19].

In a conductor, the depth to which the amplitude of an electromagnetic wave penetrating into the surface of the conductor falls to 1/e of the incident amplitude is given by the well-known skin depth equation:

$$\delta=\sqrt{\frac{2}{\mu_0 \omega \sigma}} \tag{25}$$

where ω is the angular frequency of the applied wave, μ_0 is the vacuum permeability and the electrical conductivity of the material is given by σ .

The large number of quasi-free electrons in the plasma allows the plasma to be considered a conductor. Low frequency fields do not propagate well through the plasma since this would require a large charge migration of the electrons. At frequencies above the plasma frequency, the conductance of the plasma is much greater, and the signal travels along the skin depth given by the above equation.

Section 2.8.7: Plasma Sheath

A low pressure plasma, such as those seen in typical PECVD tools, exhibits three major regions. The bulk region, in which the quasi-neutrality assumption holds well, a pre-sheath region and a sheath region which is found near reactor walls [21].

The electropositive sheath region is formed as a consequence of the higher mobility of electrons compared to ions in the plasma. In a plasma boundary region near a reactor wall, stage or substrate, electrons move at much higher velocities than ions and the flux of electrons onto the wall is much greater than the flux of ions. This leads to a net negative charge buildup on the surface of the reactor walls (which have a thin dielectric coating from prior depositions). The potential resulting from this serves to reduce the electron flux and draws a larger ion flux in the regions nearest the wall. This continues until the fluxes balance and no net current to the surface is present [19]. This equilibrium requires that the region nearest the wall have a net positive charge so that in the sheath region $n_i \gg n_e$.

In the pre-sheath region, the quasi-neutrality of the plasma is maintained but a notable electric field is present. It can be considered a transition layer between the quasi-neutral bulk plasma and the charged sheath region. The Bohm sheath criterion requires the ion velocity in the pre-sheath region to exceed the acoustic ion speed (the speed determined by the Maxwell-Boltzmann distribution, eq 18):

$$c_s = \sqrt{\frac{T_e}{M}} \tag{26}$$

where M is the ion mas and T_e is the electron temperature. The total potential drop over the pre-sheath region must exceed $T_e/2\mathrm{e}$, however, the total dimension of the pre-sheath region is difficult to determine and depends on the size of the reactor as well as the pressure dependent mean free path [21]. While the sheath region scales with the Debye length, the pre-sheath region is usually much larger, having dimensions comparable to the collisional mean free path of the electrons.

Section 2.8.8: Larmor Radius and Cyclotron Frequency

When a static magnetic field is present in the plasma, charged particles will be forced into an orbit around a magnetic field line by the Lorentz force caused by the magnetic field and particle velocity:

$$\vec{F} = q\,\vec{v}\,x\,\vec{B} \tag{27}$$

The radius of such an orbit, known as the Larmor radius, will be given by:

$$r_L = \frac{v_{perp}\, m}{q\, B} \tag{28}$$

Where v_{perp} is the particle velocity perpendicular to the direction of the magnetic field, m is the mass and q is the charge.

Since the radius is dependent on the mass of the particle it tends to vary greatly between ions and electrons. For example, in deposition systems similar to the one described in this work, electrons with a temperature of 10 eV will have a Larmor radius of approximately 100 µm while a N ion with the same energy will have a radius of 2.2 cm [22].

While the radius of orbit will vary with velocity and particle energy the frequency of the oscillation, known as the cyclotron frequency, will depend only on the strength of the applied magnetic field:

$$\omega_c = \frac{eB}{m_e} \tag{29}$$

Section 2.8.9: Electromagnetic Waves Parallel to an Applied Magnetic Field in a Plasma

Plasma heating by electron cyclotron resonance is a complex phenomenon which requires an understanding of the behaviour of electromagnetic waves travelling through a plasma parallel to an externally applied magentic field $\vec{B}_0$. An electromagnetic wave propagating along the z-axis with transverse components E_x, E_y:

$$\vec{E} \propto \exp[i(\vec{k}\vec{r} - \omega t)]; \vec{k} = k\,\hat{z}; E_1 = E_x\hat{x} + E_y\hat{y} \tag{30}$$

where $\hat{x}$, $\hat{y}$ and $\hat{z}$ are unit vectors.

The electron motion can be described by the Lorentz force, giving an equation of motion:

$$i\,m\,\omega\,\vec{v}_e = e(\vec{E} + \vec{v}_e \times \vec{B}_0) \tag{31}$$

The wave equation in the plasma is:

$$-\vec{k}(\vec{k}\,\dot{\vec{E}})+k^2\vec{E}=\frac{i\omega}{\epsilon_0 c^2}ne\vec{v}_e+\frac{\omega^2}{c^2}\vec{E} \tag{32}$$

Separating the vector components and solving the above two equations leads to the dispersion relation:

$$\tilde{n}^2=\frac{c^2k^2}{\omega^2}=1-\frac{\omega_p^2/\omega^2}{1\mp(\omega_c/\omega)} \tag{33}$$

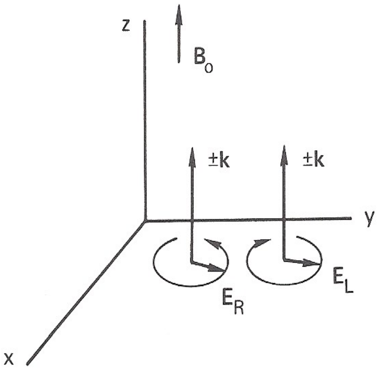

Figure 4: Geometry for right and left polarized waves in an ECR plasma generation system [23]

The two solutions in the above equation represent the two cases where E_y leads or lags E_x by 90º, respectively. This corresponds to the two circular polarizations of the electromagnetic wave (Figure 4):

$$\tilde{n}^2=1-\frac{\omega_p^2/\omega^2}{1-(\omega_c/\omega)}\quad[R\,polarized\,wave] \tag{34}$$

$$\tilde{n}^2=1-\frac{\omega_p^2/\omega^2}{1+(\omega_c/\omega)}\quad[L\,polarized\,wave] \tag{35}$$

These are the principal electromagentic waves propagating along $\vec{B}_0$. Below a critical frequency ω_L , dependent on the applied magnetic field, the L polarized wave will not propagate in the plasma since the refractive index is purely imaginary as shown in Figure 5. This is seen as the region where the L-wave inverse dielectric constant in the plasma approaches infinity. Examining eq 35 shows that there is no resonance in the L wave for positive ω . This is clear when one considers that the L-wave is in effect rotating in the opposite direction of the electrons in the plasma. If ion motions were considered in the above equation, a resonance condition between the ion orbits and the L-wave would be found but for simplicity and given the small dimension of these orbits, they are ignored.

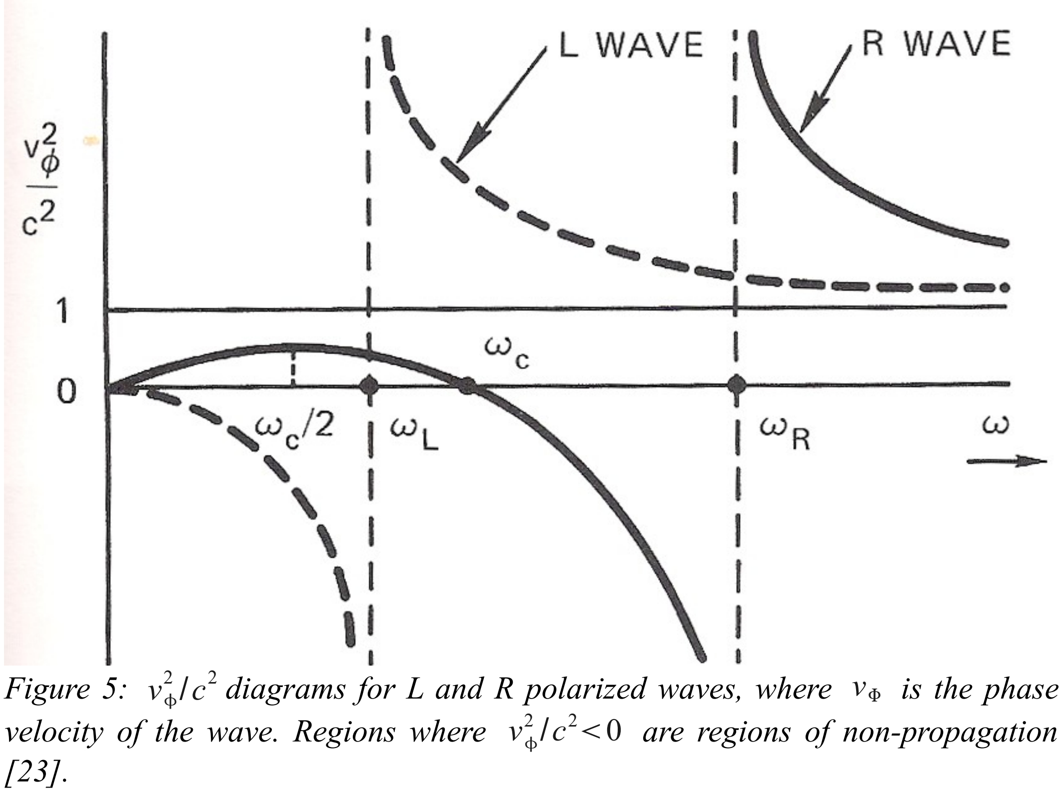

Figure 5: v_Φ^2/c^2 diagrams for L and R polarized waves, where v_Φ is the phase velocity of the wave. Regions where $v_\Phi^2/c^2<0$ are regions of non-propagation [23].

The behaviour of the R wave as seen in figure 5 is much more interesting. There is a stop-band for the propagation of the R-wave between ω_c and ω_r and there is a second, low-frequency allowed propagation band between 0 and ω_c. This is known as the whistler mode, named after the audible whistle sometimes generated in radio receivers by waves travelling through the ionosphere after a lightning strike.

Of particular interest is the resonance found at ω_c. In this case, k approaches infinity as the electromagnetic wave approaches the electron cyclotron frequency. Since the R-wave is rotating in the same direction as the electrons in the orbit, the wave is constantly losing energy by accelerating the electrons and so cannot propagate a far distance into the medium.

Section 2.9: Plasma Generation by Electron Cyclotron Resonance for PECVD

The above resonance is exploited for plasma generation in the ECR-PECVD system, whose design details are discussed in Chapter 5. The electromagnet generates a magnetic field of 875 G in the central region parallel with the axis of the cylindrical plasma chamber slightly downstream from the magnet (Figure 6). The microwave is fed through a quartz window near the centre of the magnet axis. Source gases, such as Ar, O_2 and N_2 are allowed to flow into the plasma chamber through small pinholes around the perimeter of the quartz window. The applied microwave frequency is slightly lower than the cyclotron resonance frequency in the area of high magnetic field so the R waves will

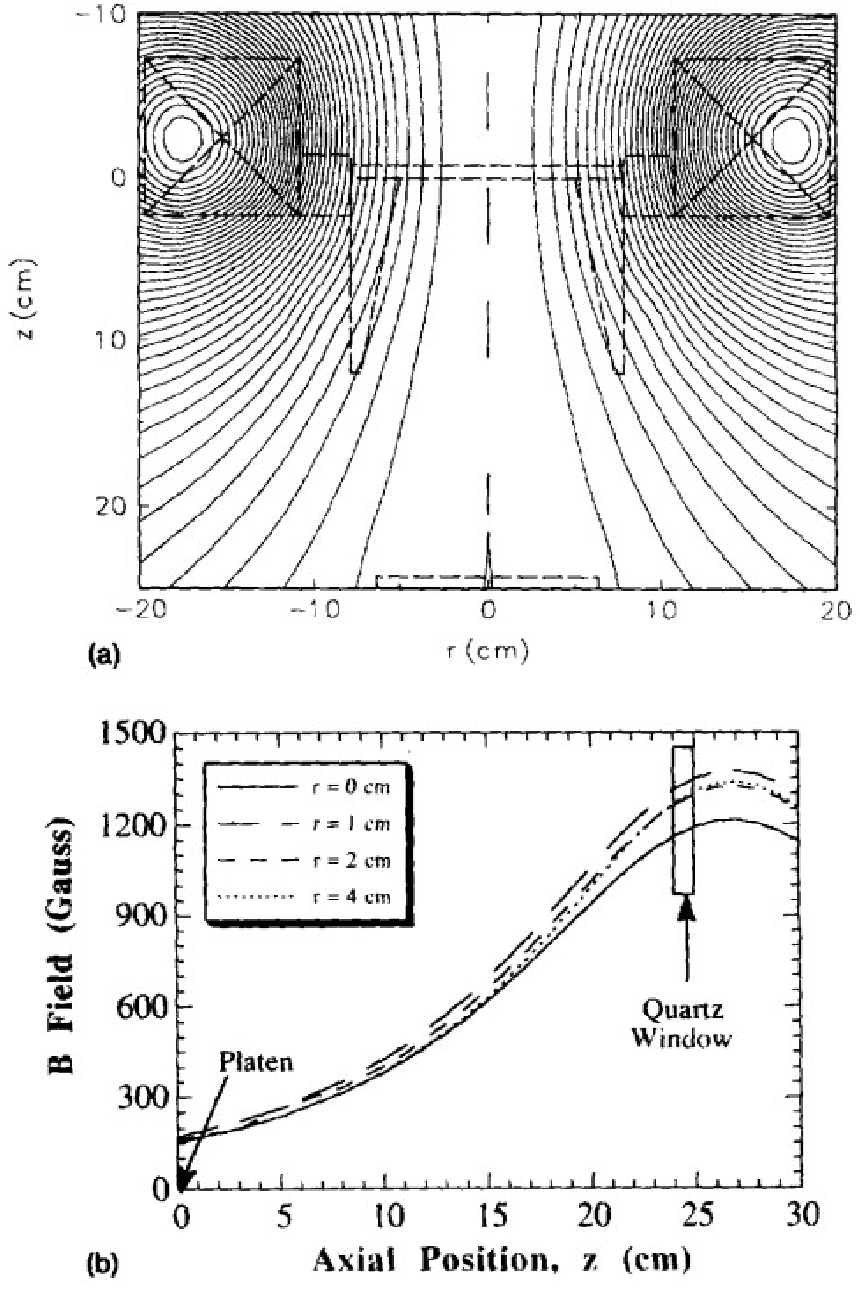

Figure 6: (a) Magnetic field line profile and (b) magnetic field strength as a function of distance from feedthrough window for ASTEX magnet at 180 A. Note that magnet alignment may differ slightly in the system discussed so axial position scale may be offset [24].

propagate in the falling edge of the whistler mode, near ω_c where much of the energy will be absorbed by accelerating the electrons. The microwave frequency is below ω_l in the plasma generating region, so the L-wave will not be allowed to propagate, but will be reflected back into the microwave waveguide. By setting the tuner stubs of the waveguide to match the impedance of the plasma, the reflected energy will be returned to the chamber as an R-polarized wave, thus reducing the reflected power measured.

When the plasma is ignited, a chance free electron in the chamber will accelerate under the influence of the applied microwaves. Since the electron is effectively trapped in an orbit around a particular magnetic field line by the Lorentz force, the acceleration will be perpendicular to the magnetic field line, tangential to the orbit. Since the radius is proportional to the tangential electron velocity, it will increase causing the electron to move in a tight spiral pattern.

The energetic electron colliding inelastically with a gas molecule may cause the excitation or ionization of the gas molecule. In the case of monoatomic species such as Ar, the behaviour is simpler since only electronic level excitations and ionization can result from these inelastic collisions. In the case of more complex species, the excitation of vibrational and rotational modes as well as ionization and dissociation are also available, allowing for more ways for the absorbed microwave energy to be dissipated. This can have significant effects of the stability and conversion efficiency of the plasma.

Section 2.9.1: Plasma Drift

Outside of the cyclotron heating region, the magnetic moment of the gyrating particle will remain constant as long as the spatial variation of the magnetic field over a distance on the scale of the Larmor radius is small compared to the field strength. The particle caught in an orbit in the magnetic field will have a magnetic moment given by $\mu = m v_{\perp}^{2} / 2\mathrm{B}$ which is adiabatically invariant. By considering only the motion of the guiding centre of the orbit near the centre of a diverging magnetic field, the motion of the particle can be separated into an orbital velocity, $v_{\perp}$ and the velocity parallel to the magnetic field given by $v_{\parallel}$. Assuming the magnetic field is in the z direction, the force on the particle will be [25]:

$$F_z = -\mu \frac{\partial B}{\partial z} = \frac{m v_{\perp}^{2}}{2\mathrm{B}} \frac{\partial B}{\partial z} \qquad (36)$$

Since the total energy of the particle must remain the same in the absence of electric fields, the effect of the adiabatic invariance of the magnetic moment of the particle and the magnetic gradient is a transfer of energy from the orbital motion to the motion parallel to the gradient. Thus a particle moving towards a region of increasing field density will slow down and be reflected if it does not have enough parallel momentum, as in a magnetic bottle. In the case of the ECR system geometry, the highest magnetic field density is found near the plasma heating area and so the particles will be accelerated away from the plasma chamber towards the substrate.

Section 2.9.2: Recombination and Sidewall Collision

Since the electron heating by the ECR source drives the plasma density higher, it is clear that there must be processes which work to reduce the density. During a collision between an electron and an ion at low relative speeds there is a finite probability of ion-electron recombination. Conservation of momentum dictates that a third body must be present for this process. In the case where this is satisfied by the release of a photon, the process is known as radiative recombination [26]. If it is satisfied by another particle it is referred to as three-body recombination. The rate of ion-electron recombination is proportional to the number density of both ions and electrons and so, in a quasi-neutral plasma (where ion and electron densities are equal) the continuity equation dictates:

$$\frac{\partial n}{\partial t} = -\alpha_r n^2; \tag{37}$$

where α_r is the recombination coefficient in units of cm^3/sec.

After the plasma density has fallen far below the original value, the density will continue to decrease reciprocally with time.

Electron attachment, sometimes associated with negative ionization or dissociation can serve to drive down the electron density in a plasma and will be proportional to both the attachment collision frequency and electron density [27]. Charge conservation principles, however, dictate that this will not have an effect on the overall density or neutrality of the plasma.

Interactions between the plasma and sidewalls are an important set of processes that causes a reduction in the overall plasma density. While the deposition of the plasma constituents on the target are the end-goal of the system discussed, these interactions are generally counter-productive to plasma generation. Drift of the electrons along the magnetic field discussed above removes the highly mobile electrons from the plasma generation regions. The less mobile ions are much less affected by this drift. If one, however, considers the motion of the electron and ion gases, it is clear that the separation of the two gas volumes cannot significantly exceed the Debye length. The drift induced motion of the electrons would cause a charge separation which would in turn create a quasi-local electric field whose effect would work against the separation, effectively increasing the drift of the ions at the expense of slowing down the electrons.

The final loss mechanism considered is the diffusion of the species across magnetic field lines. Since in the plane normal to the magnetic field, the motions of ions and electrons are restricted to their specific orbit, only collision events can cause cross-field diffusion. The large difference in the Larmor radius of the ionic species and electrons causes the cross-field diffusivity of ions to be much greater than that of electrons. This type of diffusion is intuitively a random-walk process and can be shown to be proportional to r_l^2. The cross-field diffusion coefficient can be given as:

$$D_\perp = \frac{D}{1+\omega_c^2\tau^2}$$

where τ is the mean time between collisions.

Section 2.10: Conclusions

The choice to use ECR-PECVD as a deposition system for research in silicon based optical materials has been justified by comparison to other common thin film deposition methods and by examining the design requirements for a system capable of these growths. Basic CVD mass transport was reviewed and typical classical CVD reactor designs were presented as a comparison to the system which will be described in the following chapter.

The need for PECVD as a growth method, which allows the deposition of the needed materials within a practical thermal budget, was highlighted and important plasma characteristics and physics related to PECVD were presented. The physics related to the generation of an ECR plasma including the interaction of the plasma and electromagnetic waves in an applied parallel magnetic field, plasma drift and major density limiting processes have been introduced to facilitate a discussion of the actual ECR-PECVD system installed.

Chapter 3: Review of Related Materials Sciences

This chapter reviews select physical and optical properties of amorphous silicon oxynitride films. The focus will be on structural and optical properties, which are related to the work presented in this thesis.

Section 3.1: Silicon Oxinitrides

Both the physical and optical properties of films of silicon oxynitride, SiO_xN_y, vary with composition and deposition method. General observations on the film properties can, however, be made by looking at the two stoichiometric limits of the composition, SiO_2 and Si_3N_4.

Of particular interest to microelectronic and photonic applications is the fact that by varying the composition to an intermediate composition between the binary end points, physical and optical properties can be varied, specifically the refractive index. This allows for certain applications such as graded refractive indexes and anti-reflective coatings. Ignoring the incorporation of hydrogen into the films, a parameter can be defined to describe the relative concentration of the silicon–oxygen bonds to total bonds in a silicon oxynitride [28]:

$$\alpha = \frac{2x}{2x + 3y} \tag{38}$$

This compositional parameter may be easier to understand if the SiO_xN_y film is rewritten as $(SiO_2)_\alpha(SiN_{1.33})_{1-\alpha}$ where it can be clearly seen that with $\alpha=0$ the composition is stoichiometric silicon nitride and with $\alpha=1$ the composition becomes pure stoichiometric silicon dioxide.

Section 3.2: Si_3N_4 and SiO_2

One of the most successful models used to describe bonding within SiO_xN_y films is the Random Bonding Model (RBM) originally proposed by Philipp [29] for SiO_x materials. This model assumes that the material is composed of standard (if highly distorted) corner-sharing tetrahedral structural units with silicon at the centre and oxygen and nitrogen at the vertices. In effect the material is then assumed to be of the form $Si-(Si_xO_yN_z)$. The five primary tetrahedra being labelled j=0..4 correspond to SiO_jN_{4-j}. The probability or relative concentration of each tetrahedron is given by [30]:

$$P_j=\binom{4}{j}\alpha^j(1-\alpha)^{4-j} \tag{39}$$

Carbon impurities are of particular interest for films grown with metalorganic precursors. At low concentrations the carbon impurities effectively tend to replace the silicon and with increasing carbon concentration bond to the silicon following the random bonding model.

It is clear that the amorphous structure, with a lack of long range crystallinity as well as local variations in composition and the inclusion of carbon impurities all necessarily cause the formation of dangling bonds which are passivated by hydrogen from the silane precursor. An assumption of near-stoichiometry necessitates that non-interstitial hydrogen concentrations in the films are low so the majority of hydrogen will be interstitial. The actual concentration of hydrogen incorporated from the silane precursor used for the deposition of the films is difficult to ascertain using the characterization techniques used.

The situation is further complicated by the deviation of films from stoichiometry. Of particular interest is the formation of silicon nanoclusters and nanocrystals by the precipitation of silicon during deposition [31] and particularly during post-deposition annealing of silicon rich films. These materials can be thought of as intermediate combinations of the two compositions [32]. The large bandgaps of SiO_xN_y can serve well as a bandgap barrier leading to quantum confinement in nanocrystals a few nm in size. The excess silicon also serves to increase the extinction coefficient of the films.

As one would expect from the higher density of the crystalline form of silicon dioxide, quartz, the refractive index is higher than the amorphous form, ($n_{quartz}=1.55$, $N_{a-SiO_2}=1.46$ at 633 nm [33]). The refractive index of silicon nitride films is generally found to lie between 2.0 and 2.1, being more sensitive to density and deposition characteristics [34].

Section 3.3: Use of Silane as Si Source, Chemistry of SiO_2 Deposition

The chemical environment during deposition inside the reactor is an incredibly complex one. Even if one considers one of the simplest films commonly deposited using ECR-PECVD, the formation of a SiO_2 film using SiH_4 and O_2/Ar as precursors the reactor kinetics become overwhelmingly complex. One study [35] aimed at understanding the dynamics of the chemical reactions occurring in a reactor identified 167 *major* reactions occurring simultaneously in the gas phase as well as 96 major surface reactions. For many of the intermediate and metastable species reliable reaction rate measurements are nearly impossible, so theoretically calculated and semi-empirical extrapolation were used for reaction rates.

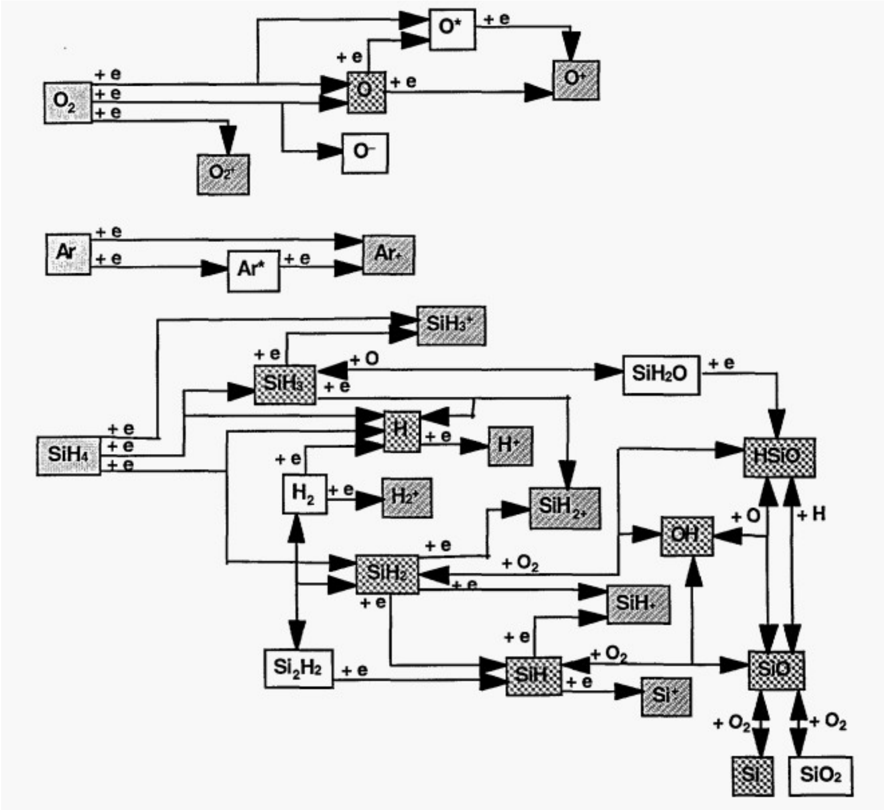

Figure 7: Dominant gas phase reaction paths in the PECVD of SiO_2 from SiH_4 and O_2 in Ar [35]

In the gas phase, electron-impact reactions, caused by the plasma and leading to the creation of ionized species; neutral species reactions, which occur in the gas phase and ion-neutral molecule reactions must all be accounted for. Dominant reaction paths in the gas phase are summarized in Figure 7.

The set of reactions occurring on the surface of the substrate is also quite complex. Neutral species' reactions with surface sites; ion-surface interactions, including adsorption, ion-induced desorption (and out-gassing); thermal and random desporption as well as physical surface sputtering by ion bombardment all need to be considered.

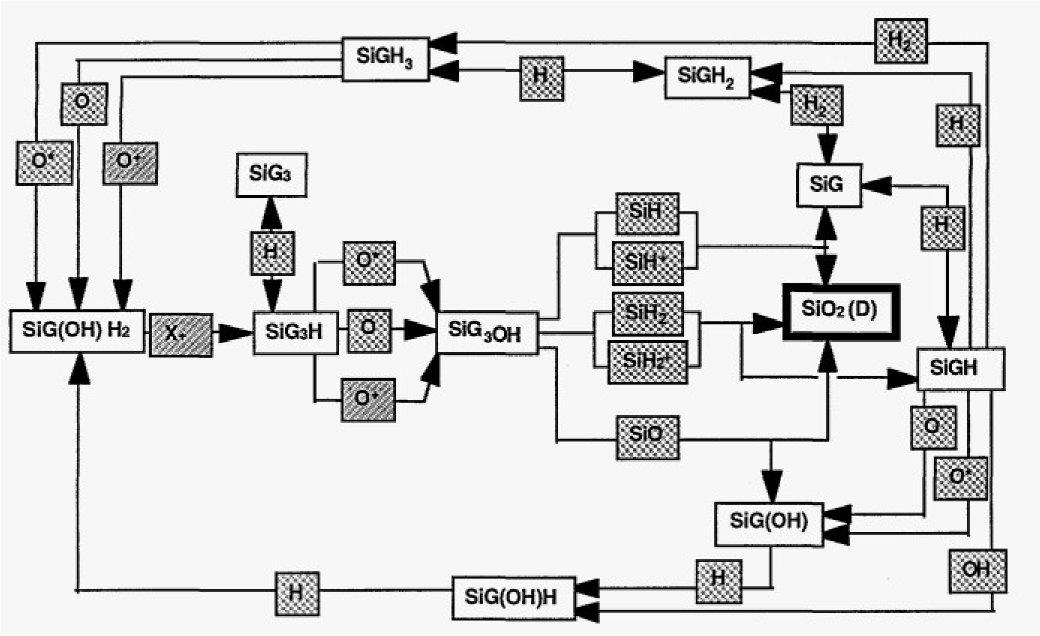

Figure 8: Dominant surface reactions in the deposition of SiO2 by PECVD from SiH4 and O2 in Ar. G represents an oxygen atom that is shared with another silicon atom [35]

To further complicate the situation, reactions with the reactor walls also form a significant portion of the kinetics as do reactions with the sidewalls. Dominant surface reactions for the deposition of SiO_2 from SiH_4 and O_2/Ar are summarized in figure 8.

To the author's knowledge dynamic models of the growth of SiONs of similar depth have not been attempted. It is, however, clear that the addition of an entirely new group of species resulting from the availability of nitrogen bonding would create an even more complex system.

Section 3.4: Material System Choices:

The material systems chosen for these studies are cerium doped silicon oxynitrides and aluminium doped silicon oxides.

Cerium-doping is needed for the production of white light from rare-earth doped silicon because of its contribution of blue emission. While the production of white light would require the co-doping of the base material with other rare-earths such as europium and terbium, cerium was chosen due to our experience in the deposition of cerium-doped materials using the precursor in an existing ECR-PECVD reactor in the same laboratory.

Aluminium and cerium co-doping of silica glasses has been shown to lead to higher fluorescent yields [36]. The incorporation of aluminium leads to higher proportions of Ce^{3+}, the optically active bonding arrangement, relative to Ce^{4+}, an optically inactive bonding arrangement [36,37]. The result is a higher density of Ce^{3+} incorporated into the silicon-based matrix without efficiency limiting clustering. This higher density leads to stronger optical emissions, and narrower and blue-shifted emission band [36,37].The combination of these improved luminescence properties with the precise compositional control, conformality, and favourable electrical and optical properties offered by ECR-PECVD silicon based material offers the potential for the fabrication of practical silicon photonic devices.

For this reason, the system is designed to allow the co-doping of silicon oxides with Al and Ce. To have controlled growths of co-doped materials, the depositions of Al-doped films should be investigated. The preliminary studies discussed in this thesis were focused on Al-doped films as a stepping stone towards Al and Ce co-doped structures of interest for electroluminescent silicon based devices.

Section 3.5: Doping

In situ doping of the silicon based materials cannot be directly carried out since the dopants of interest, in this case cerium and aluminium are not available in a gaseous or readily volatile state. This makes their application in CVD, by definition a gas-phase to solid-phase reaction, impossible without intermediate precursors.

Doping is accomplished using metal-organic precursors, which combine the metal with a complex organic ligand to form a compound volatile enough to use for a CVD process. Ideally the molecule would have fairly weak bonds joining the metal atom to the ligand so that the plasma would selectively crack the bonds holding the metal and leave the large, fairly passive ligand to be quickly pumped away.

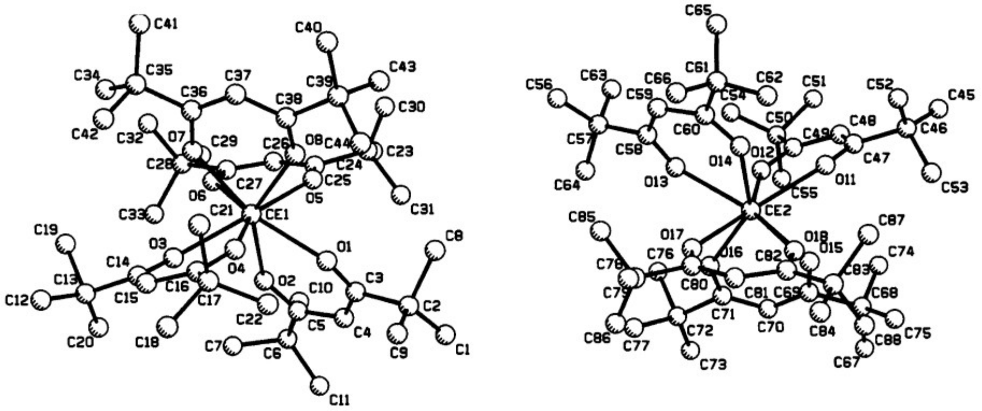

Figure 9: Two isomers of the Ce-TMHD$_4$ precursor[38]

The precursor Tetrakis(2,2,6,6-tetramethyl-3,5-heptanedionato)- cerium(IV), a rare-earth β diketone, froms a monoclinic crystal structure with two discrete $Ce(C_{11}O_2H_{19})_4$ molecules shown in figure 9 [38] . The compound itself appears as a red powder, with a melting point between 275 and 280ºC and a boiling point of 285ºC. The vapour pressure of the compound by sublimation at 140ºC is 0.05 Torr [34]. Since the cerium atom is initially in the tetravalent arrangement, bonded to four oxygen atoms, it is likely to adsorb and bond to the surface in a tetravalent arrangement in the silicon oxynitride. Since it is lacking both 4f electrons, the Ce^{4+} ion will be optically inactive while the lone 4f electron of the Ce^{3+} allows for a 5d-4f transition. For this reason Ce^{3+} structures are known to give strong emission [39]. Since the cerium is expected to incorporate mainly in the Ce^{4+} arrangement, it is expected that the as-deposited samples should not exhibit notable photoluminescence. Post-deposition annealing causing reduction of the Ce^{4+} ions cause a recoordination of the cerium Ce^{3+} in the silica/nitride matrix.

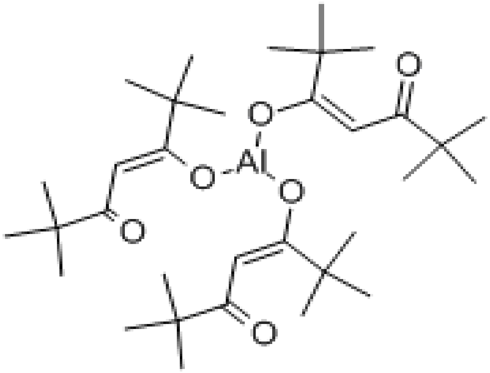

Figure 10: Chemical structure of Tris(2,2,6,6-tetramethyl-3,5-heptanedionato)aluminum used for aluminium doping [40]

The aluminium doping was carried out using Tris(2,2,6,6-tetramethyl-3,5-heptanedionato)aluminum, $Al(C_{11}H_{19}O_2)_3$ ($Al(TMHD)_3$), shown in figure 10. The material itself is a white crystalline powder with a melting point between 255 and 258° C and a boiling point above 400º C. The sublimation vapour pressure is 0.01 Torr at 150º C, significantly lower than that of the $Ce(TMHD)_4$. The ligands are the same as the cerium precursor, however, the molecule itself is smaller since the aluminium is bonded to only three of the ligands [40].

Chapter 4: Characterization Techniques

Section 4.1: Ellipsometry

The use of light as a probe to measure the thickness and optical properties of thin films is a concept which has existed for a long time. Brewster, in "*A Treatise on Optics*" [41] notes that by using white light obliquely incident on thin slabs of transparent materials (such as oil, air or spirits) Sir Issac Newton was able to calculate the thickness of the materials with a precision of millionths of an inch and relate the change in the position of rings of various colours to the relationship between the refractive index of air and the material being measured. The use of the measurement of the phase difference of perpendicularly polarized light beams and hence the development of interferometry into true ellipsometry did not occur until much later. In 1945 Alexandre Rothen introduced the name ellipsometer when he described the use of the change in ellipticity of light reflected from a thinly coated metal slide to determine the thickness of the film to an accuracy of a fraction of a monolayer, an order of magnitude better than interferometric methods would allow [42].

Ellipsometry as a characterization technique offers many benefits. The measurements are non-destructive, are minimally time consuming, require no special sample preparation and can yield large amounts of information about the film. The wide availability of lasers as an intense, coherent and highly monochromatic light source has significantly reduced the complexity of single wavelength ellipsometry (SWE), a technique which can measure film thickness with an accuracy that can distinguish fractional monolayers of well understood growths [43]. This technique, however, suffers from a periodicity problem for thicker film samples [44], which will be discussed later.

Spectroscopic ellipsometry (SE) enabled through the use of a broadband light source allows the measurement of the phase difference using more than one wavelength to avoid periodicity issues observed in SWE. When measurements are taken over a number of incident angles, variable angle spectroscopic ellipsometry (VASE) provides more data for modeling allowing for the measurement of a variety of material types including multilayer samples.

Section 4.1.1: Basic Principles of Ellipsometry

An electromagnetic wave is a transverse wave consisting of both an electric field and magnetic field vector which vary in time and position. The electric and magnetic field vectors are always perpendicular to each other and the direction of propagation of the wave. Since the electric and magnetic field vectors are related by Maxwell's Equations, having a complete description of one allows the determination of the other. For this reason, it is customary to ignore the description of the magnetic field and consider only a mathematical description of the electric field.

Although many descriptions of an electromagnetic wave exist, for the applications discussed here, it can be written as:

$$E(z,t)=E_0\sin\left(\frac{-2\pi}{\lambda}(z-vt)+\xi\right) \tag{40}$$

where E_0 is the amplitude of the electric field, λ is the wavelength, v is the wave velocity, z is the distance along the direction of propagation of the wave and ξ is an arbitrary phase angle offset.

A more general, three dimensional case of an electromagnetic wave propagating through a medium can be written as:

$$E(r,t)=E_0\exp\left(\frac{-j2\pi\tilde{N}}{\lambda}\hat{q}\cdot r\right)\exp(-j\omega t) \tag{41}$$

where $\tilde{N}$ is the complex refractive index, $\hat{q}$ is a unit vector indicating the direction of propagation, ω is the angular frequency of the wave and r is the position vector.

Since a direct measurement of the amplitude of an electromagnetic wave is not possible for most cases, the intensity, I, which represents the energy transferred across a unit area perpendicular to $\hat{q}$ is measured. This quantity is proportional to E_0^2.

The complex index of refraction is a property of the medium through which the wave travels and can be separated into two components:

$$\tilde{N}=n-jk \tag{42}$$

where the real part, n, is the ratio of the speed of light in free space to the speed of light in the medium of interest and the imaginary component, k, is the extinction coefficient describing how quickly the wave is attenuated in the medium and is related to a standard Beer-Lambert absorption coefficient α [45]:

$$k = \frac{\lambda}{4\pi}\alpha \tag{43}$$

When light is incident upon the surface, part of it will be reflected at an angle equal to the angle of incidence as measured from the surface normal. Part of the light may, however, penetrate the surface and propagate through the medium at a modified angle. This phenomenon, known as refraction is described by Snell's law:

$$\tilde{N}_1 \sin\phi_1 = \tilde{N}_2 \sin\phi_2 \tag{44}$$

where the subscripts denote the different media and ϕ denotes the angle of propagation measured from the surface normal.

Each photon of light will have an associated electric field vector which describes the plane of oscillation of the electric field. Most light sources, including incandescent ones, give off photons whose electric field direction is random. Such light is known as unpolarized light. If, however, all of the photons have an electric field oscillating in the same plane the light is referred to as linearly polarized light.

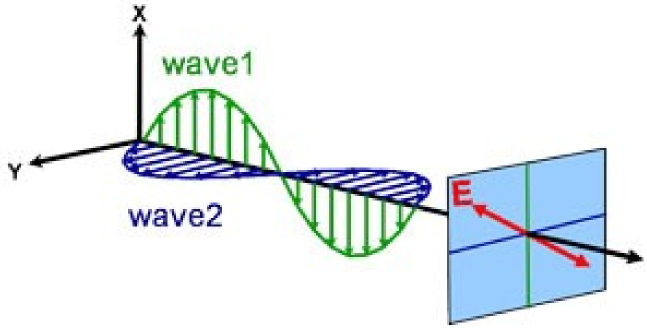

Figure 11: Linearly polarized light at 135° [46]

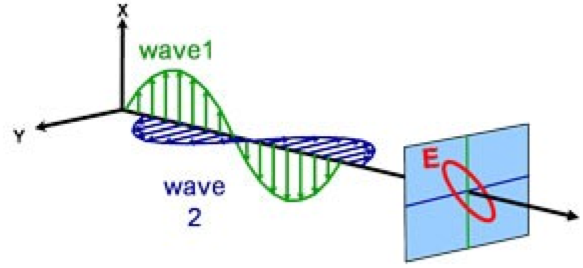

Figure 12: Elliptically polarized light[43]

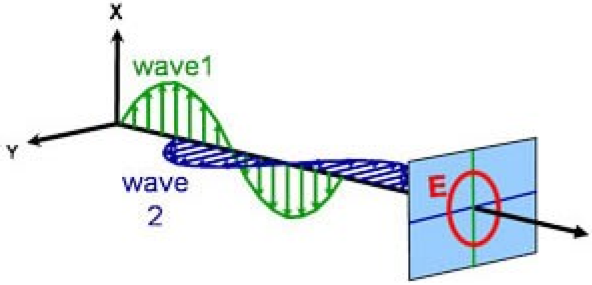

Figure 13: Circularly polarized light [43]

When two light waves are traveling in the same direction the resultant effect will be of a beam of light described by the vector sum of electric field vectors of the two individual waves. As an example, consider two perpendicularly polarized waves of equal frequency and amplitude. If the phase offset ξ is zero the resultant wave will remain linearly polarized, but the direction of polarization will be at an angle of 45 to the original waves (Figure 11). If ξ is set to 90°, the resultant electric field will no longer oscillate in a plane, but will trace a helix along the propagation direction. When viewed along the axis, a trace of the electric field vector would define a circle and this case is therefore known as circularly polarized light (Figure 13). Depending on the phase difference between the beams, the vector viewed along the axis will either move in a clockwise or counterclockwise direction giving rise to right- and left-circularly polarized light [47]

In general, the mixing of two waves of equal frequency results in the electric field vector tracing an ellipse when viewed down the axis of propagation (Figure 12). The linear and circular polarizations being a special case of elliptical polarization. Light of desired polarization can be selected from unpolarized light using combinations of optical elements which either block beams of certain polarizations or induce a phase shift in the beam.

The proportion of light transmitted and reflected from an interface depends not only on the media involved but also on the angle of incidence and the polarization of the beam of interest. One can separate the components of the electric field vector of the incoming light into two components. The first is within the plane of incidence defined by the propagation vector of both the incident and reflected wave, the so-called p-wave and the second is perpendicular to it, the s-wave, as shown in Figure 14. The ratios of the amplitudes of the incident and reflected waves are given by the Fresnel equations, which can be found in many optics texts [45:495-496]:

$$\begin{aligned} r_p &= \frac{\tilde{N}_2 \cos(\phi_1) - \tilde{N}_1 \cos(\phi_2)}{\tilde{N}_2 \cos(\phi_1) + \tilde{N}_1 \cos(\phi_2)} \\ r_s &= \frac{\tilde{N}_1 \cos(\phi_1) - \tilde{N}_2 \cos(\phi_2)}{\tilde{N}_1 \cos(\phi_1) + \tilde{N}_2 \cos(\phi_2)} \end{aligned} \tag{45}$$

When light is incident upon an ideal dielectric (k = 0), the Fresnel reflection coefficient for the p-wave becomes negative as the angle of incidence increases. The angle at which the reflection coefficient is zero is known as the Brewster angle. Since the intensity for the p-polarized light is proportional to the square of the amplitude, the p-polarized light will be fully transmitted at this angle. Further, since above this angle the reflection coefficient is negative, the p-polarized wave will have a phase shift of 180°. The Brewster angle can be calculated by:

$$\tan \phi_b = \frac{n_1}{n_2} \tag{46}$$

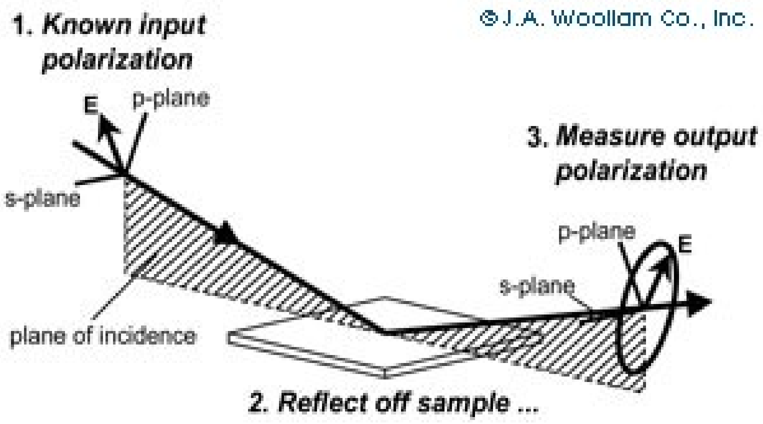

Figure 14:Linearly polarized light (1) is reflected off of the sample surface (2) and the change in polarization is measured (3) [47].

In the case of thin films the sample contains more than one interface. Light transmitted through the first interface will propagate through the film until it encounters a second interface. As in the above discussion, a fraction of this light will reflect from the interface while the rest is effectively lost into the substrate. The reflected light will travel back to the first interface where it will again split into a reflected component and a transmitted component. The transmitted component will exit the film structure and mix with the original reflected beam while the reflected component will again encounter the film-substrate interface. Each time the partial beam encounters the interface, its contribution to the total exiting beam becomes smaller and the situation can be treated as an infinite summation [48]. For a single film, the effective reflection coefficient for the two polarizations will be (where the subscript 1 represents the ambient medium, air; 2 represents the film and 3 represents the substrate) :

$$R^p = \frac{r_{12}^p + r_{23}^p \exp(-j2\beta)}{1 + r_{12}^p r_{23}^p \exp(-j2\beta)}; \; R^s = \frac{r_{12}^s + r_{23}^s \exp(-j2\beta)}{1 + r_{12}^s r_{23}^s \exp(-j2\beta)}; \\ where\, \beta = 2\pi \left(\frac{d}{\lambda}\right) \tilde{N}_2 \cos\phi_2 \tag{47}$$

The reflectance for each polarization can then be calculated as the square of the absolute value of each of the reflection coefficients. When multiple films are encountered, the reflectance can be calculated in an iterative manner.

The two polarizations are not necessarily in phase since a reflection can lead to a different phase shift in the p and s polarized rays. If we consider the phase difference between the s and p polarized beams in the incoming beam δ_1 and the phase shift after reflection from the structure δ_2 a parameter Δ describing the overall phase shift caused by the reflection from the structure can be defined as:

$$\Delta = \delta_1 - \delta_2 \tag{48}$$

Further, the reflection will not reduce the amplitude of each polarization by the same amount. Ψ is defined as the angle whose tangent is the ratio of the magnitudes of the total reflection coefficients:

$$\tan\Psi = \frac{|R^p|}{|R^s|} \tag{49}$$

The complex counterpart of Ψ is defined by the complex ratio of the total reflection coefficients, giving the most important equation for ellipsometric analysis:

$$\rho = \tan\Psi\, e^{i\Delta} = \frac{R^p}{R^s} \tag{50}$$

The quantities measured by an ellipsometer are limited to Ψ and Δ . These are then compared to the calculated Δ and Ψ of the model of the film in order to extract meaningful parameters such as the thickness, refractive index and extinction coefficient of the sample.

Section 4.1.2: Physical Models of the Optical Parameters

The optical parameters of a material are the result of the complex structure of the material itself. A simplified view of the material, although one that provides a good understanding of the interactions, is that of the Lorentz oscillator.

The electric field strength of an electromagnetic wave in a material is modified from its free-space value by the interaction with the atoms and molecules in its surroundings. When an external electric field is applied the centre of negative charge in an atom will respond by moving away from the centre of positive charge, which due to the high nucleus mass will remain effectively stationary. The effect of this motion is the formation of a dipole. If it is assumed that the displacement is small enough to be linear with the applied field, the macroscopic polarization of the material can be defined as follows:

$$\vec{P} = N \tilde{\alpha} \vec{E} \tag{51}$$

where N is the density of the oscillators and $\tilde{\alpha}$ is the wavelength dependent atomic polarizability. The local electric field at the location of the oscillator (atom) is given by the displacement field:

$$\vec{D} = \vec{E} + 4\pi N \tilde{\alpha} \vec{E} = \tilde{\varepsilon} \vec{E} \tag{52}$$

where the dielectric function $\tilde{\varepsilon} = \tilde{N}^2$. The dielectric function can be separated into the real and imaginary parts as:

$$\tilde{\varepsilon} = \varepsilon_1 + j \varepsilon_2 \tag{53}$$

where ε_2 represents the power absorbed per unit volume.

If one considers the atom to behave as a damped-driven harmonic oscillator, with natural oscillation frequency ω_0, a driving force provided by the applied oscillating electric field and a viscous damping factor Γ to account for the energy loss due to various scattering mechanisms, the dielectric function components become [48]:

$$\begin{aligned} \varepsilon_1 &= 1 + \frac{4\pi N e^2}{m} \frac{(\omega_0^2 - \omega^2)}{(\omega_0^2 - \omega^2) + \Gamma^2 \omega^2} \\ \varepsilon_2 &= \frac{4\pi N e^2}{m} \frac{\Gamma \omega}{(\omega_0^2 - \omega^2) + \Gamma^2 \omega^2} \end{aligned} \tag{54}$$

Except for a small region around ω_0, ε_1 increases with frequency. The region where ε_1 decreases is known as an anomalous dispersion region. It can also be seen that ε_2 increases to a peak around ω_0 and approaches zero as ω moves away from ω_0, indicating that there is little absorption at frequencies far from the resonant frequency of the oscillators.

From the relation of the complex refractive index and the dielectric function, n and k can be found as:

$$n=\sqrt{\frac{1}{2}[(\varepsilon_1^2+\varepsilon_2^2)^{\frac{1}{2}}+\varepsilon_1]}$$
$$k=\sqrt{\frac{1}{2}[(\varepsilon_1^2+\varepsilon_2^2)^{\frac{1}{2}}-\varepsilon_1]} \tag{55}$$

In the case where more than one oscillator is required for a material, these equations can be summed over the appropriate densities and resonant frequencies.

Since the resonant frequency of the material is related to the bandgap of the material ($E_g=\hbar\omega_0$) the resonant frequency for most insulators, with a large bandgap, will fall into the far UV range. In the visible range the refractive index will fall off slightly with increasing wavelength and the extinction coefficient will be very small. Under these conditions the index of refraction can be modeled using the Cauchy function:

$$n(\lambda)=A+\frac{B}{\lambda^2}+\frac{C}{\lambda^4} \tag{56}$$

where A, B and C are the Cauchy parameters of the material.

For most semiconductors the smaller bandgap will place the resonant frequency in or near the visible range and the Cauchy model can still be used to model the index of refraction. The extinction coefficients are sometimes modeled with an equation of the same form as the Cauchy equation or may be set as a constant over the range of interest. Models of real semiconductors usually require the use of more than one oscillator.

It is important to note that in materials such as PECVD grown silicon oxynitride films factors such as hydrogen content and film porosity will modify the optical parameters of the material. Thus a film of the same composition deposited using different systems or even in the same system under different conditions will yield different values of the optical constants.

Furthermore, no film deposited by PECVD will have a perfect plane interface between the substrate and the film nor a perfect surface. In this case the rough area can be modeled using an Effective Medium Approximation (EMA). A simple and most commonly applied EMA is a model treating the roughness layer as a mixture of the two materials whose dielectric function is related to the dielectric functions of both materials and the volume fraction, f, that each material is thought to occupy in the layer. In the Bruggeman approximation the dielectric function can be found by solving the Bruggeman equation:

$$\varepsilon_{eff}=f_a\frac{\tilde{\varepsilon}_A-\tilde{\varepsilon}}{\tilde{\varepsilon}_A+2\tilde{\varepsilon}}+f_b\frac{\tilde{\varepsilon}_B-\tilde{\varepsilon}}{\tilde{\varepsilon}_B+2\tilde{\varepsilon}} \qquad (57)$$

where the subscripts A and B refer to the two materials at the interface.

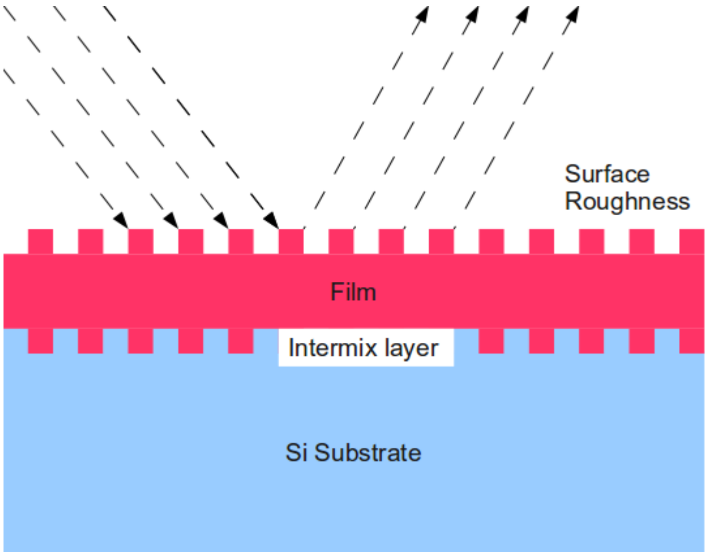

Figure 15: Model layers of a film include a 50% void layer to simulate surface roughness and a 50% substrate/film layer to simulate intermixing at the beginning of growth.

The models used to calculate the film thicknesses and optical parameters contain two "mixing" layers to account for the non-abrupt interfaces. The top layer is considered a 50% mixture of the film dielectric and air and simulates the roughness of the surface. This is followed by the bulk film region, which is modeled on top of a 50% film, 50% substrate layer which simulates the substrate roughness or intermixing layer, see Figure 15.

Section 4.1.3: Single Wavelength Considerations

While a single wavelength measurement of a Ψ and Δ of a substrate can yield a unique solution for physically meaningful n and k measurements, the measurement of a film is not as straight forward. When a film is deposited on the substrate a trajectory will form on the Ψ, Δ plane with a parameter of film thickness. For transparent films the curve, or trajectory, will eventually close back onto itself after a given thickness. This thickness or period is given as:

$$d=\frac{\lambda}{2\sqrt{n_2^2-n_1^2\sin^2\phi_1}} \tag{58}$$

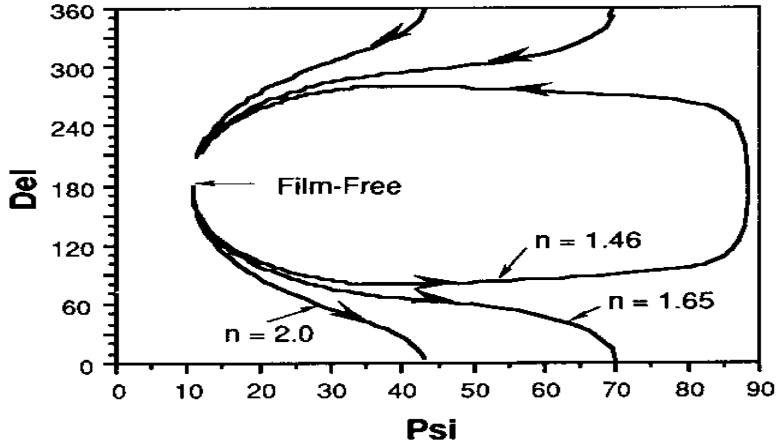

Figure 16: Ellipsometer trajectories for films of varying refractive index on silicon show change in Del and Psi with increasing thickness. The area in which the traces become dense, known as the period point, is an area of low sensitivity to the refractive index (and hence thickness) with respect to Psi [44].

In areas near the period point, shown in Figure 16 the determination of the index of refraction becomes quite difficult as a small error in the measurement of Ψ can cause a large error in the determination of the index of refraction and hence effective thickness. The insensitive areas near the period point should be avoided, if possible, by selection of a different film thickness if growth rates are well known.

In the measurements discussed in this work, single wavelength ellipsometry was used for some initial tests directly after the deposition, but the main application was in determining surface uniformity. By using the computerized XY stage on a Philips Z2000 ellipsometer setup in the CEDT laboratories, it is possible to take a series of rastered measurements to approximate the thickness of the film as a function of position on the wafer.

The growth uniformity for the samples was determined using a raster scan consisting of 100 points in a 30 mm square. The non-uniformity was calculated as the ratio of the range between the highest and lowest measurement to double the average measurement.

Samples exhibiting larger than usual non-uniformity were samples which exhibited non-circularly-symmetric thickness profiles (See Figure 38, discussion in Section 6.4). For these cases the method of calculating the non-uniformity is not as meaningful as it is for samples of low non-uniformity. For practical production systems, a more meaningful measure would be the fraction of the total area which falls within the bounds of an acceptable thickness deviation or the largest square which falls within these bounds.

Samples exhibiting this type of non-uniformity would be rejected from production runs and are not as indicative of the general trends in a set as samples exhibiting low non-uniformity, circularly symmetric growths. Given a longer time frame, these samples would be redeposited in order to give a more reliable data set. They have, however, been included in the following studies for completeness.

Section 4.1.4: Variable Angle Spectroscopic Ellipsometry

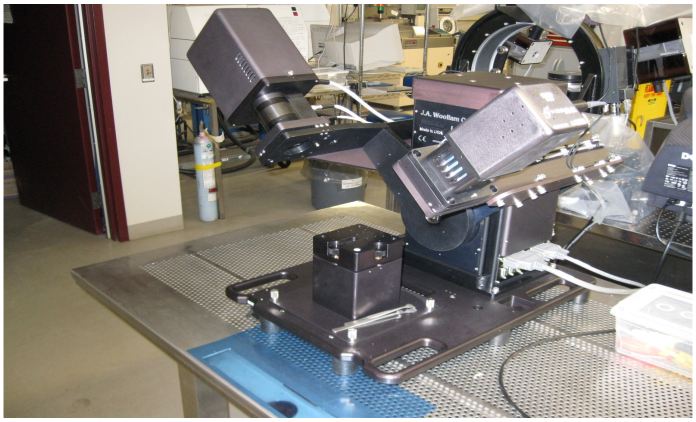

Figure 17: J. A. Woollam M2000V ellipsometer used to take VASE measurements.

In order to overcome the limitations of single wavelength ellipsometry, including issues with periodicity, regions of extremely low sensitivity and values of λ and k being limited to a single wavelength, variable angle spectroscopic ellipsometry (VASE) is a desirable technique. By taking spectral measurements at multiple angles of incidence the technique allows for the analysis of complex material systems [49].

Using a range of incident wavelengths and taking measurements at multiple angles of incidence both allows the determination of optical properties over a range of wavelengths and removes the periodicity issues associated with single wavelength, single angle measurements. Furthermore, the large data set gathered in such a measurement gives sufficient information to model multilayer films with high accuracy.

VASE measurements in our studies were taken with a J.A. Woollam M2000V ellipsometer (Figure 17), with measurements taken at incident angles of 55°,

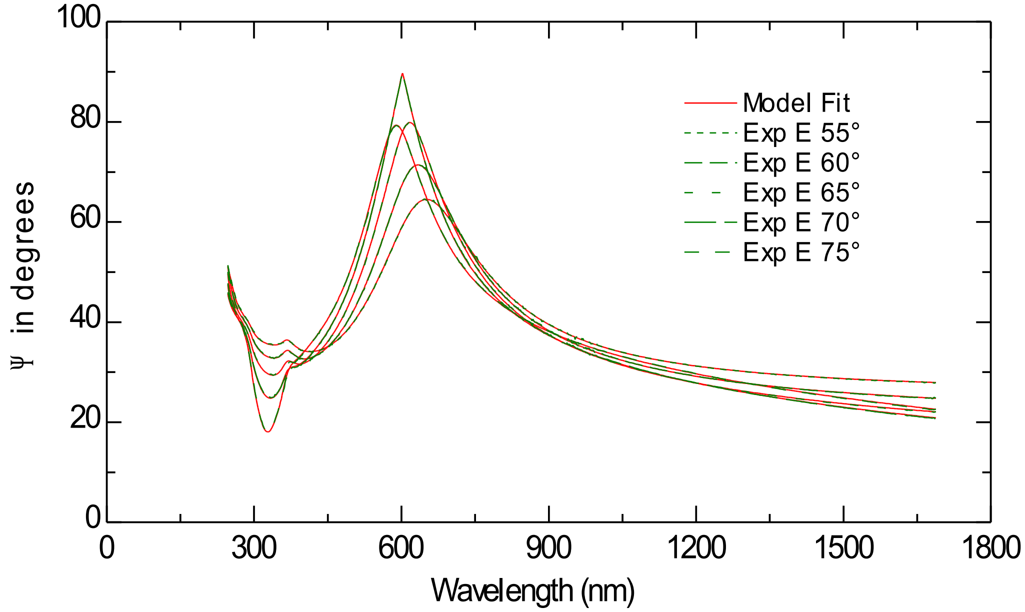

Figure 18: Psi spectrum and model fit for sample WNP5-158, SiO_xN_y film

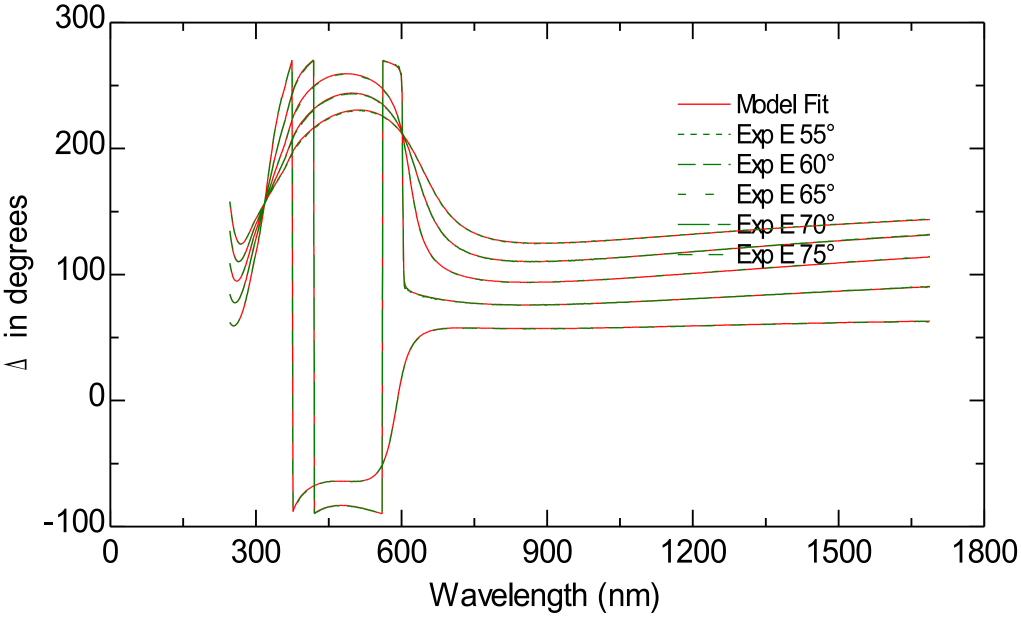

Figure 19:Delta spectrum and model fit for sample WNP5-158, SiO_xN_y film

60°, 65°, 70° and 75° measured from the surface normal. To simplify modeling, the UV portion of some spectra was removed. Sample VASE spectra are shown in Figures 18 and 19. From this data a model (see Figure 15) is built containing four layers: a surface roughness layer, generally thinner than 20 Å; a modified Cauchy model of the film itself, whose thickness, refractive index and absorption coefficient are the defining measurements; an intermixing layer, also generally below 20-30 Å and the silicon substrate whose properties are well defined. The dispersion relations for the refractive index n and extinction coefficient k for this film are shown in Figure 20.

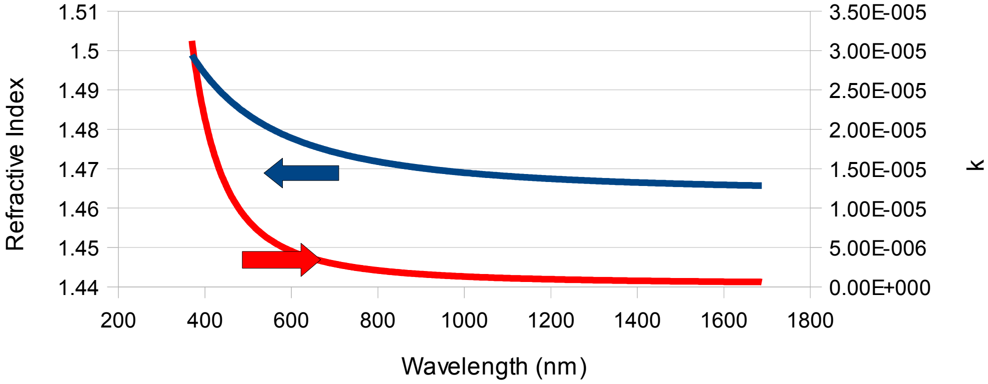

Figure 20: Dispersion relations are shown for the refractive index and extinction coefficient. The low extinction coefficient makes the modified Cauchy approximation valid.

The goodness of fit is calculated using a mean square error (MSE) estimator [50].

$$MSE=\sqrt{\frac{1}{2N-M}\sum_{i=1}^{N}\left[\left(\frac{\Psi_i^{mod}-\Psi_i^{\exp}}{\sigma_{\psi,i}^{\exp}}\right)^2+\left(\frac{\Delta_i^{mod}-\Delta_i^{\exp}}{\sigma_{\Delta,i}^{\exp}}\right)^2\right]}=\sqrt{\frac{1}{2N-M}\chi^2} \qquad (59)$$

where M is the number of parameter variables in the model.

The modified Cauchy model used gave excellent fits to the data as indicated by the MSE which was generally below 10 and below 2 for the majority of the samples.

Section 4.2: Photoluminescence Spectroscopy

Photoluminescence spectroscopy (PL) is a characterization technique in which one measures the optical spectrum from the recombination of electron-hole pairs initially created by the optical excitation of electrons in a material. The technique is of great practical value since it can yield information about the optical transitions occurring in the material without the need to directly inject carriers electrically, which can pose a practical problem for many materials.

The initial excitation requires an intense light source whose photon energy is higher than the bandgap of the material being studied. Photons from the source are absorbed by valence electrons in the material which then are promoted to the conduction band. Since the electron in the conduction band is not in a stable state, it will necessarily recombine with a hole. Radiative recombination can either involve a direct recombination between the valence band hole and the conduction band electron, which will result in the release of a photon of the same energy as the bandgap; or through interband defect states, resulting in the release of photons whose energy is lower than the bandgap energy in the material. The intensity of the excitation light results in a large number of these recombinations occurring simultaneously (to reduce the influence of detector noise) and so the measurement is one of the bulk film rather than of single discrete transitions.

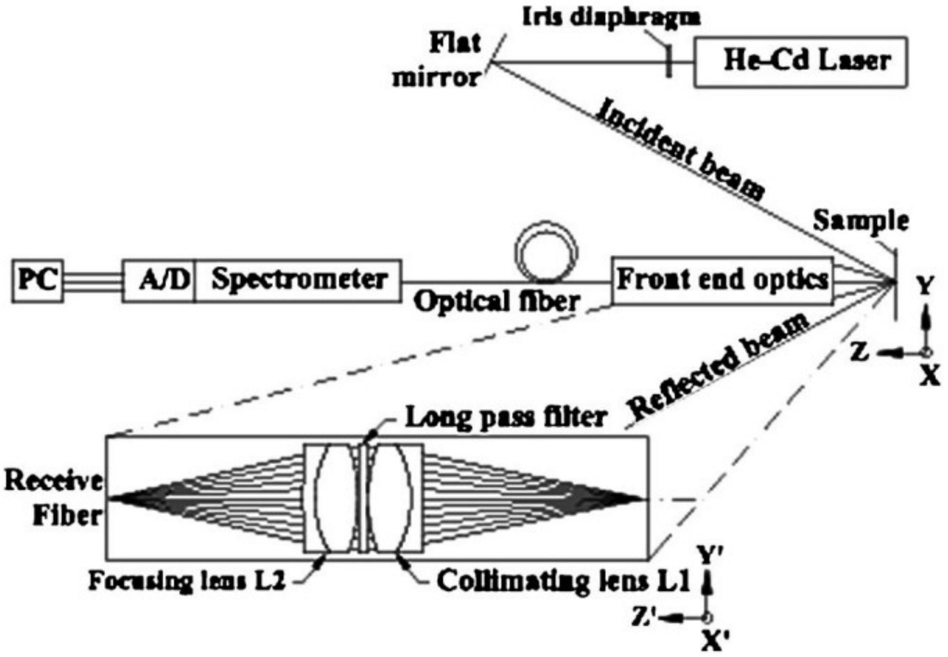

Figure 21: Schematic diagram of the photoluminescence spectroscopy setup used for Ce doped film measurements [51].

Details of the experimental apparatus used can be found in [51]. The excitation is provided by a 325 nm He-Cd laser. The sample itself is set on a XYZ stage. Before the spectrum is collected the sample position is adjusted to avoid any "dark" areas yielding low luminescence. The spectrum is collected via an Ocean Optics S2000 miniature fibre optic spectrometer [52].

Although the spectrum is collected in the dark, with possible light sources (such as computer monitors) shielded, a background "dark spectrum" is taken before the measurement and subsequently removed from the measured spectrum. The measurement time is 5 seconds per spectrum. After the spectrum is collected, a calibrated correction coefficient is applied at each wavelength to account for the spectral response of the detector.

Section 4.3: Rutherford Backscattering Spectrometry

Rutherford backscattering spectrometry (RBS) is a common near surface analytic technique used in materials science. The technique requires an ion beam (typically He^{2+} ions) to be directed onto the sample. Assuming there is no nuclear reaction that occurs, the ions will the undergo elastic collisions with the stationary target nuclei. If only a thin foil is used as a sample, and a detector is placed at a certain angle, θ_s , between the foil and the ion beam, it will detect particles whose kinetic energy will be reduced from the incident energy by a factor [53]:

$$k=\left(\frac{Z_1\cos\theta_s+\sqrt{Z_2^2-Z_1^2(\sin\theta_s)^2}}{Z_1+Z_2}\right)^2 \tag{60}$$

where $Z_1<Z_2$ represents the masses of the incident and target ions, respectively. If the incident ion beam is monoenergetic and well collimated, the measurement of the energy of the scattered ions at the scattering angle θ_s can then be used to calculate the mass of the target nuclei thus identifying them.

For thicker samples, small angle scattering from the target electrons will effectively reduce the energy of the incident ions with penetration depth. This energy loss, known as the stopping power is a function of the density and structure of the material and is often measured experimentally for different materials. The result of this is that for a near monolayer thin film the detection yield vs energy spectrum from a single element would appear as a spike at a given energy. A thicker sample would produce an almost flat response for a small range of energies just below the elemental signature energy. For even thicker samples, the distribution would drop off with thickness caused by a loss of ion density and a lower probability that a large angle scattering event would lead to a measurable ejection of the ion from the surface. If a second element is only present below a certain depth in the sample the peak will be shifted to a lower energy than if the element were present at the surface.

When using RBS to analyze crystalline samples or samples with any long range symmetry care must be taken to avoid channelling, which reduces the observed backscattering of ions to well below expected levels. Channelling occurs when a major crystallographic axis is well aligned with the primary beam direction. In this case, if an ion does not scatter from a surface atom it is more likely to undergo low angle scattering in deeper layers of the crystal than a nuclear backscattering event. This effectively "traps" the ion between crystal planes parallel with the beam and while the ions will probe deeper into the surface, the effective density observed will be much lower than the real atomic density of the sample. In thin film amorphous systems grown on crystalline substrates such as silicon, care must be taken to set the incident angle to avoid substrate channelling or unphysical measurements of the substrate signal will be observed.

By using both the discrete edges caused by the presence of a given element and the energy shifting caused by the low angle electron scattering within the sample, a depth profile of a sample can be mapped. While it is fairly easy to calculate general feature positions and relative heights from first principles using an assumed sample composition, it is far more common to use simulation software which gives a more detailed spectrum. By comparing the software generated spectrum of the simulated structure against the measured spectrum of the sample, adjustments to the simulated structure can be made in an iterative process until a close match is achieved.

Although many different software packages exist for modelling the ion beam interactions and RBS spectra, the software used for the RBS analysis in this work is the SIMNRA software written by Matej Mayer [54]. SIMNRA was chosen for its implementation of plural (accounting for multiple large angle scattering events) and multiple (accounting for multiple small angle scattering events) scattering as well as geometrical scattering, and adaptability of input format. The main detraction from using this particular software is the limited number of fitting options for multi-layer structures which requires quite a lot of manual fitting time for reasonable fit conversion and reliable results. Unless otherwise noted the incident angle is 5° to avoid substrate channelling. The stopping power data for all of the simulations used is the data of Ziegler [55]. Bragg's assumption that the interaction between the ion and target atom is independent of the environment is used to calculate the stopping power and thus the effects of the bonds on the stopping power are ignored. The stopping power S for a compound with concentration c_i of element i (so that $\sum c_i = 1$) is thus [56]:

$$S = \sum c_i S_i \tag{61}$$

Since, particularly in oxides and nitrides of light elements, the effect of bonds on the stopping power can be on the order of up to a few percent, the resultant thickness calculated by the program may in fact be an overestimate [57].

Modelling of variations in the composition of the film with depth was done by dividing the simulation material into layers with stepwise compositional changes to approximate the expected gradient change in the film composition. These concentration changes were particularly visible for the Ce doping. The compositions were changed first by hand and then using fitting routines to attain the closest match to the experimental data. More detail on the fitting methods is given in Chapter 6.

Chapter 5: McMaster ECR-PECVD Reactor

Section 5.1: Introduction

This chapter will give an overview of the hybrid sublimation electron cyclotron resonance plasma enhanced chemical vapour deposition (ECR-PECVD) system installed and tested at McMaster University's CEDT laboratories.

The major subsystems, including the plasma generation system, gas delivery system, vacuum and pressure measurement systems, sample transfer mechanism, residual gas analysis, dispersion ring geometry, metalorganic dopant delivery system, substrate temperature control and interlock system will be reviewed in detail. Aspects of system maintenance will also be discussed.

The system was manufactured by Johnsen Ultravac of Burlington, Ontario under the supervision of Dr. Jacek Wojcik and the author. The system was then taken apart and transported to the laboratory where accommodations for the system had been prepared. The final assembly of the system took place in the laboratory and initial subsystem testing, described further in this chapter, was undertaken. The connections for the vacuum system were made and the plumbing for the gas lines and exhaust were installed. The gas line heating system, plasma chamber cooling system and sample stage heater connections were installed and tested. Alignment of the sample stage was adjusted so that the transfer between the load lock arm and deposition chamber arm was smooth. The computerized control system interlocks were tested and sample depositions were started. Details of the subsystems and points of interest in the design of the system are summarized in the following sections.

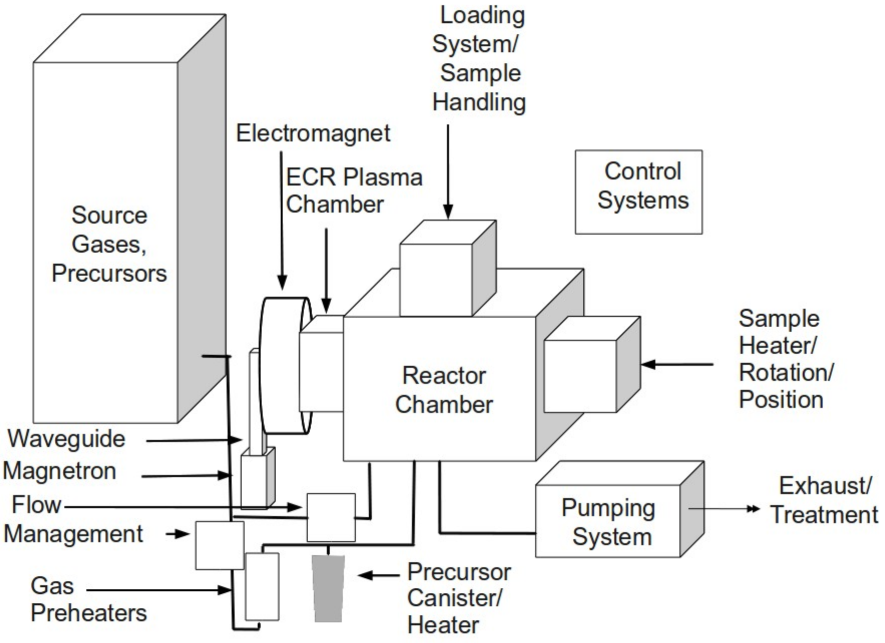

Figure 22: Simplified schematic drawing showing the interconnection of major subsystems in the ECR-PECVD reactor.

Section 5.2: Subcomponents/Subsystems

Section 5.2.1: ECR Magnet

To provide the 875 G magnetic field necessary for the electron cyclotron resonance condition a helical electromagnet is used. The inside diameter of the magnet is 8” and the total winding resistance is on the order of 0.1 Ω. The 875 G resonance condition is met at a magnet current of 180 A. The magnet is cooled using a water loop which runs from the chilled water pipes through the magnet and then through the microwave dummy load into the chilled water return. The plasma chamber onto which the magnet is mounted is capped with a quartz window to allow the penetration of the microwave energy into the chamber. The flange containing the window has perforations evenly distributed along the interior circumference which forms the dispersion ring for some of the process gases lines. Generally, only the oxygen and nitrogen source gases as well as argon are let in through this dispersion ring since adding silane in this region would result in unwanted deposition on the surrounding chamber walls and the dielectric window.

Magnet alignment is of crucial importance to efficient plasma generation and proper ion diffusion into the chamber. Since the electrons tend to diffuse along the magnetic field lines and are driven by the gradient of the field, the single magnet ECR configuration requires that the magnetic field diverges into the chamber and not in the direction of the microwave coupling window. If the magnet is placed too deep into the plasma chamber, the electrons generated near the window will tend to drift in the direction of the window and the ions will follow, driven by the charge separation. This creates a local trap for back-diffusing ions and can cause a deposition on the window itself. Of greater importance, since the gas inlet is located at the inner window plane, the plasma density inside the main chamber will be reduced. This has been visually confirmed by adjusting the magnet position during plasma generation.

The original plasma chamber was a 13” long, 8” diameter cylindrical chamber designed to allow the magnet to be continuously moved along exterior rails. While a similar chamber used with a two magnet configuration creates a dense trap between the magnets, a single magnet configuration creates a wide divergence of the magnetic field which would cause the plasma to diffuse quickly towards the walls of the plasma chamber. Combined with the larger magnet-substrate distance the ion flux on the substrate is quite low. Test depositions conducted with the 13” chamber did not yield any detectable films formation.

When the chamber was replaced by a much smaller chamber, 4” in length, successful film growth was possible. The large divergence of the magnetic field still led to a significant impact of the plasma onto the chamber walls and caused the chamber itself to be hot to the touch during runs. To avoid overheating and potential sidewall sputtering the plasma chamber required cooling, which will be described in the Plasma Chamber Heating section later in this chapter.

Section 5.2.2: Power Supply

Since stability of the high current supply is necessary for the operation of the system a specialized regulated power supply (EMS 20-125-2D) is used. The supply ensures that voltage ripple is less than 30 mV near 180 A operation [58]. The supply itself is fed from a 240 V main. Since the magnet coil resistance changes slightly with temperature it is imperative that the magnet current be turned on well before the plasma is struck to ensure that the current has stabilized.

Section 5.2.3: Microwave Source Network

The system utilizes an Astex HS-1000 magnetron head as a microwave source. The magnetron is coupled into a waveguide with a water cooled dummy load used to absorb the microwave radiation reflected from the plasma. The air cooled S-1000 microwave power supply mounted in the equipment rack supplies the magnetron with a feedback regulated maximum output power of 1000 W at the commercial band frequency of 2.455 GHz ± 15 MHz with a stability of 0.5% and ripple of less than 1%. The output microwave power can be set to a level between 200 W and 1000 W. The power supply has both automatic power limiting and magnetron filament power monitoring (held to approximately 100 W) to reduce the potential for operator error induced damage to the magnetron head [59].

A reflected power detector is mounted downstream, after the directional coupler (Astex CS-1000 Circulator) of the waveguide, to allow the monitoring of reflected power with the use of a diode detector and feedback to the power supply is given through a BNC connector. The circulator deflects the reflected power into the dummy load, protecting the magnetron head from the reflected energy and it allows the assembly to safely drive any load.

Load matching between the microwave generator and the plasma load is obtained by a series of three tuning stubs mounted within the waveguide and between the directional coupler and dielectric window separating the waveguide from the plasma chamber. Adjusting the position of the three plungers mounted on the waveguide allows the microwave source to effectively couple into changing plasma gas pressures and compositions while feedback for both the forward and reflected power are shown on the front panel. The microwaves are fed through a model SPCF rectangular to circular symmetry transducer to convert the TE_{10} mode of the waveguide to the TM_{01} mode applied to the round quartz window barrier [60].

The process of tuning the microwave coupling is non-trivial since ECR plasmas can exist in multiple steady states and often exhibit abrupt transitions and significant hysteresis [61]. Care must be taken to not only minimize reflected power but also to ensure that the system is operated in a stable mode during deposition. Constant monitoring of reflected power is critical.

Section 5.2.4: Pressure Measurements

Due to the wide range of pressures that the system encountered – ranging from atmospheric pressure (~760 Torr) during maintenance and reaching as low as 1.1×10^{-9} Torr base pressures – a number of different pressure measurement methods are required.

Low vacuum measurements are made using a Varian 0531 thermocouple gauge. This gauge consists of a wire heater element with thermocouple both housed in a tube. At higher pressures, a large number of gas molecules strike the wire and carry heat away, while at lower pressures the decreased number of molecules available to remove the heat causes an increase in the steady state heater temperature and hence the thermocouple output. When the pressure becomes low enough that radiation takes over as the dominant heat loss mechanism, the sensitivity of a thermocouple gauge becomes too low for the gauge to give useful pressure information [62]. Convection gauges are used in conjunction with the thermocouple gauges to measure high pressures.

High vacuum encountered while the system is at rest is ascertained using a hot cathode ion gauge. Thermionic emission creates free electrons from a heated filament and these are then contained by a wire grid with a high potential applied. Any ions created in the process are attracted to a third electrode. This ionization current is effectively a measure of the gas density since the probability of an electron forming an ion increases with pressure. These gauges are not only limited to low pressure (since a high current can cause the filament to burn out) but are also quite sensitive to the gas being measured since the ionization cross-section varies with different gases.

Pressures during deposition are measured using a Baratron capacitive manometer gauge. These gauges are insensitive to gas composition and give reliable absolute pressure measurements. In the gauge, a diaphragm is placed between a sealed chamber containing a high vacuum ($\sim 10^{-7}$ Torr) and the pressure to be measured. The deflection of the membrane is measured by the change in the capacitance between two electrodes surrounding the diaphragm. Although quite sensitive to particulation, the capacitive manometers offer excellent repeatability, quick response and higher accuracy than thermal gauges in a clean vacuum environment [62].

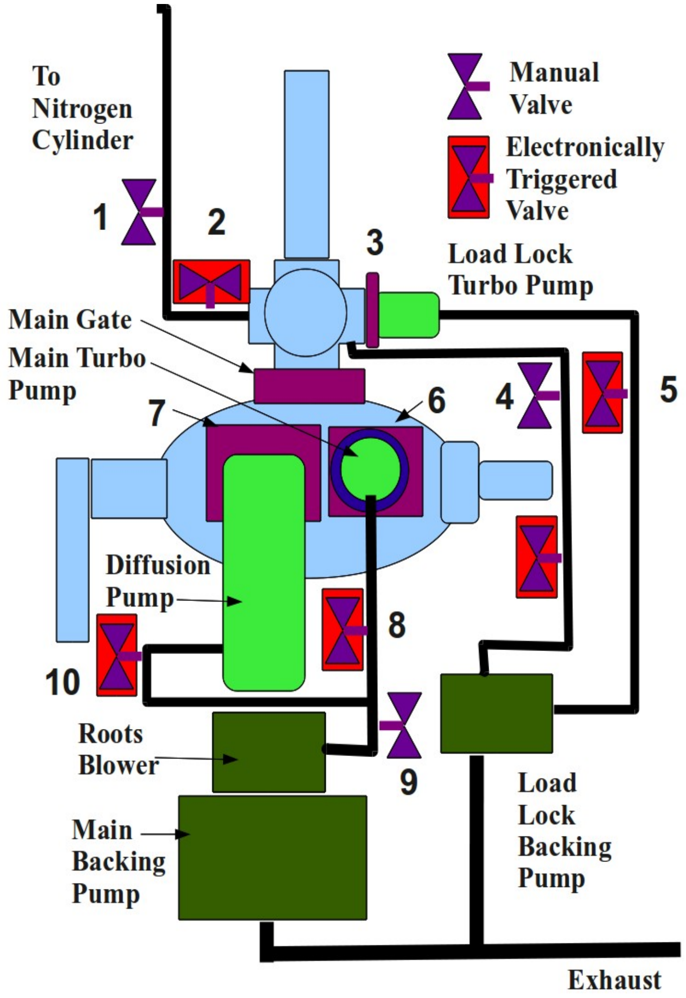

Figure 23: Simpified schematic overview of vacuum system with valving

Section 5.2.5: Vacuum System

The vacuum system for the reactor was designed to be a nearly dry system to eliminate contamination from pump oils. For this reason the main chamber and load lock are evacuated using turbo pumps (See Figure 23).

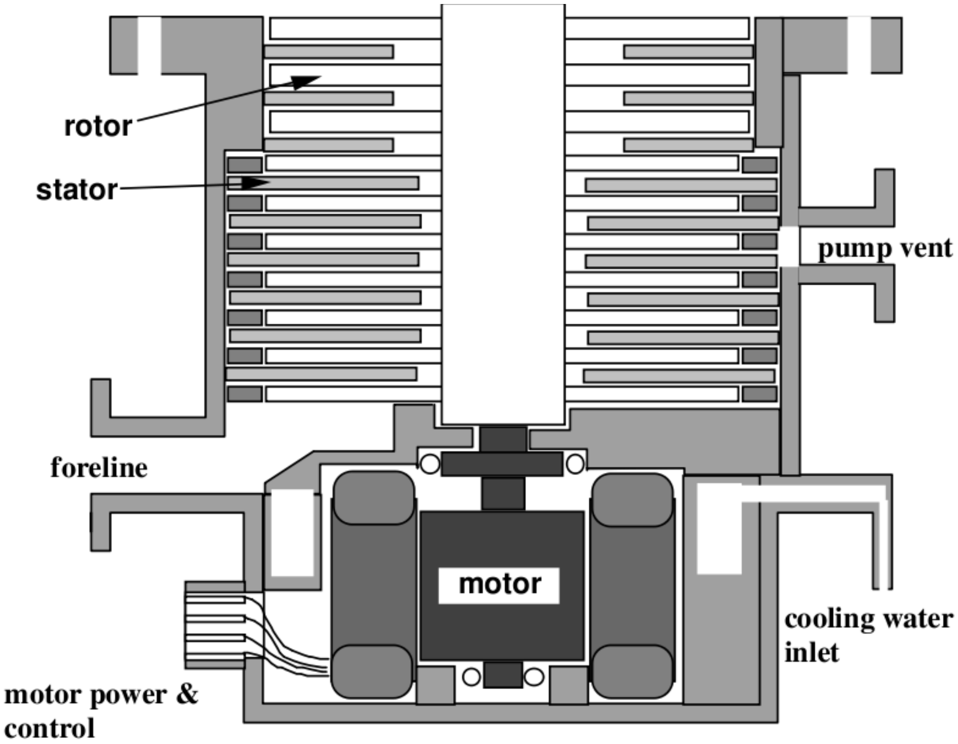

Figure 24: Schematic of an axial flow turbomolecular pump highlighting typical arrangement of stators and rotors. Adapted from [64].

5.2.5.1 Pumps

The main chamber is evacuated using a Pfeiffer TMH 520 turbomolecular drag pump, with a throughput of 300 L/min. The original design, which included a pump of higher volumetric flow, required a throttling valve to maintain a pressure high enough for reasonable deposition rates. In the final arrangement the smaller pump was fitted and it was found that no throttling would be necessary and the deposition pressure could be controlled by the gas flows alone. The pump is compatible with the dry vacuum requirements [63]. The typical base pressure is maintained below ~0.5×10^{-7} Torr between consecutive depositions and ~$0.5x10^{-8}$ Torr otherwise.

The axial flow turbomolecular pump, as shown in figure 24, consists of a series of matched rotors and stators mounted along a single axis. The rotors and stators are designed to work in stages with each pair producing a slightly higher pressure much like in the operation of a compressor. In effect the molecules “stick” to the rotors for a characteristic residence time during which the momentum of the rotors (spinning at ~50,000 rpm) is imparted onto the gas molecules.

The stator then acts like a baffle, which directs the quickly moving particles onto the next stage. The extreme rotational rate of the rotors requires exquisitely precise machining and balancing. The inlet stages are designed with an aspect ratio to maximize volumetric flow and increase the total flow to the exhaust stages which are designed to maximize compression. This allows efficient evacuation of the exhaust by the backing pump system. Typical foreline pressures for turbomolecular pumps are 1 Torr or below, since above these pressures the collisions between gas molecules and the rotors add drag to the rotor which could overload the motor and cause the rotational speed to drop to the point where the pumping speed becomes ineffective.

The removal of the built up gases in the foreline of the turbo pump is carried out by a backing pump stack composed of a Leybold D40 BCS PFPE (perfluoropolyether) Two-Stage Rotary Vane Pump and a RuVac WS 251 PFPE Roots blower pump. The roots pump is used to increase the compression of the turbo pump exhaust so it can be

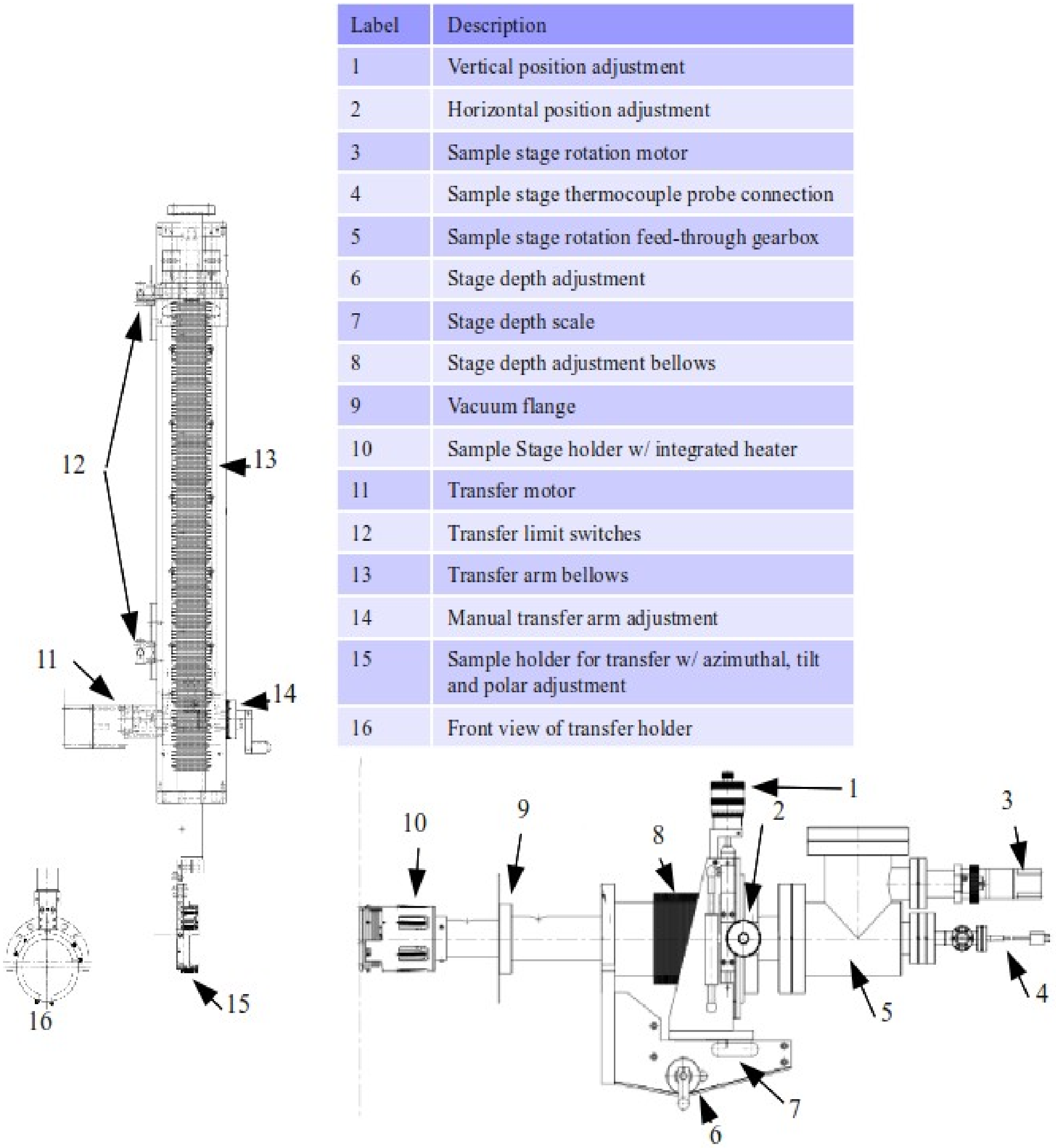

Label	Description
1	Vertical position adjustment
2	Horizontal position adjustment
3	Sample stage rotation motor
4	Sample stage thermocouple probe connection
5	Sample stage rotation feed-through gearbox
6	Stage depth adjustment
7	Stage depth scale
8	Stage depth adjustment bellows
9	Vacuum flange
10	Sample Stage holder w/ integrated heater
11	Transfer motor
12	Transfer limit switches
13	Transfer arm bellows
14	Manual transfer arm adjustment
15	Sample holder for transfer w/ azimuthal, tilt and polar adjustment
16	Front view of transfer holder

Figure 25: Main components of sample transfer mechanism. Transfer arm to stage spacing not to scale. Adapted from [65].

efficiently exhausted by the rotary vane pump. Since the absence of oil for sealing, lubrication and cooling of the pump would lead to short pump life and high cost of oil-free designs, the backing system is not a dry system. The back migration of oil vapour through the turbomolecular pump is, however, negligible and the system as a whole can be considered an effectively dry one.

5.2.5.2 Diffusion Pump

The system is fitted with diffusion pump as a back-up system in case of a failure of the turbo pump and if lower base pressures than those attainable by the turbo pump were required. Since the turbo pump is both easier to operate and free of problems related to the back migration of oil vapour, the diffusion pump was not used for any of the depositions discussed and the gate valve connection was kept closed to maintain dry vacuum.

Section 5.2.6: Load Lock

To facilitate the transfer of the sample and reduce the contamination of the main chamber by atmospheric moisture, a load lock transfer system is used to load and remove samples from the system. The load lock chamber is mounted above the main chamber and is separated by a gate valve. During loading and unloading, the load lock is vented with dry nitrogen to displace most of the moisture laden air that could enter the load lock. Since residual atmospheric moisture is a major issue for ultra-high vacuum systems, all moisture must be pumped out and allowed to outgas from the chamber walls before the transfer is initiated.

After the sample has been loaded and the load lock pumped down to a pressure roughly equal to the main chamber pressure and at least below $5.0x10^{-6}$ Torr the main gate is opened and the transfer rod, shown in figure 25 can be lowered into the chamber. The motion of the transfer arm is facilitated with a linear manipulator which uses a threaded rod to move a flange containing the transfer rod sealed within a set of bellows.

At the lower limit position of the transfer rod the sample stage is aligned with the horizontal sample positioning arm. The arm is extended to align the rods of the sample stage with the grooves on the arm. A rotation then disengages the stage from the vertical transfer rod and engages the spring loaded holder on the sample positioning arm. The arm is then retracted, the rod removed and the load lock gate valve isolates the main chamber once again.

Section 5.2.7: Residual Gas Analyzer

Since system purity is paramount to growths of high quality films, a residual gas analyzer (RGA) was installed to monitor base pressure composition in the main chamber between growths. A quadrupole residual gas analyzer was used to measure the base pressures and ensure that any unwanted chamber impurities could be recognized before starting a deposition.

The measurement process begins with an ion source which traps thermionically produced electrons which oscillate through a mesh electrode. Interaction of these electrons with the chamber gases preferentially creates positive ions which are then accelerated and focused towards the mass filter using a high negative potential.

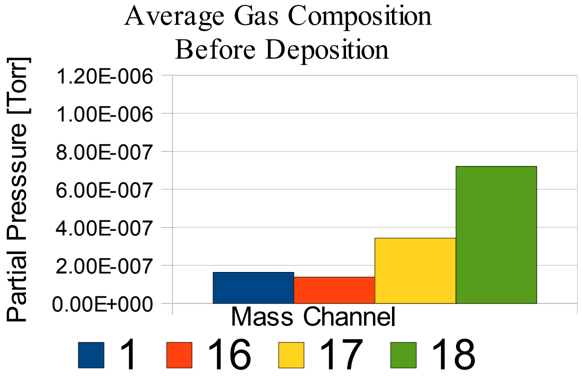

Figure 26: Average residual gas composition before deposition. Channels of mass 1 correspond to hydrogen, 16 to oxygen, 17 to OH^+ and 18 to H_2O.

At the heart of the quadrupole gas analyzer are four cylindrical rods arranged in a square. Rods opposite each other are electrically connected, creating a potential field whose equipotential lines approximate rectangular hyperbolae. An RF signal, typically in the low MHz range, riding on a DC offset is applied in opposite phase to the two sets rods. As ions travel along the axis of the rods they will begin to oscillate under the influence of the applied potential. Stable oscillations on either axis is dependent on the ion mass for a given applied potential and RF signal. The two axes reject ions which are too heavy and too light and act as a “bandpass” filter for the mass-charge ratio. By scanning the RF signal in a way that increments the mass of the ions that are let through and concurrently adjusting the DC offset to increase the selectivity of the filter for increasing mass, a sharp cut off is maintained. By dwelling at a particular filter setting for a given time and integrating the ion current for this time the partial pressures of the gas constituents can be measured [67].

The residual gas composition is typically found to consist largely of water vapour with the largest peak located at 18 amu corresponding to H_2O with fragment ion peaks of 17 and 16 amu corresponding to OH^+ and O^+. H^+ concentrations similar to O^+ concentrations were observed. The average pre-deposition partial pressures for the most common species, all related to water vapour are shown in figure 26.

Section 5.2.8: Gas Delivery System

Reproducible and stable gas flows are a necessity for the well-controlled growth of thin films. Gas flows are controlled by MKS type 1176 mass flow controllers (MFC). In total there are 10 channels for gas flow handled by two separate multi-gas controller interfaces. Two of the channels are not connected but are reserved for future use. The "top" controller, a MKS 647B, interfaces with the MFCs for the metalorganic evaporative precursor lines while the "bottom" controller interfaces with the undoped process gas lines.

The response of the mass flow controller changes with the gas that is passed through it. The MFCs are therefore calibrated for a known gas. While most of the gas flow controllers were calibrated for nitrogen, line 4 was calibrated for hydrogen. Flowing a different gas through the MFC requires that a gas correction factor (GCF) is used to account for the different proportions, thermal properties and standard densities of the gases. Since nitrogen is customarily used as the standard gas, the GCF is calculated relative to nitrogen and then converted to the GCF for the gas to be used. The gas correction factor for a mixture of gases is calculated as follows [68]:

$$GCF = \frac{0.3106\,(a_1 s_1 + a_2 s_2 \cdots a_n s_n)}{(a_1 c_{p1} d_1 + a_2 c_{p2} d_2 \cdots a_n c_{pn} d_n)} \tag{62}$$

where a_n represents the fractional flow of the different gases 1 through n, s_n represents the structural factor for the gases (dependent on the number of atoms in each gas molecule), c_p represents the specific heat capacity and d represents the standard density of the gas.

Using this formula the GCF for the different channels was calculated and these factors as well as a general description of the gas flow control system are given in Table 1.

To reduce the overall complexity of the laboratory and to conserve on valuable floor space, this system shares its gas supply cylinders with two adjacent systems. The gas supply lines exit the gas cabinets and are routed above the machines. Joints in the 1/4" type 304 stainless steel piping were welded using an automated orbital welder to ensure joint quality. The gas supply lines branch off from above to supply each of the systems.

Table 1: Summary of gas lines and mass flow controller settings

Line # (as read on computer)	Gas	Controller	MFC Calibration	GCF for N_2	Total GCF
1	100 % Ar	Top	50 [sccm] Ar	1.39	1.00
2	100% Ar	Top	100 [sccm] Ar	1.39	1.00
3	100% Ar	Top	100 [sccm] Ar	1.39	1.00
4	100% Ar	Top	100 [sccm] H_2	1.39	1.38
5	30% SiH_4; 70% Ar	Bottom	50 [sccm] Ar	1.04	0.75
6	CH_4	Bottom	100 [sccm] Ar	0.72	0.52
7	N_2	Bottom	50 [sccm] Ar	1	0.72
8	10% N_2; 90% Ar	Bottom	50 [sccm] Ar	1.38	1.00
9	100% Ar	Bottom	50 [sccm] Ar	1.39	1.00
10	10% O_2; 90% Ar	Bottom	50 [sccm] Ar	1.38	1.00
11	--	--	--	--	--
12	--	--	--	--	--

Since silane is a pyrophoric gas, special precautions must be taken to ensure safety. The silane is held in a special vented gas supply cabinet to protect against a build-up of the gas. The cabinet has a purging system that flows nitrogen through the lines, and valving if servicing is required. The heat produced from a small leak of silane has the potential to cause a catastrophic failure of the piping and since the supply line running from the cabinet to the system itself is fairly long and so contains an appreciable amount of silane, the silane line was vented through the main chamber when the system was not in use.

Section 5.2.9: Silane Dispersion Ring

Since the materials deposited are silicon based an even spatial distribution of silicon species in the plasma is a requirement for uniform film depositions. This requires a fairly uniform admission of silane into the growth chamber. The silane is allowed to flow into the chamber through a specially designed dispersion ring.

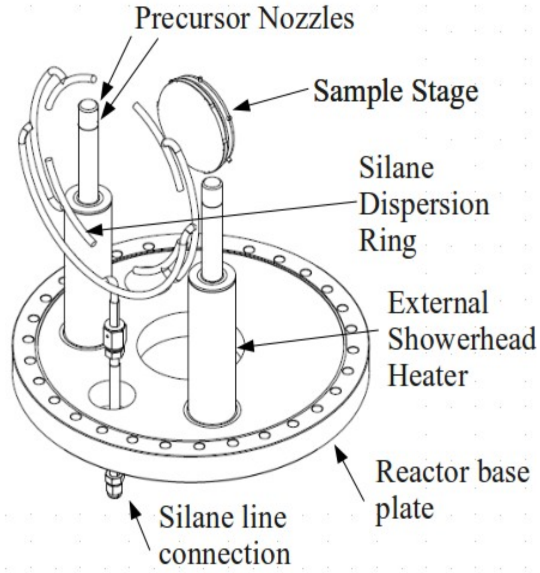

Figure 27: Internal geometry of deposition system showing the point of entry of silane and metalorganic vapour. Plasma source (not shown) is located to the left, aligned with centre of silane dispersion ring and sample stage. Adapted from [66].

The silane dispersion ring has a diameter of 7.25" and is divided into four sections of an arc made of 0.250" stainless steel tubing. Each section contains two pinholes which allow the silane mixture to flow into the chamber.

Section 5.2.10: Precursor Heating

The metalorganic precursors used for the *in situ* doping of the films with cerium or aluminium were loaded into the system in a nitrogen purged glovebox under standard temperature and pressure in a powder form. The precursors are placed into a specially designed canister (Figure 28) which can be heated in a relatively uniform manner.

Figure 28: Metalorganic precursor canister with custom heating jacket. Note recess for the insertion of thermocouple probe, heater thermocouple connection and standard VCR-2 male fitting.

The canister itself contains a recess into which a thermocouple probe can be inserted in order to have a more precise measurement of the internal temperature of the canister and hence the temperature of the precursor itself. The canister is then fitted with a custom electrical heating jacket and a standard male VCR-2 fitting at the top to allow it to be connected with a union tee adaptor on the precursor carrier gas line. A small copper puck is placed between the underside of the canister and the insulation to give an additional thermal mass at the bottom of the canister, where for practical purposes electrical heating would be difficult to incorporate. This additional mass, after equilibrium is reached, reduces the effective heat loss from the bottom of the canister, reducing the thermal gradient in the canister and ensuring a more even temperature distribution in the precursor.

Since the stability of the precursor temperature is crucial for the repeatability of the doping, great care was taken to ensure proper thermal control of the precursor canister. This was accomplished using a Eurotherm 2408 Proportional, Integral, Derivative (PID) temperature controller.

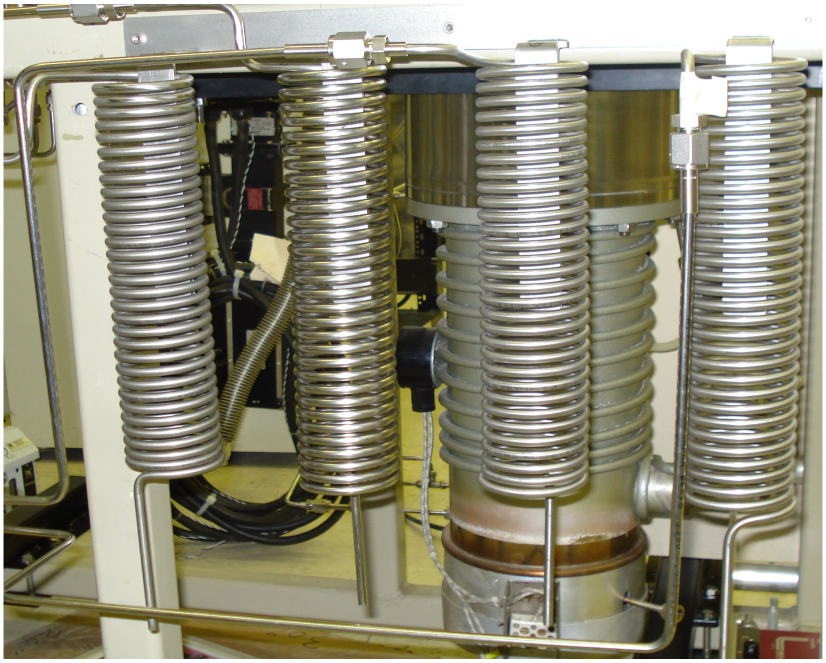

Figure 29: Gas preheater coils prior to the installation of heater tape and insulation

The original temperature control scheme was to use feedback from the thermocouple placed in the recess of the canister to control the heating jacket output in order to stabilize the “internal” temperature of the precursor canister. This proved to be impractical due to the relatively low thermal mass and good insulation of the heating jacket.

The temperature setting was increased slowly to approach the target temperature and the heater temperature would consistently overshoot the target while the temperature measured in the recess of the canister would remain below the target. The recess temperature would then follow and overshoot the target temperature quite dramatically, reaching a maximum temperature of ~280 °C before the heating was manually disengaged.

Both automatic and manual feedback parameter tuning methods suggested by the temperature controller manufacturer [69] were followed in order to reduce the overshoot and subsequent oscillations, however, the problem remained. A mixed tuning cycle in which the initial feedback parameters were set using feedback from the heating jacket thermocouple and used as a starting point for tuning with the recess feedback were also unsuccessful, resulting in significant oscillation. Finally, programming strict maximum-output and maximum ramp rate limits into the controller was attempted to further slow down the response of the heating jacket, but suitably stable operation could not be reached. In all of these cases the heating jacket heated up too quickly and could not cool off before the canister crossed the target temperature resulting in the target temperature to be overshot.

Since stable operation could not be reached using the recessed thermocouple for feedback, the system was reconnected and parameters were re-tuned to use feedback from the thermocouple located in the heating jacket lining. In this configuration the temperature stability of the jacket was ~ 1° C.

The canister would then be allowed to slowly heat up and come into equilibrium with the heating jacket. In order to reduce start up time, the heating jacket target temperature would usually be set 5-10° C higher than the canister target temperature and then reduced to the proper temperature as the canister temperature approached the target temperature. Using this method, the canister temperature overshoot would usually not exceed 2-3° C if any was observed. Once the target temperature was reached, the system would usually be left idling for approximately 20 minutes to ensure that equilibrium inside the canister was truly attained.

Section 5.2.11: Precursor Nozzles

The precursor vapour, sublimated in the heated canister, is allowed to mix with the argon carrier gas flowing down the lines. The precursor enters the chamber through two showerhead columns located between the silane dispersion ring and the sample stage as shown in figure 27. To minimize the potential for condensation or deposition of the precursor onto the showerhead nozzles or internal tubing, the shower head is fitted with external heaters.

The heaters consist of thin heater tape wrapped around the base of the columns inside the recess of the chamber. The columns were held at a temperature of 235° C for all of the depositions.

Since the system is specifically designed for co-doping with up to four metalorganic precursors, cross-contamination is a significant issue. While periodically baking out the lines under an argon flow can be used to reduce residual precursors found on the tubing walls, this procedure does not ensure total purity. For this reason, a dual nozzle was installed in the system. The first nozzle is connected to precursor line #1 while the other three lines meet to feed the second nozzle. This compromise allows relative line cleanliness to be maintained while keeping system complexity down. For the experiments described in this work, no co-doping was attempted and so only the individual precursor nozzle was used.

Section 5.2.12: Heating Tape/Insulation

Maintaining a sufficient temperature of the dopant supply tubing is necessary to prevent condensation of the precursor on the piping walls. The final design of the pipe heating assembly consisted of three layers applied to the pipes. Heater tape is wrapped around the pipe to supply the necessary heat and this layer is wrapped in insulation. Finally the whole structure is tightly wrapped in aluminium foil (Figure 30).

The complex layout of the piping used for the four dopant supply lines required the use of 18 separate sections of heating tape ranging in length from 4' to 16'. The design selection criteria for the heating tape were:

- Use on conductive surfaces
- Operation near temperatures of 300° C
- Reliability and long, maintenance free work-life
- Sufficient flexibility to be tightly wrapped around the 1/4” tubing

Particular attention was given to the wrapping of the pipe, which required dense spacing of the heater tape without touching or overlap, to reduce hot spots and the potential for local failure of the tape. Since the piping is difficult to access and in some areas would require the shutdown of the vacuum system to access, reliability was a priority. For this reason, heater tape designed for 240 V operation was used with a driving voltage of 120 V to ensure that, at the required power, the current would be significantly below the rated operating current of the tape to reduce the chance of failure.

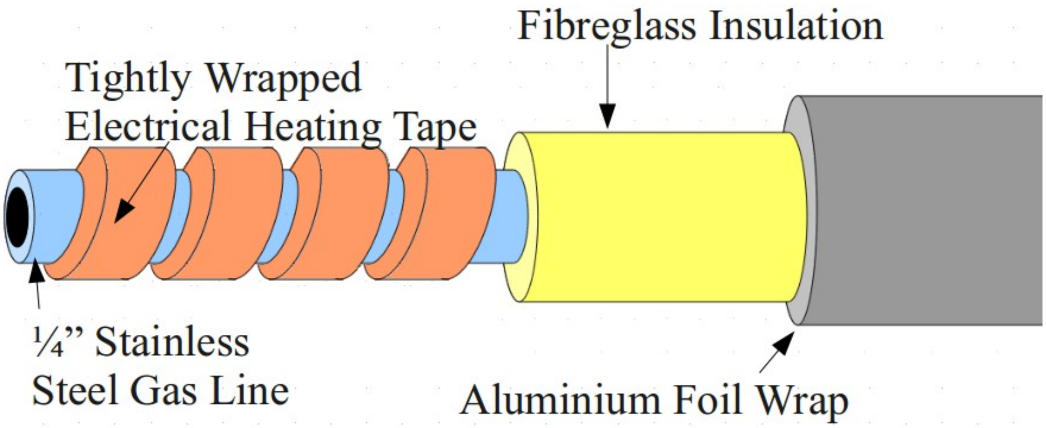

Figure 30: Layers of the heated precursor supply line

After wrapping a test section of pipe to determine the ratio between heater tape length required for wrapping and pipe length, the necessary lengths of heater tape were selected and installed. The piping was the fitted with fibreglass insulation jackets and joint, corner and valve sections were filled with mat and loose fibreglass. The insulated pipe was then wrapped in aluminium foil to hold the insulation and seal any potential air leaks.

The temperature control was handled using a PID temperature controller with feedback provided by a K-type thermocouple probe. Multiple probes were taped onto the piping in areas which were likely to have a lower than average temperature and the coldest reading was used as feedback for the temperature controller. Two additional probes were left connected so that a rough measurement of the range of temperatures along the piping could be monitored. The nominal piping temperature was set to 250° C.

Section 5.2.13: Sample Stage Heater

Since substrate temperature is one of the most important process variables during the depositions, particular attention must be directed to the control and measurement of the sample stage heater. Direct substrate surface measurement is difficult to implement in practice and monitoring during the growth would be too complex to implement. For this reason, only the stage heater temperature is monitored and while the substrate temperature is expected to vary significantly from the stage temperature it is assumed that during the steady state conditions of the deposition cycle a stable stage temperature is indicative of a stable substrate temperature.

The heater itself is mounted directly behind the sample stage and is powered through a special feed-through at the base of the sample stage arm so that the stage can rotate during deposition without cutting power to the heater. Phase angle modulation controlled via a high power solid state relay is used to control the power fed to the ceramic heater element. This modulation method reduces abrupt changes in the effective current flowing through the heater and gives a smooth heater output response.

Section 5.2.14: Computer PID control and Interlocks

Since the deposition system is composed of a large number of subsystems, each of which each requires monitoring, a computer interface was used to simplify the operation of the system. While the plasma generation system, shutters, residual gas analysis, stage temperature and sample positioning were all manually controlled, the majority of the other subsystems, including the vacuum pumps, gate valves, pressure measurement system and gas flows controls were all integrated into the computerized interface. While ease of use was a major benefit of this interface, the system also allowed the implementation of safety interlocks designed to protect the vacuum system from operator error or failure of components.

Section 5.3: System Maintenance

System maintenance was mainly focused on maintaining a clean vacuum environment. The deposition of material on the walls of the chamber is unavoidable during the ECR-PECVD process. This, combined with the condensation of residual moisture work to contaminate the vacuum environment as outgassing from the walls releases contaminants, particularly hydrogen which can become incorporated in higher amounts in future growths. Proper cleaning procedures can help to prevent this.

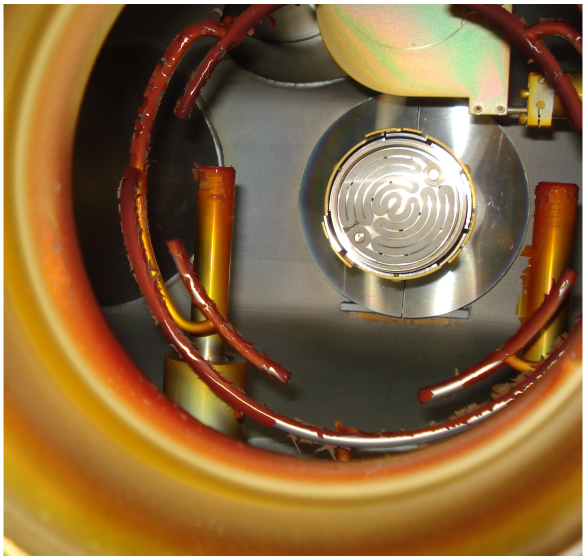

Figure 31: Reactor sidewall depositions prior to mechanical cleaning during system maintenance shutdown. Dark red colour implies high cerium content. Visible in the photograph is the dispersion ring, dopant delivery showerhead columns, sample stage and heater as well as the manual shutter, shown in the raised or open position.

A full chamber cleaning procedure was carried out when necessitated by the breaking of the vacuum for maintenance tasks as well as changes in the planned growth types. The cleaning cycle requires baking the chamber at a temperature of 150° C using externally applied heater tape to encourage the outgassing of the chamber walls. The contaminants released are then pumped away through the vacuum system. Following this, thorough plasma cleaning is performed using a high power argon plasma. During this process, the argon flow rate is adjusted to maintain a pressure of approximately 1.5 mTorr at a plasma power of 800 W for a period of 40-60 minutes. The resultant high energy argon ions sputter the deposited species from the walls of the reactor and the contaminants are again pumped out through the vacuum system.

Section 5.4: Heating of Plasma Chamber

During the initial depositions it was noticed that the walls of the plasma chamber were heating up significantly during depositions. This was likely due to the poor axial confinement of the plasma resulting from the single magnet configuration. Since it was feared that this could lead to some sputtering of the chamber walls resulting in the contamination of the samples by species related to the stainless steel, the films were analyzed using Secondary Ion Mass Spectrometry (SIMS) by our industrial partner, Group IV Semiconductor. It was determined that the concentrations of chromium, cesium and iron species were low enough to rule out sidewall sputtering related contamination.

The heating of the plasma chamber still needed to be addressed and so a water cooling system was devised for the walls. 1/4" OD copper tubing was coiled tightly around the exterior of the plasma chamber and fittings were installed to route the piping through the chamber bolt holes in a manner that would not interfere with the positioning of the magnet. A thermocouple probe was attached to the chamber. Chilled water was then circulated through the tubing to externally cool the chamber. Thermal contact between the chamber and the cooling coil was accomplished using pipe clamps to hold the coil firmly against the chamber. After pump-down the seal was tested and a thermocouple was inserted into a recess in the joint between the dispersion ring and the chamber flange. With the cooling system installed the chamber wall temperature does not exceed 40° C in steady state operation even under the 800W cleaning plasma.

Section 5.5: Manual Shutter Operation

Gas flows are set and the plasma is struck prior to the start of the deposition. During this time the substrate, which had been moved from the sample transfer position to the deposition position is shielded from the ion flux by a large shutter mounted on a rotational magnetic feed-through, which allows it to swing up to uncover the substrate and sample stage. This exposes the substrate to the plasma flux and allows the deposition to begin.

Although this simple system is sufficient for the growth of simple devices with few layers, for devices with a large number of layers, an automatic shutter which could close at precisely determined times to allow changing of the gas flows and chamber composition would be preferable. The design of the shutter could be improved greatly if the open position was lower than the closed position, since this would reduce the chances of the shutter falling due to vibrations during the sample transfer procedure which has caused problems during the operation of the system.

Chapter 6: Results of Preliminary Growths

Section 6.1: System Testing and Initial SiO$_x$ Growths

System testing was begun before the high vacuum system was fully operational, in order to keep up with the timeline of the industrial partner, Group IV Semiconductor. In particular, the main chamber turbo pump was not functioning correctly, so the chamber pressure was maintained by the roughing stack and the temperature control solid state relay delivered with the system had to be replaced, so heater temperature control was not available.

Prior to the installation of the solid state relay used to control the heater power, depositions of SiO$_x$ films were preformed nominally at room temperature. It should be noted that many factors including thermal conduction through the main chamber and sample holder arm from the showerhead heater as well as the natural plasma heating of the sample holder were not taken into account. The actual substrate temperature was not monitored.

The first depositions, of samples WNP5-175 and 176 were performed using a 10% oxygen-in-argon flow of 30 sccm with 30% silane in argon as the silicon precursor. The deposition rates for the samples were found to vary from 6.8 to 8.2 nm/min. The results of the first two depositions are shown below in Table 2. The film indices of refraction straddle the nominal stoichiometric composition index and the test indicated that the plasma striking and gas delivery worked satisfactorily.

Table 2: Summary of first two depositions conducted at room temperature with O2/Ar flow of 30 sccm.

Sample	SiH_4/Ar [sccm]	Growth rate [nm/min]	Thickness Non-uniformity	Index
WNP5-175	5	6.8	2.7%	1.374±0.10%
WNP5-176	10	8.2	2.9%	1.501±7.3%

After an overhaul required to repair the shutter mechanism and alignment of the sample transfer mechanism caused either by the post-manufacturing relaxation of stress in the sample arm or slipping of the set screw settings of the transfer system, room temperature film depositions were performed. As seen in Table 3 below the reproducibility of the depositions without proper substrate temperature control was poor.

Table 3: Deposition conditions and film parameters for 20 minute depositions

Sample	SiH_4/Ar [sccm]	O_2/Ar [sccm]	Baratron pressure [mTorr]	Thickness [nm]	Non-uniformity	Index
WNP5-179	10	30	91.4	115.3	8.70%	1.521
WNP5-184	10	30	92.6	96.7	2.70%	1.492
WNP5-185	10	30	93.7	144.2	3.10%	0.000

After the arrival of the proper phase angle controlled solid state relay, the installation of the substrate heater and Eurotherm 2408 PID temperature controller was completed. Multiple tuning cycles were carried out centred around the expected deposition stage temperature of 300° C in order to set the thermal damping and heater response parameters of the system. This is done by a cycle in which the heater is turned off, allowing the temperature to drop and then running the heater for a short pulse. By monitoring the effect of this pulse-cycle on the temperature, the controller approximates the parameters needed for a critically damped response. The controller was set in automatic tuning mode so that through further observation of the temperature response during standard operation the parameters are refined and adjusted for drift [70].

Direct substrate temperature measurements were not carried out due to the difficulties in mounting an appropriately positioned thermocouple feedthrough, a time consuming task requiring a properly positioned free port. Prior work on an Inductively Coupled Plasma Enhanced Chemical Vapour Deposition (ICP-PECVD) system in the CEDT laboratories with a nearly identical sample stage, heater and control systems were, however, carried out in the past [71]. The results of these studies yielded a linear relationship between the stage and substrate temperature (in ° C) [71]:

$$T_{substrate} = 0.3303 \mathrm{x} \mathrm{T}_{stage} + 21.58 \tag{63}$$

The thermal response in the present ECR-PECVD system is expected to be similar to that of the ICP system, so a stage temperature of 300° C would yield an assumed substrate temperature of approximately 121° C.

With the available temperature control, three sets of samples were prepared to study the effect of deposition pressure, silane/oxygen ratio and plasma source/dispersion ring to substrate distance on the refractive index and growth rate of the SiO_x films. The deposition parameters used are summarized in Table 4. Some minor plasma stability issues were experienced for the deposition of WNP5-198, WNP5-199 and A-1 in which reflected power momentarily increased to ~65 W. However, given the long deposition times, this is not expected to significantly impact the overall film characteristics. The effect of distance on the thickness and refractive index are shown in Figure 32. As one might expect, bringing the sample closer to the dispersion ring increases the refractive index. This would indicate that the films grown close to the dispersion ring through which the silane enters the chamber are silicon rich as they are grown in an area in which the silane concentration is higher. Although all of the values are above the stoichiometric/thermal oxide value of 1.465, a very large increase is seen at the 50 mm position. The decrease in the growth rate most likely indicates that although an excess of silane (and so dissociated or partially dissociated silicon species) is present, the excess silane effectively shields the adsorption of oxygen atoms on the surface through gas phase interactions leading to an overall reduced growth rate.

While it would be of great interest to extend the range of substrate-plasma distances studied, this would require the effective rebuilding of the entire sample positioning mechanism, which would prove difficult and costly and would not be practical given the time-line for this project.

Table 4: High-pressure deposition parameters and film properties for the study of Pressure, Silane:Oxygen Ration and substrate distance in the growth of SiO_x *films. Magnet current was kept constant at 180 A ± 0.75 A for all of the runs.*

Date	WaferID	Wfr Pos'n	Dep Temp (˚C)	SiH_4/Ar (sccm)	O_2/Ar (sccm)	For / Rev Power (W)		Bara (mTorr)	Dep Time (min)	SiH_4/Ar : O_2/Ar	Thick (nm)	Dep Rate (nm/min)	Range (nm)	Non-U (%)	Index	Index Range
	Effect of Pressure															
26-May	WNP5-192	35	300	2.4	5	508	3	27.8	40.0	0.48	339.0	8.5	3.4	0.5	1.515	0.0095
26-May	WNP5-193	35	300	4.8	10	501	1	46.8	40.0	0.48	295.0	7.4	1.1	0.2	1.656	0.0114
27-May	WNP5-195	35	300	7.2	15	503	5	62.9	40.0	0.48	298.3	7.5	2.7	0.4	1.729	0.0175
27-May	WNP5-196	35	300	9.6	20	502	3	76.6	40.0	0.48	295.2	7.4	4.2	0.7	1.800	0.0127
	Effect of silane:oxygen															
27-May	WNP5-197	35	300	6	12.5	503	1	56.5	40.0	0.48	296.7	7.4	2.6	0.4	1.729	0.0126
28-May	WNP5-198	35	300	8	10.5	503	2	55.4	40.0	0.76	315.0	7.9	22.2	3.5	2.841	0.1900
28-May	WNP5-199	35	300	10	8.5	507	10	55.3	40.0	1.18	340.3	8.5	5.6	0.8	2.716	0.0789
28-May	A-1	35	300	12	6.5	516	20	56.6	40.0	1.85	289.3	7.2	9.9	1.7	3.722	0.0285
	Effect of distance															
31-May	WNP6-027	20	300	6	12.5	502	3	54.8	40.0	0.48	321.3	8.0	1.7	0.3	1.654	0.0000
31-May	WNP5-197	35	300	6	12.5	503	1	56.5	40.0	0.48	296.7	7.4	2.6	0.4	1.729	0.0126
31-May	WNP6-026	50	300	6	12.5	501	1	56.1	40.0	0.48	270.4	6.8	12.5	2.3	2.945	0.0213

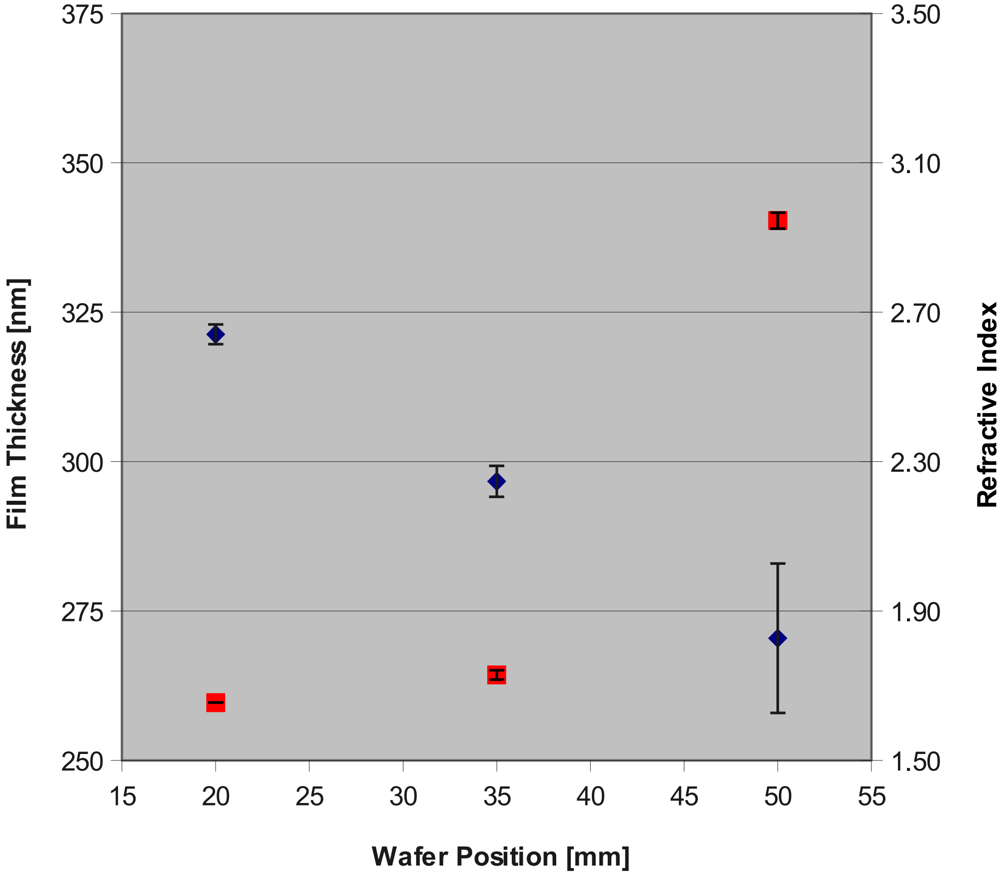

Figure 32: Effect of sample distance on thickness (blue diamonds) and refractive index(red squares). The scale is positioned arbitrarily at a position of ~50 cm from the mouth of the plasma source and an increase in the scale measurement indicates that the sample is closer to the dispersion ring/plasma source. Temperature 300 °C, $SiH_4/Ar:O_2/Ar=0.48$, Pressure= 55.8±0.9 mTorr, Forward power=502±1W, Deposition time = 40 min

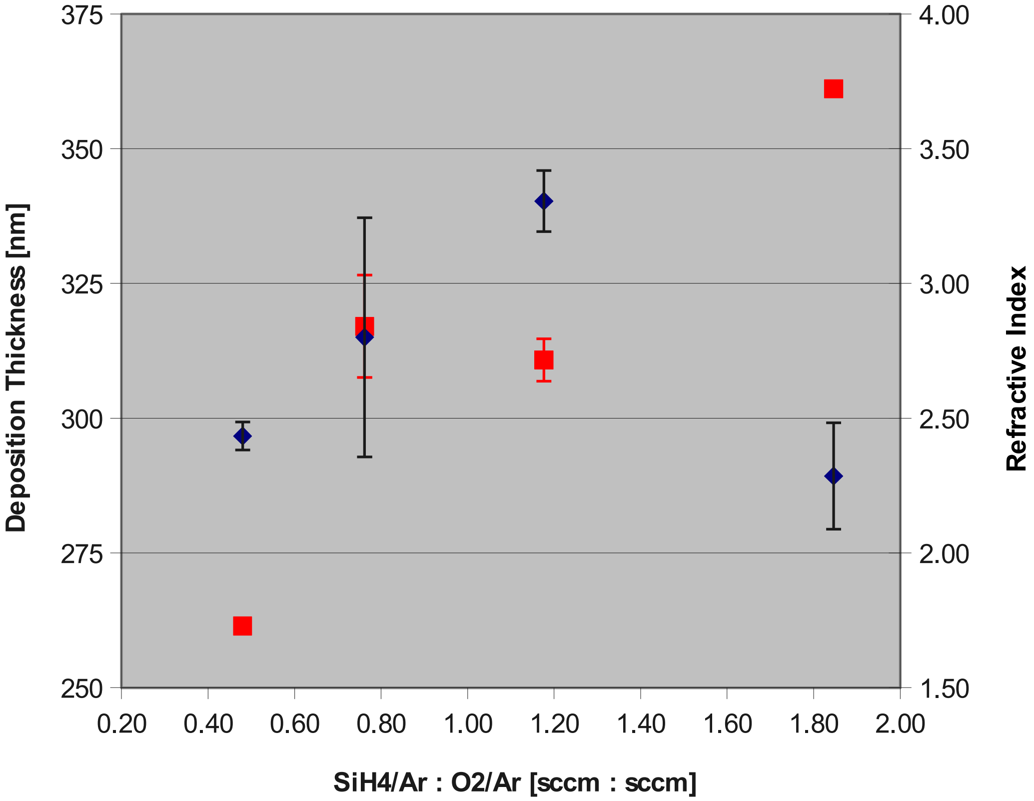

Figure 33: Effect of SiH_4/Ar:O_2/Ar ratio on refractive index (red squares) and thickness (blue diamonds).

Wafer position = 35mm, Temperature = 300°C, Pressure = 56.0±0.7 mTorr, Forward power = 505±5 W, Deposition time = 40 min

The refractive index is seen to increase with increasing silane content as would be expected as the films become more silicon rich, as shown in Figure 33. The refractive index for all of the films would indicate that all of the films are silicon rich. The significant decrease in the thickness for sample A-1 may be a result of the poor plasma stability during the growth but given the short period of the reflected power spike is most likely attributable to the reduction of available oxygen. A repetition of the deposition and another deposition between this ratio and 1.18 could determine if this point is an experimental aberration or if the pattern is consistent.

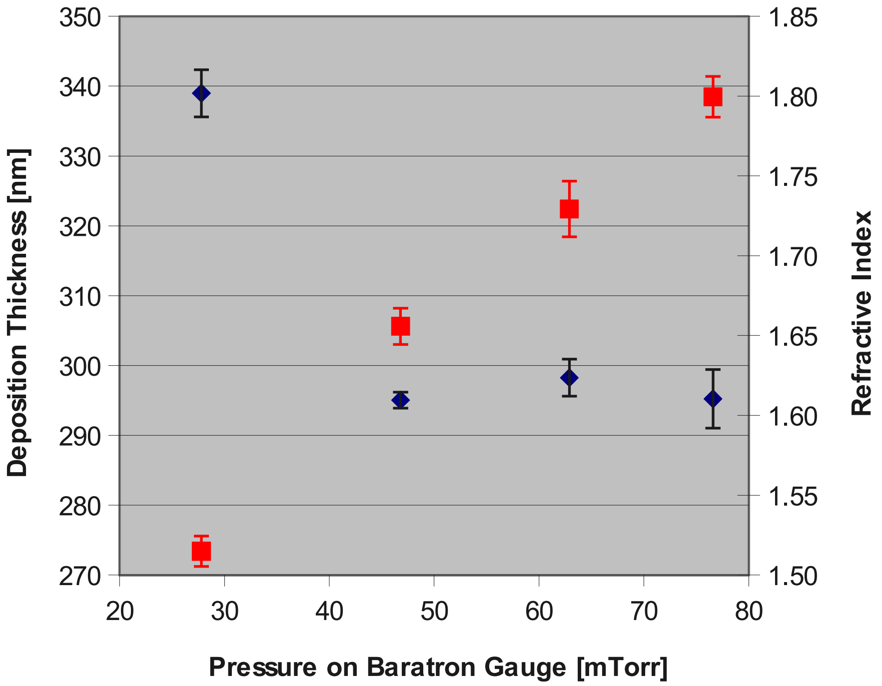

Figure 34: Effect of deposition pressure on refractive index (red squares) and thickness (blue diamonds).

SiH_4/Ar:O_2/Ar = 0.48, Wafer position = 35 mm, Temperature = 300° C, Forward power = 505±5 W, Deposition time = 40 min

The effect of varying the deposition pressure can be seen in figure 34. Although the refractive index does change with the pressures the change is significantly less than the change seen with variation of the gas ratios and distance. The growth rate decreases quickly between the first two measurements but remains fairly constant at higher pressures.

Section 6.2: Low Pressure SiO_x Depositions

Once the main chamber pump was refurbished and ready for service a series of SiO_x films were prepared at low pressures. The results shown as a function of $SiH_4/Ar:O_2/Ar$ ratio are summarized in Figure 35 and the deposition parameters are summarized in Table 5.

Table 5: Deposition parameters for low pressure silicon oxide and silicon rich silicon oxide growths. Plasma power was ~500W, stage position was 35mm and substrate temperature was 300 °C for all growths.

WaferID	SiH_4/Ar [sccm]	O_2/Ar [sccm]	Bara [mTorr]	Dep Time [min]	$SiH_4/Ar : O_2/Ar$	Thickness [nm]	Index
WNP6-048	5	30	2.9	30.0	0.17	103.4	1.459
WNP6-041	5	30	2.8	30.0	0.17	98.6	1.465
WNP6-045	5	30	3.1	30.0	0.17	101.7	1.462
WNP6-039	10	30	2.8	20.0	0.33	106.0	1.629
WNP6-043	12	30	3.45	20.0	0.40	122.8	1.670
WNP6-044	13.5	30	3.55	20.0	0.45	114.1	1.866
WNP6-049	13.5	30	3.39	20.0	0.45	118.1	1.795
WNP6-042	15	30	3.6	30.0	0.50	217.1	2.133

As can be seen by the repetition of the growth conditions for WNP6-041 and WNP6-045, the growth at the lower pressure yields refractive index values near that of a thermal oxide (as compared to WNP6-029) and good repeatability is obtained. WNP6-048 was deposited on a HF-cleaned wafer and maintains the expected film characteristics. WNP6-049 repeated the growth of WNP6-044 on a wafer stripped of the native oxide. The refractive indices measured for repeated depositions of silicon rich oxides conducted varied more than those measured for repeated depositions of near stoichiometric compositions.

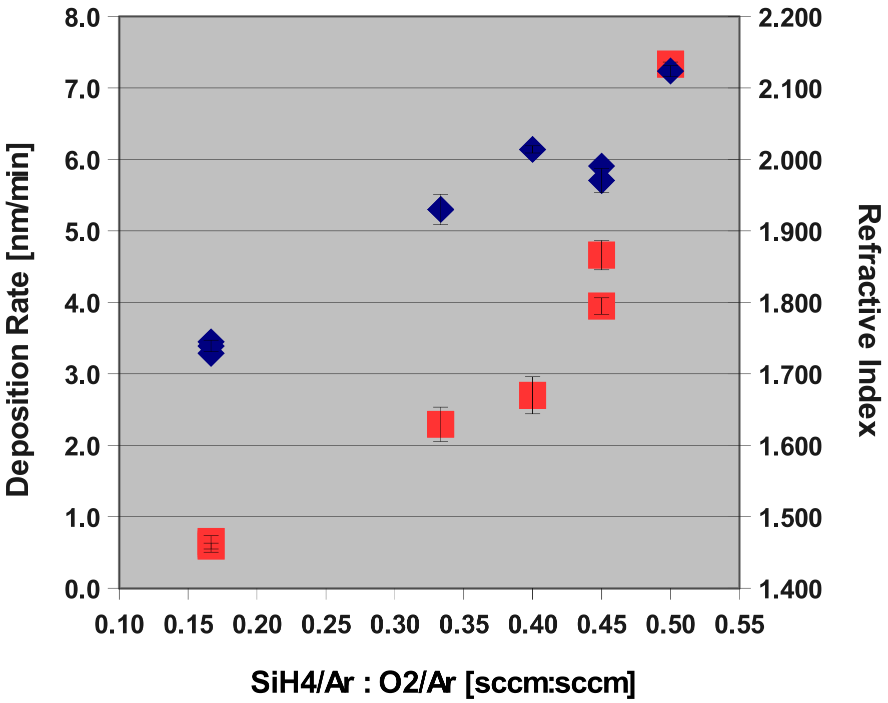

Figure 35: Effect of SiH4/Ar:O2/Ar ratio on the growth rate (blue diamonds) and refractive index (red squares) of low pressure depositions of SiO_x *at a pressure of ~3 mTorr.*

Error bars indicated range (maximum deviation)

Table 6: Deposition parameters and film characteristics for depositions of SiO_x ($x\approx2$) films at different substrate temperatures

Sample ID	Heater Temp [deg C]	Silane [sccm]	Oxygen [sccm]	Pressure [mTorr]	Deposition Time [min]	Thickness [nm]	Growth Rate [nm/min]	Range [nm]	Non-Uniformity [%]	Index of Refraction
WNP6-041	300	5	30	2.8	30.0	98.6	3.3	2.3	1.2	1.465
WNP6-045	300	5	30	3.1	30.0	101.7	3.4	1.0	0.5	1.462
WNP6-048	300	5	30	2.9	30.0	103.4	3.4	1.1	0.5	1.459
WNP6-150	500	5	30	3.02	25.0	71.1	2.8	15.4	10.8	1.466
WNP6-153	700	5	30	2.98	45.0	90.8	2.0	5.6	3.1	1.462

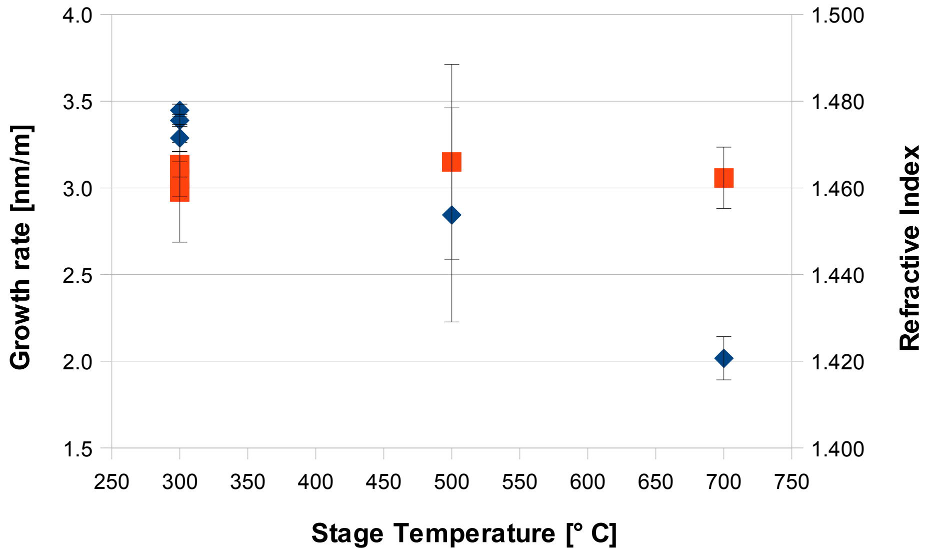

Figure 36: The effect of stage temperature on growth rate and index of refraction of silicon oxide films deposited under lower pressures are shown. The refractive index (red squares) is quite stable with deposition temperature. The growth rate (blue diamonds) drops off linearly with increasing temperature. The small spread of both the growth rate and refractive index for the three growths at 300°C indicates good repeatability under these conditions.

While it is clear from these results that the repeatability of the depositions is greatly improved by the lower pressure and improved temperature control, a wider future study should be conducted to give greater statistical significance to the results and to investigate any possible parameter drift that may be present in the system instrumentation.

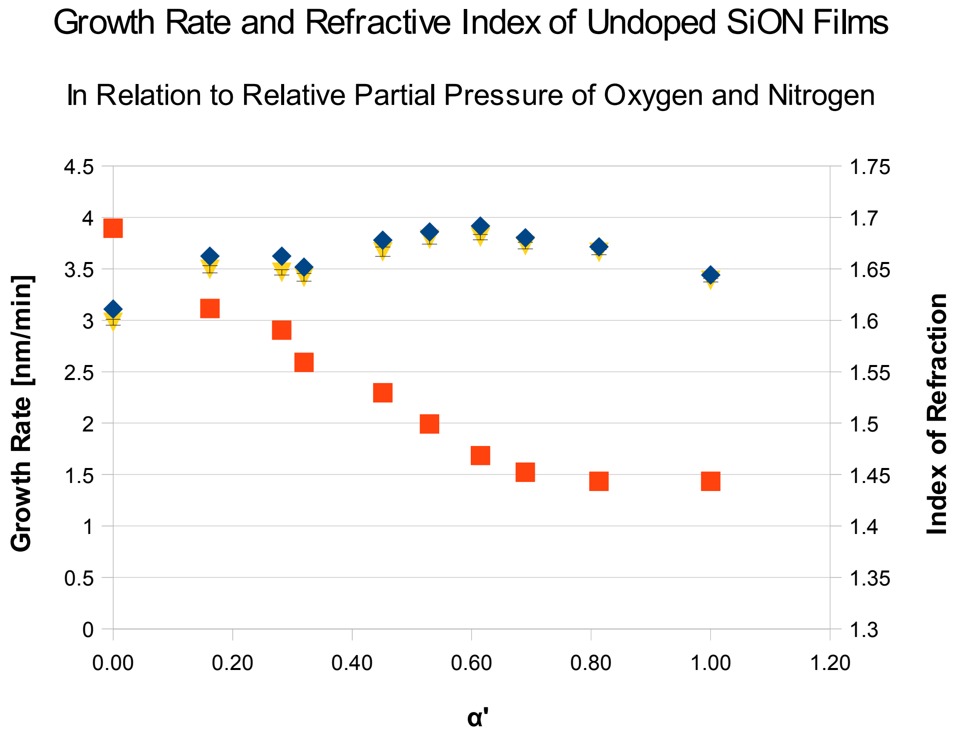

Figure 37: Growth rate measured by VASE (blue diamonds) and refractive index (red squares) of the series of undoped silicon oxynitride films shown with changing oxygen partial pressure.

α' denotes the ratio of the patial pressure of oxygen/argon mixtures to the combined partial pressure of oxygen and nitrogen mixtures.

Single wavelength raster scan average growth rates (yellow triangles) show good agreement between single wavelength and VASE measurements.

Error bars on the growth rate indicate widest ranges of thicknesses indicating non-uniformity of the film.

A brief study of the effect of substrate temperature on refractive index and deposition rate of the near stoichiometric films was conducted using the parameters listed in Table 6. Growths were prepared using sample stage temperatures of 300° C, 500° C and 700° C corresponding to approximate substrate temperatures of 121° C, 187° C and 253° C as calculated using equation 63. The refractive index was found to be quite stable for all of the depositions at a value of 1.463±0.003. The growth rate decreases linearly (R^2=0.98) with temperature and is found to decrease by 3.3 picometers/minute per degree increase in temperature, as seen in Figure 36. The trend indicates that the surface desorption increases at higher temperatures limiting the growth rate of the films. In order to limit the large number of degrees of freedom or process parameters and thus the complexity of the subsequent film characterization the later films were deposited at a stage heater temperature of 300 °C.

Section 6.3: Undoped Silicon Oxynitride Growths

Silicon oxynitride growths of varying compositions were prepared using a 10% nitrogen in argon mixture (Table 7). Ellipsometric measurements were taken with both a VASE system to obtain an accurate determination of thickness and refractive index and a single wavelength ellipsometer to determine film uniformity. The non-uniformity of the samples was quite low at 0.93% ± 0.25%. For the undoped silicon oxynitride films the growth rate (see Figure 37) is found to be ~3.5 nm/min. The index of refraction of the films is seen to decrease as the ratio of oxygen to nitrogen increases in the chamber, indicating that with abundant oxygen only a small amount of nitrogen is incorporated into the films. This is consistent with the expected higher stability of the SiO bond over the SiN bond.

Table 7: Deposition parameters for undoped silicon oxynitrides

Wafer ID	**Deposition Time [min]**	**SiH4/Ar [sccm]**	**O2/Ar [sccm]**	**N2/Ar [sccm]**
WNP6-045	30	5.0	30.0	0.0
WNP6-152	35	5.0	5.0	25.0
WNP6-155	25	5.0	0.0	30.0
WNP6-156	35	5.0	10.0	20.0
WNP6-157	35	5.0	15.0	15.0
WNP6-158	35	5.0	20.0	10.0
WNP6-159	35	5.0	25.0	5.0
WNP6-161	35	5.0	7.5	22.5
WNP6-162	35	5.0	12.5	17.5
WNP6-163	35	5.0	17.5	12.5

RBS analysis of a silicon nitride sample, WNP6-022d deposited under the same conditions as the film WNP5-155 indicates that the composition is $Si_{0.35}N_{0.65}$ and the film is therefore nitrogen rich. The increase in nitrogen in the film works to lower the index of refraction of the film in comparison to a pure Si_3N_4 film [73]. Future studies focused on the deposition of pure Si_3N_4 films with this system should include samples prepared with a lower silane flow. Proper bake-outs and plasma cleaning should be used prior to deposition to minimize the solvolysis of the Si-N bond by remnant water vapour and OH radicals. Studies attempting to fabricate SiO_xN_y films of low x should consider using a more dilute mixture of oxygen in argon as well as a reduced silane flow to slow film growth and ensure that the oxygen ion bombardment is low enough for the oxygen incorporation to be fully transport limited.

Section 6.4: Thickness Measurements

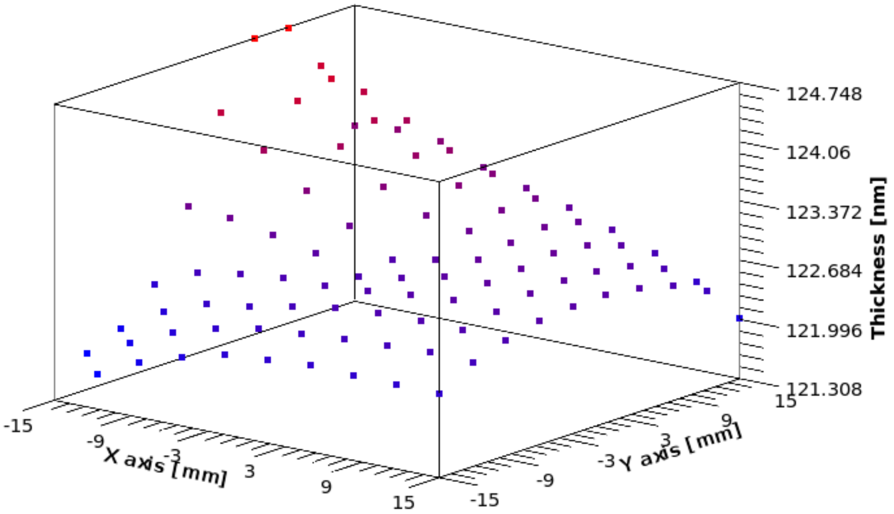

Figure 38: Non circularly symmetric thickness profile indicates that differing growth rates are not caused by steady state plasma nonuniformity. Possible cause can include uneven heating of substrate. Sample WNP6-043.

Predicting the thickness of films whose growth rate is not well established is difficult. The result is that some of the sample thicknesses fell near the insensitive period point region of the ellipsometric measurements. In this case, the index of refraction at 632.8 nm was measured using VASE and set as a constant so that the thickness and non-uniformity can accurately be determined.

The raster pattern used for most measurements was a 100x100pt grid covering an area of 3.000 x 3.0000 cm^2.

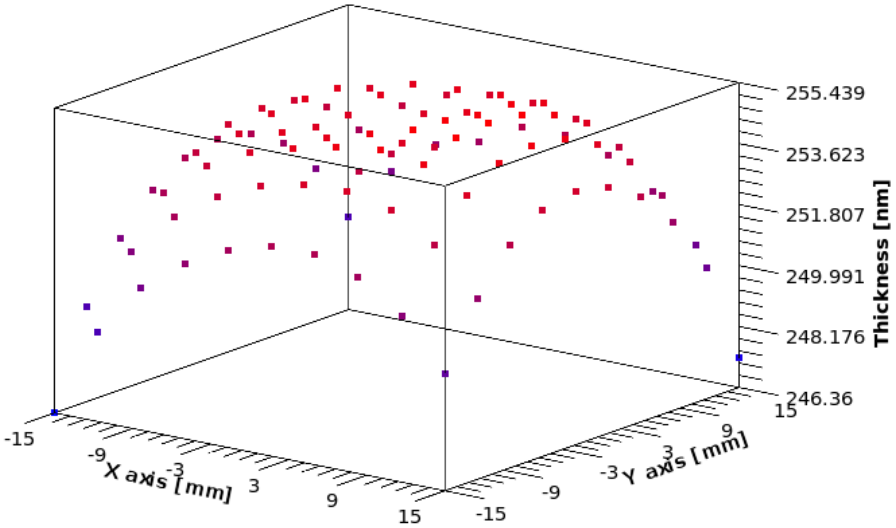

Figure 39: The tapered growth profile is seen for the majority of samples. Sample WNP5-005.

The rotation of the sample during deposition should result in a circularly symmetric thickness profile for all films such as the one shown in Figure 39. If the steady-state plasma density is uneven near the wafer or the stage is not normal to the ECR magnet axis, causing varying deposition rates, the circular symmetry would be maintained, however the profile could be concave or even exhibit a semi-toroidal bump. Non-circularly symmetric profiles are more likely caused by substrate issues, such as thermal contact issues between the substrate and stage, improper substrate positioning or surface contamination. Surface contamination would presumably lead to either a change localize around a point or a fairly abrupt transition in either the growth rate or refractive index of the film. For this reason, it is likely that growth profiles such as those seen in Figure 38 are caused by a thermal gradient present in the film during deposition. This could be caused by a minuscule deformation of the substrate caused by uneven and localized stress applied by the pins holding the substrate on the stage, which would lead to a slight steady-state temperature non-uniformity of the substrate.

Section 6.5: Ce-doped SiO_xN_y films

Ce-doping was accomplished using the $Ce(TMHD)_4$ precursor as discussed in the system description chapter. The deposition parameters for selected growths are given in Table 8. A large compositional range of silicon oxynitrides were attempted, with two flow levels of the Ar carrier gas for the precursor. The precursor heater temperature was held at roughly 220° C for all of the depositions.

The composition of the resultant films was found using RBS. Analysis was carried out with the SIMNRA 6.05 software using a dual ion scattering and small angle scattering models to improve accuracy of the thickness drop-off simulation and steep substrate signal. The experimental and computed spectra based on compositional models given in Table 9 are shown in Figure 40. To account for variations in the composition of the films, which showed substantial variation of the cerium concentration with depth a stepwise concentration change was used as shown for sample WNP5-015 in Figure 41.

Table 8: Deposition parameters for Ce-doped films

Wafer ID	Deposition Time [min]	Ce cell Temp [°C]	Oxygen [mTorr]	Silane [mTorr]	Nitrogen/Ar [mTorr]	Ce Carrier [mTorr]	Total [mTorr]	SiH4/Ar [sccm]	O2/Ar [sccm]	N2/Ar [sccm]	Al Carrier [sccm]
WNP5-000	35	220	0.62	0.00	0.00	1.12	1.74	0.0	6.2	0.0	10.0
WNP5-001	35	220	1.14	0.44	0.00	1.10	2.68	5.0	12.0	0.0	10.0
WNP5-002	35	220	0.58	0.44	0.00	1.10	2.12	5.0	5.9	0.0	10.0
WNP5-003	35	222	2.21	0.41	0.00	1.11	3.73	5.0	0.0	0.0	10.0
WNP5-004	35	220	0.49	0.40	2.20	1.10	4.19	5.0	5.0	25.0	10.0
WNP5-005	35	222	1.43	0.41	1.32	1.08	4.24	5.0	15.0	15.0	10.0
WNP5-007	35	220	0.88	0.46	1.80	1.09	4.23	5.0	10.0	20.0	10.0
WNP5-008	35	222	0.87	0.43	2.04	0.87	4.20	5.0	8.0	22.0	10.0
WNP5-010	35	220	1.08	0.44	1.59	0.79	3.89	5.0	12.5	17.5	10.0
WNP5-012	45	223	2.37	0.41	0.42	0.58	3.78	5.0	25.0	5.0	5.0
WNP5-014	45	225	1.02	0.42	1.79	0.57	3.80	5.0	10.0	20.0	5.0

Table 9: Composition of Ce-doped silicon oxynitride films acquired by RBS. Compositions listed are thickness weighted averages of models used in simulation spectra shown in figure 40.

Sample ID	Si [%]	O [%]	N [%]	Ce [%]	C [%]	Density (10^{22}/cm^3)
WNP5-004	13.7	36.5	6.5	3.1	40.3	5.6
WNP5-005	17.6	43.6	17.8	3.6	17.4	5.6
WNP5-007	16.9	29.2	12.1	3.6	28.2	5.0
WNP5-008	17.9	50.4	16.2	3.9	11.6	6.7
WNP5-010	17.3	45.5	5.5	3.5	28.3	5.1
WNP5-012	19.3	47.7	7.7	4.7	20.6	3.85
WNP5-014	12.0	47.5	10.0	3.4	27.1	5.5
WNP5-015	11.9	40.8	9.4	3.1	34.8	5.9

The experiments were performed using a 2MeV ${}_4He^+$ ion beam at the Tandetron Accelerator Laboratory at the University of Western Ontario. Measurements were performed at an angle of incidence 5° from normal and random rotation of the sample to reduce channeling effects. The scattering angle was 170°. Dosages for the experiments were 6 μC.

It should be noted that the sensitivity of RBS decreases very quickly with reduced atomic mass. The poor sensitivity to carbon increases the errors involved in quantitative determination of carbon content in the films. This increases the statistical uncertainty for the carbon content in these films which is found to be in the vicinity of 3%. Further complications arise from the overlap of oxygen and nitrogen peaks for films of such thickness. The uncertainty associated with nitrogen is found to be on the order of 1% while for oxygen, silicon and cerium the uncertainty was found to be below 0.5%.

While the insensitivity to carbon is a physical limit of the characterization technique, oxygen and nitrogen could be better resolved through the use of thinner samples. If studies of doped SiO_xN_y samples fabricated using this deposition system are planned for the future, compositional calibrations should be done with much thinner samples which would produce more discernible oxygen and nitrogen peaks.

While most spectra in Figure 40 show an even distribution of Ce throughout the thickness of the film some samples exhibit a lower incorporation of the rare earth during the earlier stages of the growth. The gradient distributions were approximated using multiple stepwise increases in concentration. While the argon carrier gas flow was decreased for later film growths, the effect on the measured cerium incorporation was not substantial.

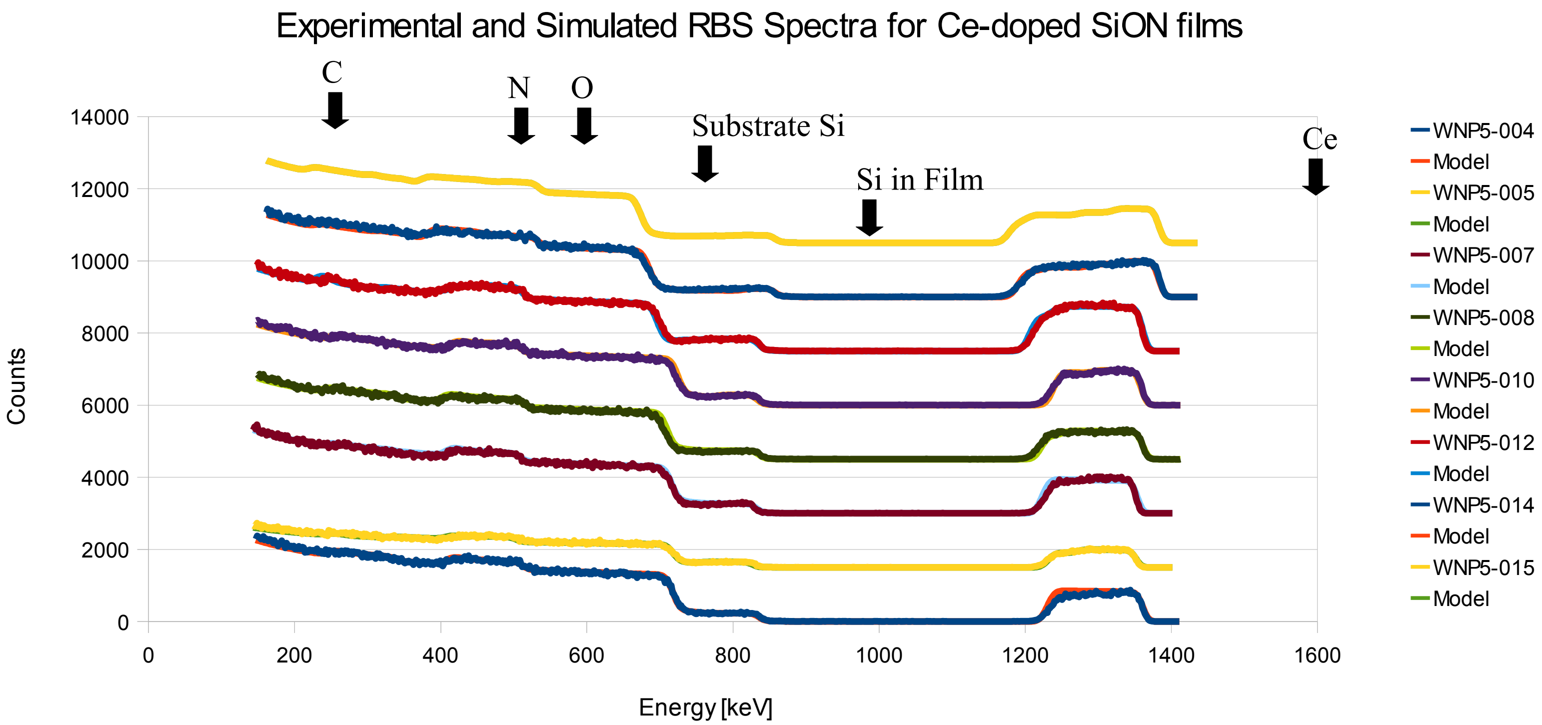

Figure 40: Experimental and simulated RBS spectra of Ce-doped SiON films. Note the diminishing size of features with reduced elemental mass and overlap of oxygen and nitrogen peaks.

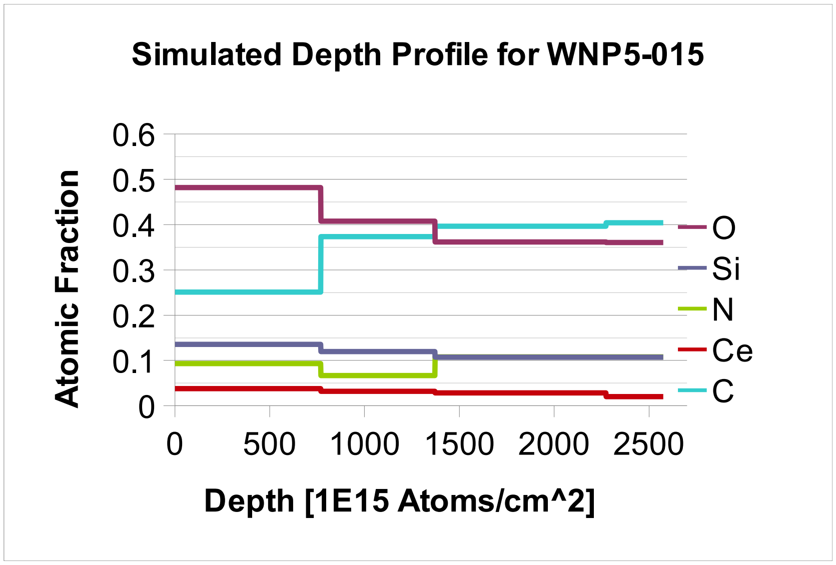

Figure 41: Depth-Composition map used for the simulation of the RBS spectrum for sample WNP5-015. The sample is divided into depth regions which are simulated as an series of separate films. Compositions are chosen to give the best possible fit to the experimental data.

The likely source of the carbon contamination is a degradation of the metalorganic precursor used as a cerium source. The precursor temperature used for most depositions of ~220 °C is quite high in comparison to its melting point of 275 °C [72]. Repetitive thermal cycling and short high temperature (~280 °C) exposure during the sublimator temperature calibrations may have caused a partial breakdown of the precursor resulting in the release of carbon containing molecules of comparatively lower molecular mass which would in turn lead to an increase in the adsorbtion of the carbon onto the surface of the sample.

The high carbon concentration causes a significantly increased growth rate as compared to the undoped SiO_xN_y films. The density of the films was calculated from the atomic density measured by RBS and thickness measured by spectroscopic ellipsometry. The variation of densities of the films is quite small, ~15%, and the densities on the same order of magnitude as crystalline silicon.

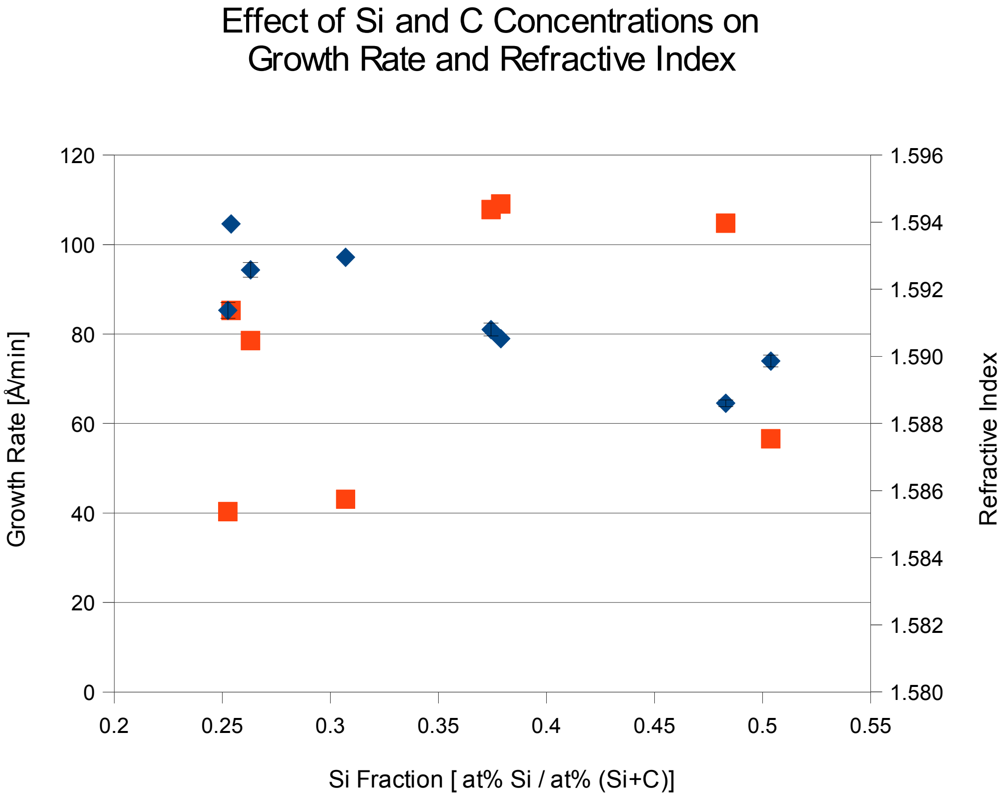

Figure 42: Although growth rate (blue diamonds) seems to decrease with relative silicon concentration, limiting other film parameters would give more defined results

The variation of the measured refractive index is quite small varying less than 1%. The refractive index does not appear to be strongly linked to the film density, however the wide range of compositions makes determining the actual effect of density on the refractive index difficult without a larger, less diverse sample set..

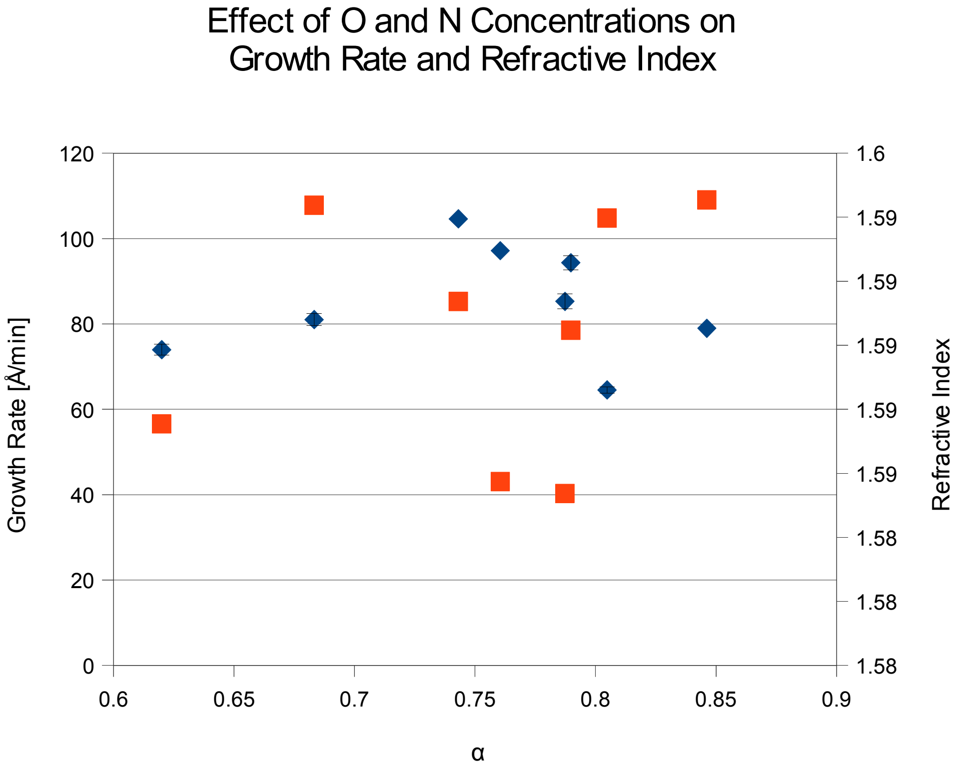

Figure 43: The large number of unfixed degrees of freedom in these film systems make determination of effect of individual elemental contributions difficult.

The small number of samples in such a large parameter space makes the determination of any trends in the growth dynamics with respect to sample composition nearly impossible to determine. It does however appear that an increase in the relative amount of carbon in the samples does lead to an increase in the growth rate (see Figure 42). This could be a result of of the the large molecular size of the precursor ligands associated with the presence of carbon. The effect on the refractive index is not clear.

The effect of the relative concentrations of oxygen and nitrogen on the growth dynamics are even less clear (see Figure 43). It would be expected, given the high carbon concentration and large amount of oxygen present in the films that the nitrogen has a relatively small effect on the growth dynamics. The difficulties in further studies of the effect of individual elemental contributions to growth dynamics and optical properties come from the fact that it is nearly impossible to fix the other compositional degrees of freedom in the system. This is particularly true in the case of carbon for which, as an unexpected impurity, no direct control pathway was anticipated.

Section 6.6: Photoluminescence of Annealed Ce-doped SiO_xN_y Samples

Annealing runs prior to photoluminescence measurements are required to allow for diffusion of the atoms in the sample. This can lead to, among other things, small scale phase separation leading to cluster formation, particularly in silicon rich samples; defect reduction or diffusion; as well as a change in particular bonding arrangements for the dopants. The latter is of particular interest in the photoluminescence from Ce in Si-based systems, since it allows the tetravalent Ce ion to optically activate in a trivalent bonding arrangement.

Annealing conditions were chosen based on conditions found to enhance photoluminescence in other rare-earth doped silicon based materials [76]. The annealing was performed using a tube furnace under a nitrogen flow to reduce the possibility of oxygen or other atmospheric contamination. The samples were cleaved into pieces generally slightly smaller than 1 cm^2. Annealing temperatures were increased in 100° C steps from 400 to 1200° C and each annealing was performed for a 60 minute interval. An additional 120 min anneal was performed at 1200° C.

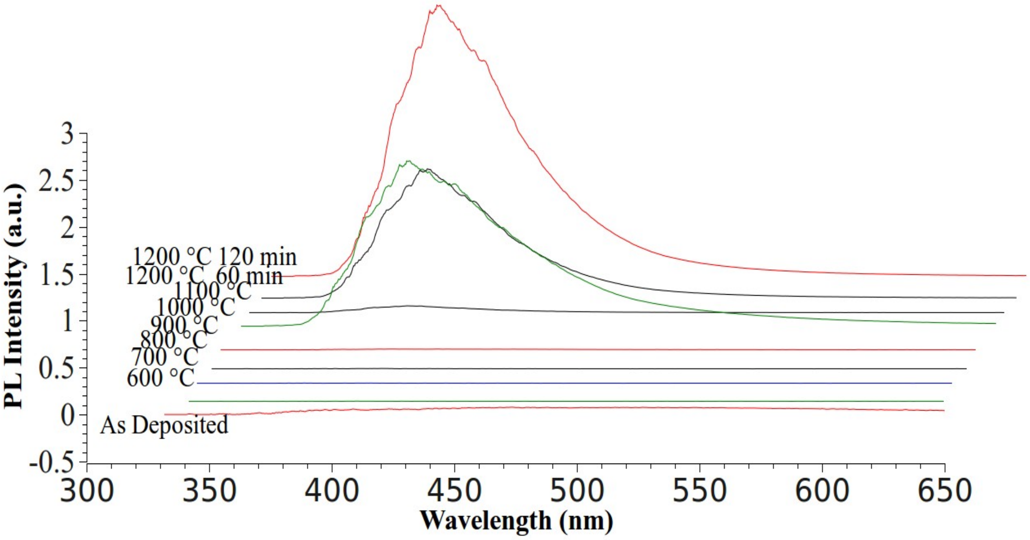

Figure 44: Typical changes in photoluminescent response of cerium doped films annealed at temperatures ranging from 600-1200 °C. A significantly reduced emission is seen at 1100 °C. Increasing the annealing temperature to 1200 °C shows a return of much of the luminescence and longer annealing at this temperature results in an even more intense response.

Photoluminescence measurements of the cerium doped films display little change below annealing temperatures of 900 °C as presented in the typical spectra displayed by sample WNP5-005 shown in Figure 44. This is to be expected since the Ce deposited from the precursor is in the form of the optically inactive tetravalent ions [6]. No significant change in the emission is seen until 1000 °C when a blue emission becomes visible and the photoluminescence increases dramatically for all of the samples, and generally increases with the cerium concentration in the films. Upon annealing at 1100 °C the integrated luminescent intensity drops off by ~96-98% for all of the samples.[1].

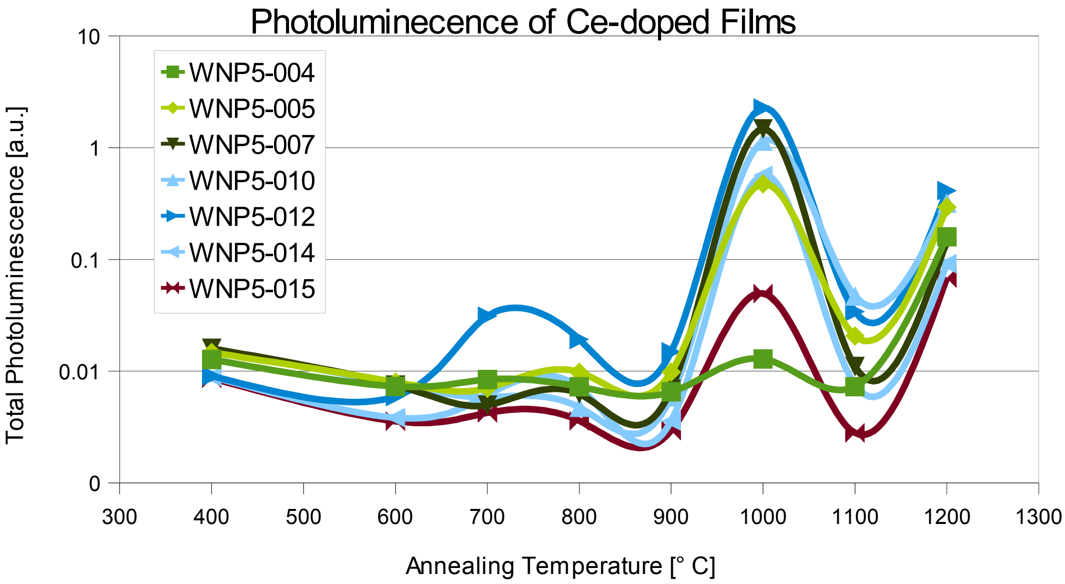

Figure 45: Photoluminescent response of the Ce-doped films with changing annealing temperature for 60 min anneals. Decreased luminescence is seen for all films at 1100° C but returns after annealing at 1200 ° C.

Increasing the annealing temperature to 1200 °C causes a significant return of the luminescence. This behaviour is shown in Figure 45. Extended annealing at 1200 °C for

---

[1] It is possible that this drop was caused by atmospheric contamination or another problem during the annealing at 1100° C, however this seems less likely since the annealing was done in two batches. This was done to avoid having samples near the edge of the boat where the temperature of the tube furnace is expected to drop off. The second run was, however, completed directly after the first run, so an unknown problem in the annealing is not out of the question.

120 minutes generally causes further enhancement of the photoluminescent output. Similar behaviour has been noted in the formation of cerium-silicates in doped silicon oxides during annealing [6], however, an explanation of the luminescence mechanism and its relation to the microstructural changes in the films require further dedicated study.

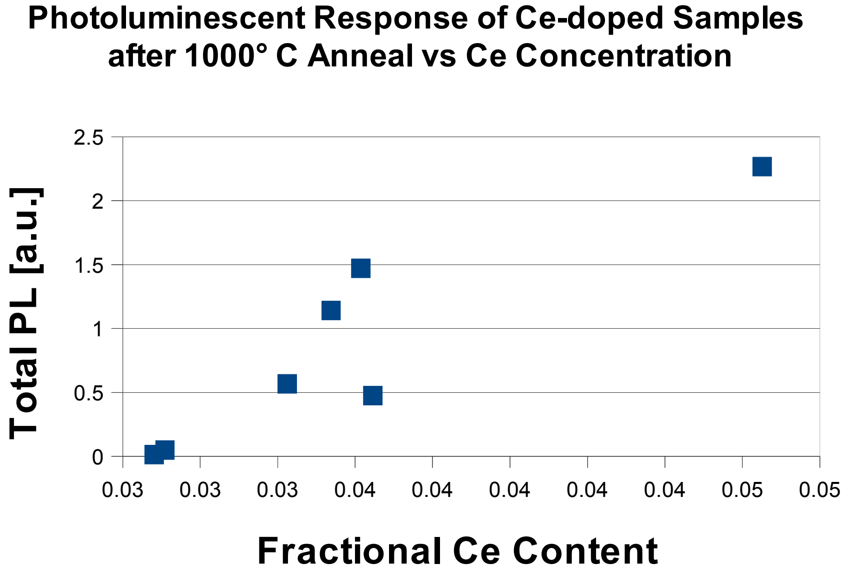

Figure 46: Increasing Ce concentration causes an increased photoluminescent response (shown at 1000° C, normalized to film thickness) indicating that self-quenching is not a limiting factor at these concentration levels.

Section 6.7: Aluminium Doped Silicon Oxide Films

The final sample set of film depositions used the precursor Al(TMHD)$_3$ for *in situ* doping of oxynitride films with aluminium. After careful cleaning, the precursor was loaded into the canister and this was fitted to the delivery system and the heating jacket was placed over the canister. A careful bake out of the precursor lines was performed to remove any remaining Ce contamination. Samples of $SiO_{x>2}$:Al were prepared with varying temperatures of the precursor from 160° C to 220° C. The silane flow was held at 5 sccm with an O_2/Ar flow of 30 sccm and a precursor carrier gas flow of 10 sccm. Deposition time was 60 min for all of the growths and substrate heater temperatures were held at 300° C.

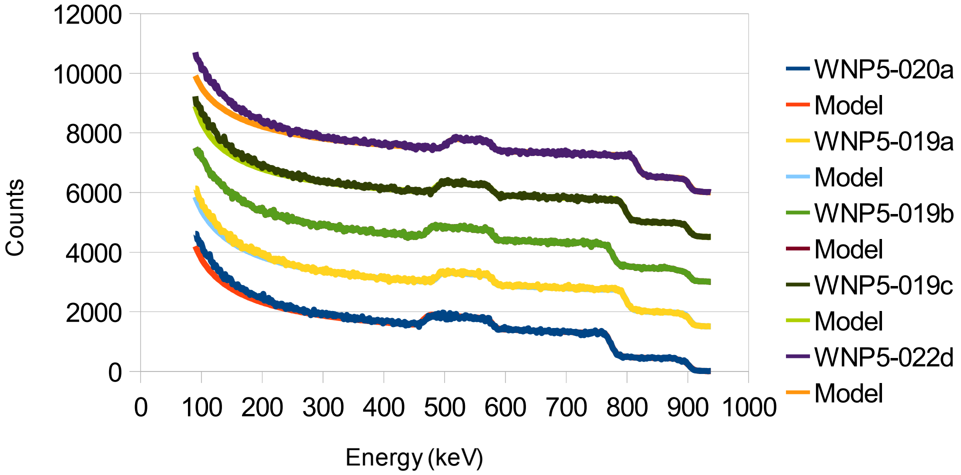

Figure 47: RBS spectra for SiO_x films doped with aluminium as well as stoichiometric SiO_2. The small difference in mass between Si and Al causes the Al to be visible only as a difference in the height of the silicon film edge

RBS analysis (see Figure 47 for spectra) shows significant aluminium incorporation, as is also shown in Table 10. For comparison a deposition with similar parameters but without the precursor flow is included. Although the sample set is quite small, it is clear that the higher precursor temperatures lead to increasing aluminium incorporation. Carbon contamination was negligible in the samples and the films with larger aluminium incorporation showed reduced levels of silicon.

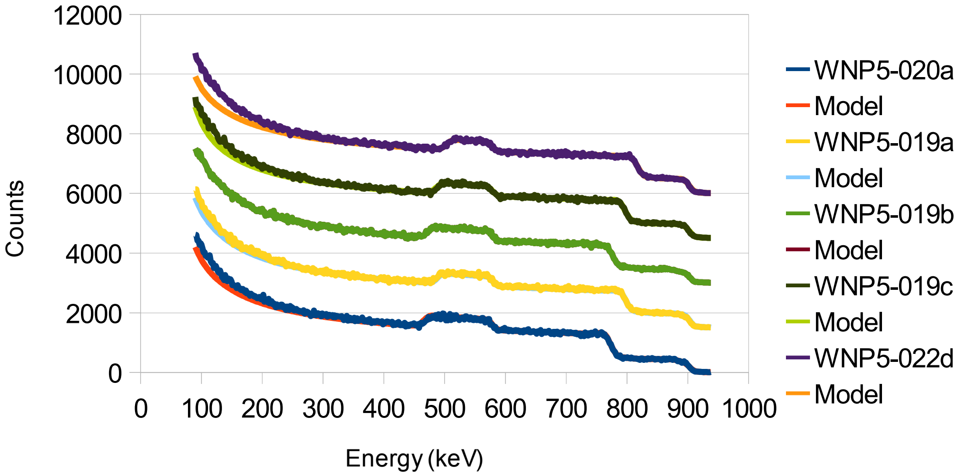

Figure 48: RBS spectra for SiO_x films doped with aluminium as well as stoichiometric SiO_2. The small difference in mass between Si and Al causes the Al to be visible only as a difference in the height of the silicon film edge

Table 10: Composition of Al doped SiO_x Films

Sample	Cell Temp [° C]	Si	O	Al	n @ 632.8 nm	Growth Rate [nm/min]
WNP5-020a	220	23.9%	69.8%	6.3%	1.521	4.55
WNP5-019b	200	25.2%	68.5%	6.2%	1.515	4.15
WNP5-019a	180	31.1%	66.7%	2.2%	1.487	4.55
WNP5-019c	160	30.2%	66.9%	2.8%	1.467	3.50
WNP5-022d	N/A	33.2%	66.8	0%	1.465	2.90

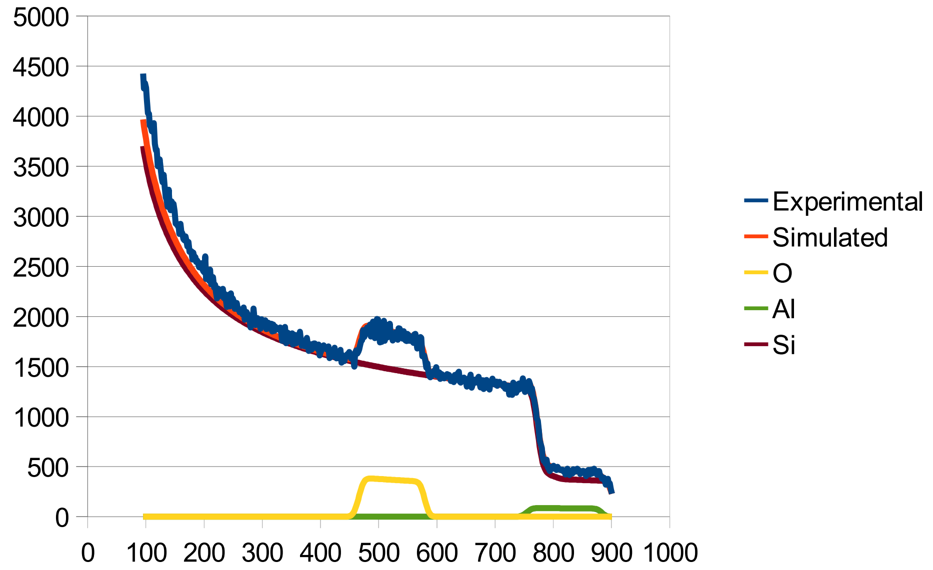

Figure 49: Contributions of individual elements to the simulated RBS spectra of sample WNP5-020a. The presence of aluminium is detectable by the lower-than-experimental silicon film edge and a slight lip on the substrate silicon edge.

Difficulties in ascertaining the aluminium content from RBS result from the close atomic masses of Si and Al, which makes the contributions overlap. The presence of aluminium causes an increase in the initial film edge and a lip on the substrate edge. Unlike the oxygen and nitrogen peaks in prior growths, which tend to smoothly and gradually blend together, the overlap of the silicon and oxygen signal is causes a distinct step in the pre-substrate region of the spectrum. This makes the determination of the relative concentrations of aluminium and silicon easier and more reliable

The growth rate of the aluminium doped films is slightly higher than that of the undoped silicon oxide films deposited under similar conditions. The refractive index at 632 nm tends to increase with aluminium content.

Chapter 7: Conclusions and Future Work

A new electron cyclotron resonance plasma enhanced chemical vapour deposition system was successfully setup in the CEDT laboratories at McMaster University. While an overview of the system was given in Chapter 5 many of the details in the installation process were omitted for brevity. Much of the work of this project focused on the installation, calibration of subsystems and maintenance of the system.

Depositions of silicon oxide were performed during initial system testing to narrow down desirable settings for some of the process variables. The growth rate was seen to decrease as sample-plasma source distance increased and the refractive index increased at closer distances, implying silicon rich composition. The source-sample distance for subsequent depositions was chosen to be 35 mm. Varying the ratio of silane to oxygen/argon during depositions led to a peak growth rate at a flow ratio of 1.20 and growth rates decreasel with both higher relative oxygen and silane flows. The refractive index is seen to increase with an excess of silane in the chamber. The effect of pressure changes in the region between 20 and 80 mTorr is a decrease in growth rates for higher pressures and a linear increase in the refractive index with increasing pressure.

A series of silicon oxide growths under high vacuum (~3mTorr) showed a nearly linear increase in growth rates with increasing silane flow. As expected, higher silane flow yielded films with refractive indces significantly above the thermal silicon dioxide index.

Repeated growths under the same conditions showed that the system is capable of high repeatability.

Changing the stage temperature for select growth conditions showed that the refractive index is stable and close to the thermal oxide values and that the growth rate is seen to decrease with increasing stage temperature.

While general relationships between the gas flow ratios and the substrate temperature on the one hand and refractive index and growth rates on the other were established, future studies should be done with a larger sample set to improve measurement statistics. It would be wise to repeat some growths to establish if the system exhibits any notable drift with both time and use. The regular growth of a small set of samples under predetermined growth conditions every few months and a set number of deposition hours would be useful in measuring any drift. Running such a set before and after a plasma clean could also be of interest.

A series of undoped silicon oxynitride depositons was prepared and non-uniformity was seen to be around 1%. Growth rates were fairly stable at ~3.5 nm/min. As expected, the refractive index was seen to increase as more nitrogen was incorporated into the film. Films with higher nitrogen content approached a refractive index of 1.7. RBS analysis of the oxygen-free silicon nitride films showed that the films were nitrogen-rich, which accounts for the lower than stoichiometric refractive index.

Future studies aimed at SiO_xN_y growths of low x may wish to reduce the flow of nitrogen with an addition of argon to maintain deposition pressure. Using a more dilute nitrogen mixture may be another alternative which would allow better control of molar flow of nitrogen since it would not require lower nitrogen flow rates.

Ce-doped SiO_xN_y films were prepared using the $Ce(TMHD)_4$ precursor sublimated into an argon flow. RBS analysis of the films showed significant carbon contamination. The likely source is the ligands of the metalorganic precursor and could be attributed to excessive precursor temperature or a potential breakdown of the precursor caused by a thermal shock during the calibration. The density of the films was, however, quite constant near $5x10^{22}$ atoms/cm^3.

While the cerium incorporation was quite high at ~3-5%, growths with a fresh load of the precursor and at lower temperatures should be run to see if the carbon contamination can be minimized.

The large parameter space of the effectively quaternary system makes the determination of any relationship between growth rates, refractive index and film composition impossible with such a limited sample set. This portion of the project was intended more as a test of the capabilities of the system over a wide composition range than a definitive study of such a wide range of compositions. The designer of future studies would be wise to restrict the composition parameter space in order to gain a better understanding of a smaller range of materials.

Photoluminescence measurements showed little intensity at sample annealing temperatures below 1000° C after 60 minutes. A blue emission was seen from all the cerium doped samples. The luminescence was strong enough to easily be seen with the naked eye. A sharp drop in luminescence was observed after annealing at 1100° C and the luminescence returned when the annealing temperature was increased to 1200° C. The luminescence was further enhanced with longer annealing at 1200° C. Generally, increasing cerium content in the films led to a higher luminescence.

The use of transmission electron microscopy (TEM) may yield additional information on possible changes in the film structure, which could explain the drop in luminescence at 1100° C. The time and training required to carry out such work was beyond the scope of this study. It may be prudent for future depositions of Ce-doped silicon oxynitrides to be limited to a single set of gas flow parameters and a range of precursor temperatures. Although tedious, a series of depositions starting at a low sublimator temperature (such as 140° C) and working up in small increments (5° C) may yield a critical temperature at which cerium incorporation occurs. Such studies could potentially give a better understanding of the relationship between precursor temperature and carbon contamination. Finally, these studies could help determine a solid relationship between cerium content and luminscence. If a well-defined relationship is seen higher cerium content could potentially be studied by reducing the overall source gas flows while maintaining the same ratios and using additional argon to maintain the same deposition pressure. If the precursor temperature is held below a temperature at which the carbon contamination is seen, and the carrier flow is maintained, one could expect higher cerium content in otherwise similar matrices.

Finally, the use of $Al(TMHD)_3$ was evaluated for *in situ* doping of silicon oxide films with aluminium. The films were generally oxygen rich relative to silicon, and aluminium incorporation up to 6% was seen. This set of films did not demonstrate any measurable carbon contamination.

This final study was by no means a definitive study on Al-doped SiO_x grown by this method and much more work is needed in this direction. The use of $Al(TMHD)_3$ as an Al dopant of silicon based films was, however, successfully demonstrated.

Chapter 8: References

[1]G. E. Moore, “Cramming more components onto integrated circuits,” Proceedings of the IEEE, vol. 38, no. 1, 1965.

[2]“Energy Consumption by Sector,” U.S. Energy Information Adminstration (2009), [Online] available: http://www.eia.gov/totalenergy/data/annual/index.cfm

[3]A.J. Kenyon, “Recent developments in rare-earth doped materials for optoelectronics,” Prog. Quantum Elec. 26, 225-284, 2002

[4]Philippe M. Fauchet, “Monolithic Silicon Light Sources,” Topics in Applied Physics, 94, 177, 1999

[5]L. T. Canham, “Silicon quantum wire array fabrication by electrochemical and chemical dissolution of wafers,” Appl. Phys. Lett., 57(10), 1046, 1990

[6]Jing Li, Othman Zalloum, Tyler Roschuk, Chenglin Heng, Jacek Wojcik, Peter Mascher. “The formation of light emitting cerium silicates in cerium doped silicon oxides” Appl. Phys. Lett., 94, 011112 , 2009

[7]Graham Reed and Andrew Knights, *Silicon Photonics: An Introduction*, p 223-242, John Wiley and Sons, 2004

[8]T. Roschuk, P. R. J. Wilson, O. H. Y. Zallom, J. Li, Jacek Wojcik and Peter Mascher. “Structure and luminescence of rare earth- doped silicon oxides studied through their X-ray absorption near edge structure and X-ray excited optical luminescence”, Phys. Status

Solidi B, 247 (2), 248-253, 2010.

[9]Dennis W. Hess and David B. Graves. “Plasma-Assisted Chemical Vapor Deposition” in C*hemical Vapor Deposition*. Micheal L. Hitchman and Kavs F. Jensen Eds. San Diego: Academic Press, 1993. pp 385-431.

[10]IC knowledge inc. “Chemical Vapour Deposition” in *Visual Guide to Process Equipment,* pp. 12-17, [Online] available: http://www.icknowledge.com/our_products/Chapter%204.pdf

[11]Arthur Sherman. *Chemical Vapor Deposition for Microelectronics: Principles, Technology and Applications.* Park Ridge, NJ: 1987: pp 1-37

[12]Daniel M. Dobkin and Micheal K. Zuraw. *Principles of Chemical Vapor Deposition: What's Going on Inside the Reactor.* Netherlands: Kluwer Academic, 2003.

[13]Aicha Elshabini-Riad and Fred D. Bralow III. *Thin Film Technology Handbook.* New York: McGraw Hill, 1997.

[14]Kiyotaka Wasa and Shigeru Hayakawa, *Handbook of sputter deposition technology: principles, technology, and applications.* Park Ridge, N.J., U.S.A.: Noyes Publications, 1992.

[15]Walter S. Knodle and Robert Chow, “Molecular Beam Epitaxy: Equipment and Practice,” in *Handbook of thin-film deposition processes and techniques: principles, methods, equipment, and applications.* Park Ridge, N.J., U.S.A.: Noyes Publications, 1988, ch. 6.

[16]F. Simeon, "Note on the Production of Mirrors by Cathodic Bombardment" in *The Making of Reflecting Surfaces,* Phys. Soc., London, 1920, pp 26-28

[17]D. M. Dobkin and M. K. Zuraw, *Principles of chemical vapor deposition.* Boston : Kluwer Academic Publishers, 2003

[18]Donald A. Gurnett, A. Bhattacharjee, *Introduction to plasma physics: with space and laboratory applications.* New York : Cambridge University Press, 2005.

[19]T. J. M. Boyd, J. J. Sanderson, *The Physics of Plasmas*. New York: Cambridge University Press, 2003.

[20]Keith Stowe, *Introduction to Statistical Mechanics and Thermodynamics*, 2nd Ed., Cambridge University Press 2007.

[21]J. A. Meyer, G.H. Kim, M. J. Goeckner and N. Hershkowitz. "Measurements of the presheath in an electron cyclotron resonance etching device" in *Plasma Sources Sci. Technol.* vol. 1, pp. 147-150, 1992.

[22]Marcel G. Boudreau, "SiO_xN_y Waveguides Deposited by Electron Cyclotron Resonance Chemical Vapour Deposition," M.A.Sc. Thesis, Engineering Physics, McMaster University, Hamilton, Ontario, 1993, pp.8

[23]Francis F. Chen, *Introduction to Plasma Physics.* New York: Plenum Press, 1974, pp. 116-117.

[24]Eray S. Aydil et al., "Multiple steady states in electron cyclotron resonance plasma reactors", *J. Vac. Sci. Technol. A. vol. 11, no. 6, pp. 2883-2892, Nov/Dec, 1993.*

[25]Uman S. Inan and Marek Gołkowski, *Principles of Plasma Physics for Scientists and Engineers*. Cambridge University Press:New York. pp. 30-42.

*[26]*Francis F. Chen, *Introduction to Plasma Physics. New York: Plenum Press, 1974, pp. 146*

[27]J. A. Bittencourt, *Fundamentals of Plasma Physics,* New York: Pergamon Press, 1986, pp. 205.

[28]A. del Prado, E. S. Andrés, I. Mártil, G. Gonazález-Diaz, D. Bravo, F. J. López, W. Bohne, J. Röhrich, B. Selle and F. L. Martinez, "Optical and structural properties of $SiO_xN_yH_z$ films deposited by electron cyclotron resonance and their correlation with composition", J. Appl. Phys., vol. 93, no. 11, pp. 8930-8938, June 2003.

[29]Herbert R. Philipp, "Optical and bonding model for non-crystalline SiO_x and SiO_xN_y Materials," *J. Non-crystalline Solids,* 8-10, pp. 627-632, 1972.

[30]T. S. Eriksson, C. G. Granqvist, "Infrared optical properties of silicon oxynitride films: Experimental data and theoretical interpretation" J. Appl. Phys., vol. 60, No. 6, pp. 2081-2091, 1986.

[31]I. Y. Y. BU, A. J. Flewitt and W. I. Miline, "Nanocrystalline Silicon Thin Films Fabricated at 80°C by Using Electron Cyclotron Resonance Chemical Vapor Deposition", *Plasma Sci. Tech.*, vol. 12 No. 5, pp. 608-613, Oct, 2010.

[32]T. Roschuk, "Characterization of Amorphous Silicon (a-Si) and Silicon Rich Silicon Oxide (SiO_x) Materials Produced by ECR-PECVD," M.A.Sc. Thesis, Engineering

Physics, McMaster University, Hamilton, Ontario, 2005. pp. 29

[33]Milton Ohring, *The Materials Science of Thin Films*, Academic Press, Inc. New York, New York, 1992.

[34]R. Wood, "Electron Cyclotron Resonance Chemical Vapour Deposition of SiO_xN_y Films for Use in Flat Panel Displays," M.A.Sc. Thesis, Engineering Physics, McMaster University, Hamilton, Ontario, 2006. pp. 2-27.

[35]E. Meeks, R. S. Larson, P. Ho, C. Apblett, S. M. Han, E. Edelberg and E. S. Aydil, "Modeling High-Density-Plasma Deposition of SiO_2 in $SiH_4/O_2/Ar$" Sandia National Laboratories, Albuquerque, New Mexico, SAND97-8241-UC-401, 1997.

[36] Huijuan Bi, Weiping Cai, Huazhong Shi, Baodian Yao and
Lide Zhang, "Effects of annealing and Al co-doping on the photoluminescence of
Ce3+-doped silica prepared by a sol–gel process." *J. Phys. D: Appl. Phys*. Vol. 33 pp. 2369–2372, 2000

[37] Yoshiro Ishii, Kazuo Arai, Hiroshi Namikawa, Mitsuhiro Tanaka, Akira Negishi and Takashi Handa, "Preparation of Cerium-Activated Silica Glasses: Phosphorus and Aluminum Codoping Effects on Absorption and Fluorescence Properties." Journal of the American Ceramic Society, Vol. 70, No. 2, pp.72-77, 1987.

[38]Markku Leskelä, Reijo Sillanpää, Lauri Niinistö and Marja Tiitta, "Structural and Thermal Studies of Tetrakis(2,2,6,6-tetramethyl-3,5-heptanedionato)cerium(IV)" *Acta Chemica Scandinavica*, vol. 45 pp. 1006-1011, 1991.

[39]Jing Li, "Light Emission from Rare Earth-Doped Silicon Oxide Thin Films Deposited by ECR-PECVD," M.A.Sc. Thesis, Engineering Physics, McMaster University., Hamilton, Ontario, 2008, pp.14

[40]Chemical Book (2008) "TRIS(2,2,6,6-TETRAMETHYL-3,5-HEPTANEDIONATO)ALUMINUM CAS#: 14319-08-5" [Online] available: http://www.chemicalbook.com/ProductChemicalPropertiesCB5701555_EN.htm

[41]David Brewster, *A treatise on optics.* Longman, Brown, Green and Longman (1857), pp. 127.

[42]Alexandre Rothen, *The Ellipsometer, an Apparatus to Measure Thicknesses of Thin Surface Films*. Review of Scientific Instruments, 16:2 pp26-30, February 1945.

[43]Harland G. Tompkins, *Spectroscopic Ellipsometry and Reflectometry: A User's Guide.* New York: Wiley, 1999, pp. 2.

[44]Harland G. Tompkins, *User's Guide to Ellipsometry.* Boston: Academic Press, 1993, pp. 41

[45]F. L. Pedrotti, L. S. Pedrotti, L. M. Pedrotti, *Introduction to Optics, 3rd ed.* Upper Saddle River, N.J. : Pearson Prentice Hall, 2007.

[46]J. A. Woollam Co. "Spectroscopic Ellipsometry Tutorial Light and Materials I" [Online].

Available: http://www.jawoollam.com/tutorial_2.html

[47]R. M. A. Azzam, N. M. Bashra, *Ellipsometry and Polarized Light.* Amsterdam; New

York : North-Holland Pub. Co., 1977, pp. 18, 286

[48]Harland G. Tompkins, *Spectroscopic Ellipsometry and Reflectometry: A User's Guide.* New York : Wiley, 1999, pp. 27, 221-224

[49]John A. Woollam, Paul G. Snyder, "Fundamentals and Applications of Variable Angle Spectroscopic Ellipsometry," *Materials Science and Engineering B*, vol. 5, pp. 279-283, May, 1990.

[50]"Guide to Using WVASE 32 Software for Spectroscopic Ellipsometry Data Acquisition and Analysis." J. A. Woollam Co Inc.,2001, pp. 61.

[51]O.H.Y. Zalloum et al., "Laser photoluminescence spectrometer based on charge-coupled device detection for silicon-based photonics," *Review of Scientific Instruments*, vol. 77, no. 2, pp. 23907, 2006.

[52]Ocean Optics Inc. "S2000 Spectrometer Data Sheet" 203-00000-J7D-05-0704 , Dunedin Fl.

[53]L.C. Feldman and J. W. Mayer. *Fundamentals, Surface and Thin Film Analysis*. New York: North-Holland, 1986

[54]E. Rauhala, N. P. Barradas, S. Fazinic, M. Mayer, E. Szilágyi and M. Thompson. et al. "Status of ion beam data analysis and simulation software" *Nucl. Instr. And Meth. In Phys. Res. B*, vol 244, pp. 436-456, Nov 2005.

[55]J.F. Ziegler. Helium - Stopping Powers and Ranges in All Elements, vol. 4 of *The Stopping and Ranges of Ions in Matter*. Pergamon Press, New York, 1977.

[56]M. Mayer, SIMNRA User’s Guide, Report IPP 9/113, Max-Planck-Institut für Plasmaphysik, Garching, Germany, 1997

[57]J.F. Ziegler and J.M. Manoyan. Nucl. Instr. Meth. B 35 (1988) 215

[58]Electronic Measurement's INC. “Instruction Manual for EMS Power Supply Model 20-125-2-D 10T/P”

[59]“Astex S1000 Installation Manual”, 1997.

[60]L. G. Carpenter, *Vacuum Technology: An Introduction*, New York: American Elsevier Pub. Co.,1970.

[61]Aydil et al., “Multiple steady states in electron resonance plasma reactors”, J. Vac. Sci. Technol. A, vol. 11, no. 6, pp. 2883-2892, Nov/Dec 1993.

[62]Nigel Harris, *Modern Vaccum Practice 3rd Edition,* McGraw-Hill, New York, 2005.

[63]“TMH 520/TMU 520/TMH 520 P/TMU 520 P Turbomolecular Drag *Pumps” Pfeiffer Vacuum, 2008.*

[64]P. Biltoft, B. Benapfl, and T. Swain, *Vacuum Technology, An Introductory Laboratory Course, Las Positas College , 2002.*

[65]*“Sample Stage General Assembly”, Johnsen Ultravac Drawing #09047SSGA, Burlington, Ontario, 2009.*

[66]*“Gas Distribution Ring”, Johnsen Ultavac Drawing #9047GDR, Burlington, Ontario, 2009.*

[67]J. H. Batey, “Quadrupole Gas Analyzers”, *Vacuum*, vol. 37, no. 8-9, pp.659-668,

1987.

[68]MKS Instruments (2011), “Gas Correction Factors”[Online]. Available: http://www.mksinst.com/TechInfo/gasconversiontable.aspx

[69]Edward Irving, “Erbium Doped SiO_xN_y Waveguides Produced by ECR-PECVD” M.A.Sc. Thesis, Engineering Physics, McMaster University, Hamilton, Ontario, 2003. pp 53.

[70]Matej Mayer, “SIMNRA User’s Guide 6.05” Max-Planck-Institut für Plasmaphysik, 2009.

[71]Haiqiang Zhang, “Study of Optimal Deposition Conditions for an Inductively Coupled Plasma Chemical Vapour Deposition (ICP-CVD) System.” M.A.Sc. Thesis, Engineering Physics, McMaster University, Hamilton, Ontario, 2005. pp. 72-73.

[72]“Strem Chemical Catalog” Strem Chemicals, Inc., 2010

[73]W. Eckstein and M. Mayer, “Rutherford backscattering from layered structures beyond the single scattering model” Nuclear Instruments and Methods in Physics Research B, vol.153, pp337-344, 1999.

[74]L. Wang, H.S. Reehal, F.L. Martinez,E.S. Andres, A. del Prado, A,“Characterization of nitrogen-rich silicon nitride films grown by the electron cyclotron resonance plasma technique”, Semiconductor Science and Technology, Vol. 18, pp. 633-641, 2003.

[75]Eurotherm 2408 Temperature Controller Manual

[76]Patrick Wilson, Private communication